Lanthanide(III)-Based Single-Molecule Magnets: Design, Synthesis, Magnetic and Luminescent Properties

Zur Erlangung des akademischen Grades eines

DOKTORS DER NATURWISSENSCHAFTEN

(Dr. rer. nat.)

von der KIT-Fakultät für Chemie und Biowissenschaften

des Karlsruher Instituts für Technologie (KIT)

genehmigte

DISSERTATION

von

M. Eng., Yangxin Chen

1. Referent / Referentin: Prof. Dr. Annie K. Powell
2. Referent / Referentin: Prof. Dr. Horst Geckeis

Tag der mündlichen Prüfung: 03.02.2026

I. Eidesstattliche Erklärung

Bei der eingereichten Dissertation zu dem Thema

Lanthanide(III)-Based Single-Molecule Magnets: Design, Synthesis, Magnetic and Luminescent Properties

handelt es sich um meine eigenständig erbrachte Leistung.

Ich habe nur die angegebenen Quellen und Hilfsmittel benutzt und mich keiner unzulässigen Hilfe Dritter bedient. Insbesondere habe ich wörtlich oder sinngemäß aus anderen Werken übernommene Inhalte als solche kenntlich gemacht.

Die, Arbeit oder Teile, davon habe ich bislang nicht an einer Hochschule des In- oder Auslands als Bestandteil einer Prüfungs- oder Qualifikationsleistung vorgelegt.

Die Richtigkeit der vorstehenden Erklärungen bestätige ich.

Die Bedeutung der eidesstattlichen Versicherung und die strafrechtlichen Folgen einer unrichtigen oder unvollständigen eidesstattlichen Versicherung sind mir bekannt.

Ich versichere an Eides statt, dass ich nach bestem Wissen die reine Wahrheit erklärt und nichts verschwiegen habe.

....

Ort und Datum

....

Unterschrift

II. Note

The ions shown in the illustrations are not to scale. Organic hydrogen atoms are usually omitted for clarity. Atoms and ions are shown in the following colours in all illustrations:

Element	**Colour**
Dy	Bright blue
Nd	Pink
Zn	Bright green
C	Grey
O	Red
Cl	Yellow
N	Dark blue
H	White

Numerical quantities such as bond lengths and angles are given with their standard uncertainties in round brackets after the respective values and refer to last digits.

This thesis was prepared from 1st of January 2022 to 17th of December 2025 at the Institute of Inorganic Chemistry (AOC), Faculty of Chemistry and Biosciences of the Karlsruhe Institute of Technology (KIT) under the supervision of Prof. Dr. Annie K. Powell.

III. List of Abbreviations

χ	magnetic susceptibility
χ^M	molar magnetic susceptibility
μ	magnetic moment
μ_B	Bohr magneton
λ	Wavelength
M	Magnetization
T	Temperature
T_B	blocking temperature
CASSCF	complete active space self-consistent field
U	energy barrier
PXRD	powder X-ray diffraction
IR	infrared vibrational spectroscopy
SQUID	superconducting quantum interference device
SOC	spin orbit coupling
Ln	lanthanide (including Y^{III} as diamagnetic substitute)
D	Anisotropy
QTM	quantum tunnelling of magnetisation
ZFQTM	zero-field quantum tunnelling of magnetisation

Table of Contents

Chapter 3. Single-Molecule Magnet Behavior in Lanthanide–Pyrene-4,5-Semiquinate Radical Complexes 71

Abstract

Lanthanide-based single-molecule magnets (SMMs) have attracted significant attention due to their unique magnetic and luminescent properties, which make them promising candidates for high-density data storage, quantum computing, and molecular spintronics.

This thesis is divided into four main chapters, focusing on the design, synthesis, and characterization of lanthanide complexes. It explores single-molecule oxygen radical magnetic materials and 3d-4f magneto-optical properties of DOTA-based ligands.

In Chapter 1, “Introduction,” the background and motivation for studying lanthanide SMMs are discussed. Key concepts including mononuclear and dinuclear lanthanide SMMs, slow magnetic relaxation, and the role of ligand design in tuning magnetic and luminescent properties are introduced.

In Chapter 2, “Single-Molecule Magnet Behavior in Lanthanide–9,10-Phenanthrenequinone Radical Complexes,” coordination compounds based on the oxygen radical $\mathrm{phsq^{-}}$ ligand (phsq = 9,10-phenanthrenesemiquinonate radical) were investigated. By coordinating axial triphenylphosphine oxide (tppo) and tricycloheanexphosphine oxide (tcypo) ligands, fifteen air-stable radical complexes, $[\mathrm{Ln^{3+}{}_2(phsq)_4(tppo)_2(NO_3)_2}]$ or $[\mathrm{Ln^{3+}{}_2(phsq)_4(tcypo)_2(NO_3)_2}]$, were synthesized. Whereas the $\mathrm{Sm^{3+}}$ to $\mathrm{Lu^{3+}}$ complexes are isostructural, the $\mathrm{Ce^{3+}}$ and $\mathrm{Nd^{3+}}$ analogues display distorted ligand arrangements. Compounds $[\mathrm{Ln^{3+}{}_2(phsq)_4(tppo)_2(NO_3)_2}]$ (Ln = Nd, Dy, Tb) and $[\mathrm{Dy^{3+}{}_2(phsq)_4(tcypo)_2(NO_3)_2}]$ exhibit slow magnetic relaxation. In particular, the AC magnetic susceptibility of $[\mathrm{Dy^{3+}{}_2(phsq)_4(tppo)_2(NO_3)_2}]$ shows a maxima up to 14 K at the benchmark frequency of 1000 Hz with an effective energy barrier of ~100 K. Micro-SQUID measurements show the suppression of zero-field quantum tunneling and

CASSCF calculations, which are in very good confirm excellent agreement with experimental data, confirm the excellent SMM behavior.

In Chapter 3, “Single-Molecule Magnet Behavior in Lanthanide Radical Pyrene-4,5-dione Complexes,” the ligand was further modified to pysq $^{-}$ (pyrenesemiquinonate radical anion) by increasing the π-system of the ligand with the co-ligands triphenylphosphineoxide (tppo) and tricyclohexanephosphineoxide (tcypo) introduced axially. Six air-stable radical complexes, $[\mathrm{Dy^{3+}{}_2(pysq)_4(tppo)_2(NO_3)_2}]$ (Ln = Nd, Gd, Dy, Ho, Er) and $[\mathrm{Dy^{3+}{}_2(pysq)_4(tcypo)_2(NO_3)_2}]$, were synthesized. Among these, $[\mathrm{Dy^{3+}{}_2(pysq)_4(tppo)_2(NO_3)_2}]$ (Ln = Nd, Dy, Er) and $[\mathrm{Dy^{3+}{}_2(pysq)_4(tcypo)_2(NO_3)_2}]$ exhibit slow magnetic relaxation, with the Dy derivatives showing AC maxima at the higher temperature of 20 K (at 1000 Hz) and an effective energy barrier of ~327 K.

In Chapter 4, “Structure, Magnetic, and Luminescent Properties of Lanthanide-DOTA Complexes and Its Derivatives,” classical DOTA ligands were employed to construct 3d-4f heterometallic complexes. Optical studies show that [ZnDy(DOTA)] exhibits characteristic $\mathrm{Dy^{3+}}$ luminescence, and further modification of DOTA led to the $[\mathrm{Dy(H_2tapen)}]$ complex, expanding the exploration of lanthanide photophysical properties.

In summary, this thesis presents the design, synthesis, and detailed characterization of multifunctional lanthanide complexes, highlighting the relationship between their molecular structure, magnetic behavior, and luminescent properties.

Zusammenfasung

Lanthanidbasierte Einzelmolekülmagnete (SMMs) haben aufgrund ihrer einzigartigen magnetischen und lumineszenten Eigenschaften, die sie zu vielversprechenden Kandidaten für die Datenspeicherung mit hoher Dichte, das Quantencomputing und die molekulare Spintronik machen, große Aufmerksamkeit erregt.

Diese Dissertation gliedert sich in vier Hauptkapitel, die sich mit dem Design, der Synthese und der Charakterisierung von Lanthanoidkomplexen befassen. Sie untersucht magnetische Einzelmolekülmaterialien auf Sauerstoffradikalbasis sowie die 3d-4f-magnetooptischen Eigenschaften von DOTA-basierten Liganden.

In Kapitel 1, **"**Einleitung**"**, werden der Hintergrund und die Motivation für die Untersuchung von Lanthanoid-SMMs diskutiert. Es werden Schlüsselkonzepte wie einkernige und zweikernige Lanthanoid-SMMs, langsame magnetische Relaxation und die Rolle des Ligandendesigns bei der Abstimmung magnetischer und lumineszenter Eigenschaften vorgestellt.

In Kapitel 2, „Einmolekülmagnetverhalten in Lanthanoid-9,10-Phenanthrenchinon-Radikalkomplexen“, wurden Koordinationsverbindungen auf Basis des Sauerstoffradikalliganden phsq $^{-}$ (phsq = 9,10-Phenanthrensemichinonat-Radikal) untersucht. Durch Koordination axialer Triphenylphosphinoxid- (tppo) und Tricycloheanxphosphinoxid- (tcypo) Liganden wurden fünfzehn luftstabile Radikalkomplexe, $[\mathrm{Ln^{3+}_2(phsq)_4(tppo)_2(NO_3)_2}]$ bzw. $[\mathrm{Ln^{3+}_2(phsq)_4(tcypo)_2(NO_3)_2}]$, synthetisiert. Während die $\mathrm{Sm^{3+}}$- bis $\mathrm{Lu^{3+}}$-Komplexe isostrukturell sind, weisen die $\mathrm{Ce^{3+}}$- und $\mathrm{Nd^{3+}}$-Analoga veränderte Ligandenanordnungen auf. Die Verbindungen $[\mathrm{Ln^{3+}_2(phsq)_4(tppo)_2(NO_3)_2}]$ (Ln = Nd, Dy, Tb) und $[\mathrm{Ln^{3+}_2(phsq)_4(tcypo)_2(NO_3)_2}]$ zeigen eine langsame magnetische Relaxation. Insbesondere weist die AC-

Magnetisierungssuszeptibilität von $[Dy^{3+}{}_2(phsq)_4(tppo)_2(NO_3)_2]$ bei der Referenzfrequenz von 1000 Hz ein Maximum von bis zu 14 K mit einer effektiven Energiebarriere von ~100 K auf. Mikro-SQUID-Messungen zeigen die Unterdrückung des Quantentunnelns im Nullfeld, und CASSCF-Rechnungen, die in sehr guter Übereinstimmung mit den experimentellen Daten stehen, bestätigen das hervorragende SMM-Verhalten.

In Kapitel 3, „Einmolekülmagnetverhalten in Lanthanid-Radikal-Pyren-4,5-dion-Komplexen“, wurde der Ligand durch axiale Einführung der Co-Liganden Triphenylphosphinoxid (tppo) und Tricyclohexanphosphinoxid (tcypo) zu $pysq^{-}$ (Pyrenesemichinonat-Radikalanion) modifiziert. Sechs luftstabile Radikalkomplexe, $[Ln^{3+}{}_2(pysq)_4(tppo)_2(NO_3)_2]$ (Ln = Nd, Gd, Dy, Ho, Er) und $[Ln^{3+}{}_2(pysq)_4(tcypo)_2(NO_3)_2]$, wurden synthetisiert. Unter diesen weisen $[Dy^{3+}{}_2(pysq)_4(tppo)_2(NO_3)_2]$ (Ln = Nd, Dy, Er) und $[Ln^{3+}{}_2(pysq)_4(tcypo)_2(NO_3)_2]$ eine langsame magnetische Relaxation auf, wobei die Dy-Derivate AC-Maxima bei der höheren Temperatur von 20 K (bei 1000 Hz) und eine effektive Energiebarriere von ~327 K zeigen.

In Kapitel 4, „Struktur, magnetische und lumineszierende Eigenschaften von Lanthanoid-DOTA-Komplexen und deren Derivaten“, wurden klassische DOTA-Liganden zur Synthese von 3d-4f-Heterometallkomplexen verwendet. Optische Untersuchungen zeigen, dass [ZnDy(DOTA)] die charakteristische Dy^{3+}-Lumineszenz aufweist. Durch weitere Modifizierung von DOTA wurde der Komplex $[Dy(H_2tapen)]$ erhalten, wodurch die Erforschung der photophysikalischen Eigenschaften von Lanthanoiden erweitert wurde.

Zusammenfassend präsentiert diese Arbeit das Design, die Synthese und die detaillierte Charakterisierung multifunktionaler Lanthanoidkomplexe und hebt dabei den Zusammenhang zwischen ihrer Molekularstruktur, ihrem magnetischen Verhalten und ihren Lumineszenzeigenschaften hervor.

Chapter 1. Introduction

1.1 Background

In the context of today's big data era, the amount of information is growing exponentially, and how to store and process massive amounts of information in a limited space has become a focus of discussion[1-3]. As a result, attention has turned towards the development of new storage and processing technologies[4] where magnetic materials play an important role[4-5]. However, the superparamagnetic effect of conventional magnetic materials limits the storage density[6]. On the other hand, information processing technology that exploits quantum effects, namely quantum information processing (QIP)[7-13], has been actively pursued to increase processing speed. It has been proposed that magnetic materials with exotic quantum magnetic phenomena such as quantum tunneling of magnetization (QTM) are particularly useful for developing QIP architectures[14-16]. Therefore, the development of magnetic materials with defined magnetic properties is necessary to increase storage density and create quantum information processing devices such as quantum computers[17]. Recently, the demonstration of the Grover algorithm using the electronic and nuclear spin degrees of freedom is an important development in the context of the above discussion[14].

In recent years, molecule-based magnets have received global attention[18] as a result of the advantages they have over traditional magnetic materials such as high density, easy processing, and chemical controllability. Recent advances in experimental techniques and quantum chemical methods have led to the discovery of several novel magnetic phenomena in molecular magnetic materials, particularly in single-molecule magnets (SMMs) that exhibit hysteresis similar to that of traditional magnets[6].

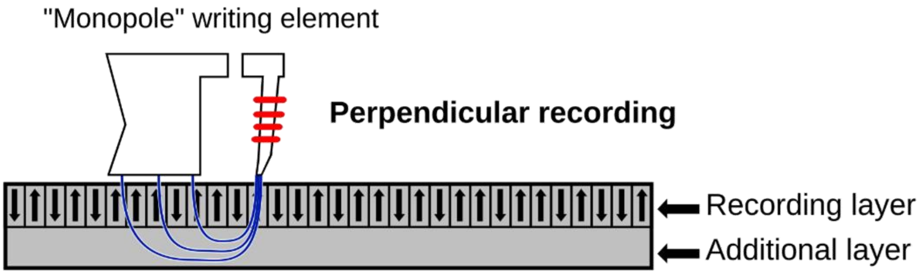

Figure 1.1. Storage read-write model diagram

In terms of storage, the magnetic domains are the basic unit of storage. As shown in Figure 1.1, the different magnetization orientations of magnetic domain units are used to store binary information 0 or 1. By magnetizing specific magnetic domains they obtain their 0 or 1, values which enables information storage and retrieval.

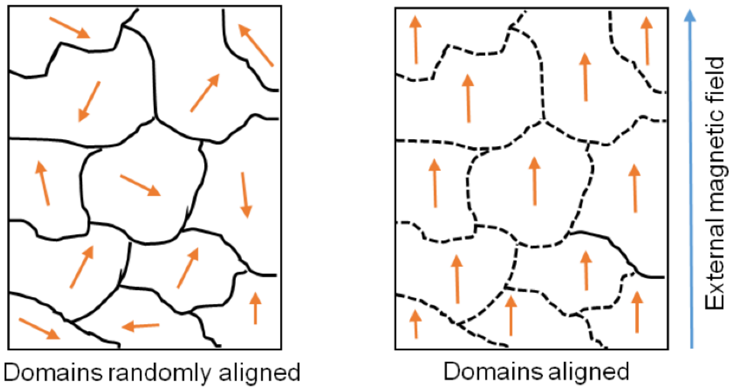

Figure 1.2. Schematic visualization of unmagnetized and magnetized magnetic domains.

As shown in the figure 1.2, the magnetic moments within one magnetic domain are arranged in the same direction, and the magnetic domains are arranged randomly, which means without an applied external magnetic field no net magnetic moment can be observed. In traditional storage hard disks, each magnetic domain is composed of magnetic grains, each made up of many atoms. The size of the magnetic domain ranges from micrometers to millimeters. This highlights a significant advantage of molecular data storage since each SMMs can, in theory, be used as an independent magnetic domain[19]. The size of such molecules is in the nanometer range. If a single molecule is used as an individual magnetic domain, the storage capacity within the same volume would increase by several orders of magnitude compared to traditional magnetic storage devices[15]. In 2025, scientists from the University of Manchester and the Australian National University synthesized the best single-molecule magnet $Dy\{N(Si^{i}Pr_3)Si(^{i}Pr)_2C(CH_3)=CHCH_3\}$[20] to date, which exhibits a blocking temperature of 100 K and an effective energy barrier of 1843(11) cm^{-1}. If used as a storage device, its storage performance is 3 Tb/cm^3, which is ca.100 times higher than the performance of traditional modern storage devices[20-23].

1.2 Single-Molecule Magnets

As the name suggests the magnetic properties of single-molecule magnet originates from the molecules themselves with each molecule acting as an isolated “magnetic domain”[24-25]. In the unmagnetized state, single-molecule magnets (SMMs) exhibit a bistable configuration with equal populations of two degenerate states which can be described as opposite spin orientations, resulting in a net magnetic moment of zero. When an external magnetic field is applied the degeneracy between these states is lifted. The spin orientation aligned with the field becomes energetically favorable and more populated, leading to a non-zero net magnetization. Upon removal of the magnetic field, an energy barrier inhibits the reversal of the molecular spin orientation, giving rise to magnetic hysteresis at the molecular level and slow relaxation of magnetization[26]. At high temperatures, the spins in single-molecule magnets can easily flip because the thermal energy overcomes the barrier between the two spin orientations (Figure 1.3). As the temperature decreases, the spins reverse more slowly, a phenomenon known as slow magnetic relaxation, which allows the material to retain magnetization over extended periods even without an external magnetic field. The energy required for spin reversal is called the effective energy barrier (U_{eff}) which determines the stability of the magnetic state. The blocking temperature (T_B) can be considered as the highest temperature at which magnetic hysteresis is observed (T_B will be discussed in more detail later in this section) [6, 27-31].

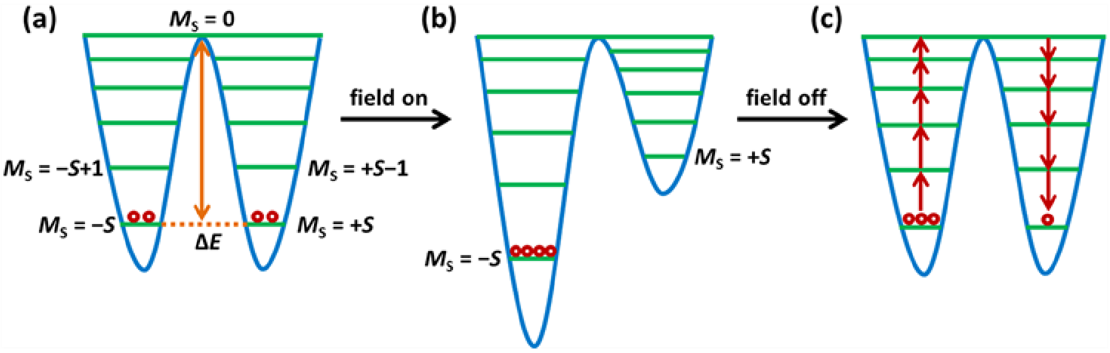

Figure 1.3. Bistability diagram of single-molecule magnets Copyright © 2011, American Chemical Society.

For a system with an integer total spin quantum number (S), the effective energy barrier (U_{eff}) can be expressed as: $U_{eff} = |D|S^2$[32]. When the total spin quantum number S of the system is a half integer, the effective energy barrier can be described by the following formula: $U_{eff} = D(S^2-1/4)$[33]. Here, D is the axial zero-field splitting (magnetic anisotropy) parameter[34-35], which represents the energy separation between different magnetic quantum numbers [$\pm M_s$, $\pm(M_s-1)$ …] in the absence of an external magnetic field [36-44]. For this slow magnetic relaxation process, when no external magnetic field is applied, the magnetic relaxation rate is described by the following equation:

$$\tau^{-1} = AT + \tau_0{}^{-1}\, exp^{-\frac{U_{eff}}{K_B T}} + CT^n + \tau_{QTM}^{-1}$$

The first term corresponds to the Orbach process, which is a two-phonon relaxation process caused by the transition from the ground state to the excited state and back to the ground state. The second term refers to the Raman process, which is also a two-phonon relaxation, but it absorbs phonons from the ground state to reach a virtual state (without the corresponding magnetic energy level) and then returns to the ground state[45]. The third component of the magnetic relaxation process is quantum tunneling, which involves direct transitions between the ground-state degenerate spin states without requiring energy exchange. This temperature-independent process contributes to the overall relaxation behavior of single-molecule magnets. In addition, the height of the spin-reversal energy barrier determines the stability of the magnetic state and plays a key role in establishing the blocking temperature (T_B) of the system. The blocking temperature (T_B) is the temperature at which the spins appear effectively "frozen" during a measurement. T_B depends on the measurement timescale and is often considered the temperature at which the magnetic hysteresis closes, however there are other definitions such as the temperature at which the relaxation time (τ) reaches 100 seconds, often referred to as $T_{B,100}$. In simpler terms, it can be viewed as the highest temperature at which magnetic hysteresis, the "memory" of magnetization, can still be detected.

There are several commonly used definitions of T_B:

i. The temperature at which the imaginary part of the AC magnetic susceptibility reaches a peak at a specific frequency.
ii. The temperature at which the magnetic hysteresis loop can be observed.

iii. The temperature at which the DC magnetic susceptibility under zero-field cooling (ZFC) exhibits a maximum.

The blocking temperatures obtained by these methods can vary significantly. Among them, the most frequently reported T_B corresponds to the temperature at which the hysteresis loop is observed. Additionally, some studies define T_B as the temperature at which the spin relaxation time reaches 100 seconds[21, 46].

Single-molecule magnets were first developed based on transition metal complexes. In the early days of single-molecule magnet research, scientists , primarily focused on polynuclear transition metal complexes, aiming to synthesize compounds with larger ground-state spin (S) values. For example, research in the field of single-molecule magnets began in the early 1990s, when Roberta Sessoli et al. [47] reported the magnetic properties of a mixed-valence manganese cluster, $[Mn_{12}O_{12}(O_2CMe)_{16}(H_2O)_4]$ (Mn_{12}), which exhibits single-molecule magnet (SMM) behavior. The compound was first synthesized by Lis [48] in 1980. As shown in Figure 1.4, the cluster contains eight Mn^{III} ions (S=2) at the outer positions and 4 Mn^{IV} ions (S = 3/2) in the central core. The outer Mn^{III} ions are ferromagnetically coupled among themselves, and the central Mn^{IV} ions are also ferromagnetically coupled. Antiferromagnetic interactions between the outer Mn^{III} ions and the central Mn^{IV} ions result in a antiferromagnetic coupling arrangement, giving rise to a high-spin ground state of S = 10.

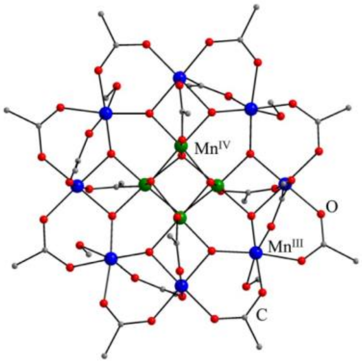

Figure 1.4. The structure of complex $[Mn_{12}O_{12}(O_2CMe)_{16}(H_2O)_4]$ (Mn_{12}). Color code: Mn^{IV} green, Mn^{III} blue, O red, C gray. Copyright © 2021, Elsevier.

Afterward, a series of high-nuclearity single-molecule magnets based on Mn^{III} have been reported, such as Mn_6[49], Mn_{19}[50], Mn_{25}[51], Mn_{31}[52], and Mn_{84}[53] clusters. In particular, the Mn_{84} clusters reported by Christou's group[53] (Figure 1-5 left) has a very high nuclearity, but its ground state spin is only 6 and its U_{eff} is also very small, only 12.5 cm^{-1}. In addition, Powell's group[50] achieved a high spin value of 83/2 in the ferromagnetically coupled $[Mn^{II}_7Mn^{III}_{12}]$ (Mn_{19}) complex, but no SMM behavior was observed.

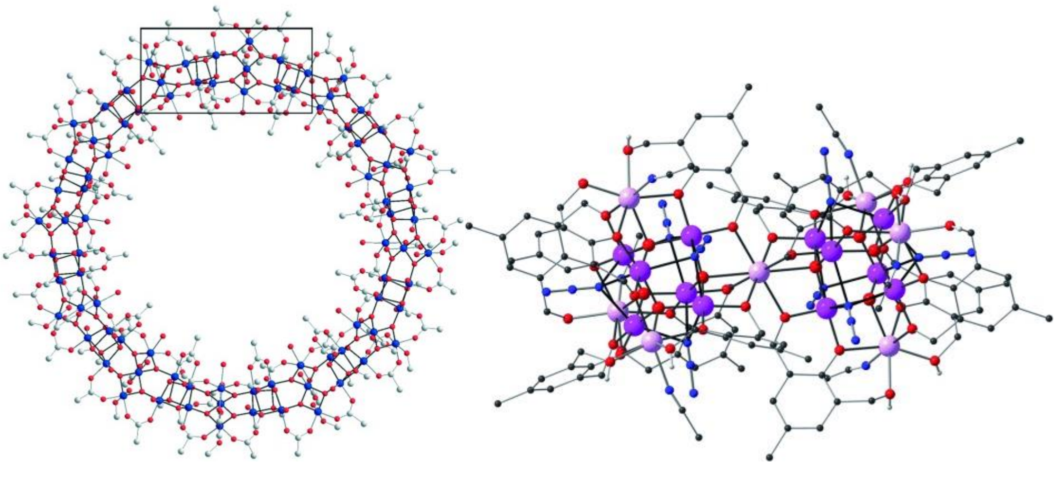

Figure 1.5. The structure of Mn_{84} clusters (left) Copyright © 2004, Wiley-VCH Verlag GmbH; and Mn_{19} clusters (right) Copyright © 2006, Wiley-VCH Verlag GmbH;

Therefore, scientists found that despite obtaining a large net spin ground state value, the system did not exhibit a correspondingly large effective energy barrier[54]. According to the relationship between the ground state quantum value and the effective energy barrier, in addition to the net spin quantum number, there is also a connection to magnetic anisotropy: despite a large net spin quantum number, the magnetic anisotropy within the molecule may cancel each other out due to the different orientations of the magnetic axes at different metal sites[55-56].

Compared with transition metals, lanthanide metals have unique advantages in the design and synthesis of single-molecule magnets because lanthanide elements are more likely to achieve energy level splitting than transition metals in the absence of a magnetic field[57]. Since the lanthanide ions have more unpaired electrons in their 4f electron layer, they have larger spin magnetic moments and more significant magnetic anisotropy[17]. The lanthanide ions have been used successfully to construct single-molecule magnets[58-59].

For trivalent dysprosium ions (Dy^{3+}) with a $4f^9$ electronic configuration, the free ions produce the ground-state term ^6H under the influence of Coulomb repulsion between electrons. This term contains 66 energy levels, which can be considered degenerate in the absence of other interactions. The presence of spin-orbit coupling (SOC) causes this term to further split into a series of non-degenerate levels, among which the branch with the lowest energy is $^6H_{15/2}$[60]; When the ion is placed in a crystal field with a specific symmetry, the crystal field further splits the spin-orbit ground-state branch J = 15/2 into individual levels corresponding to such as $m_J = \pm15/2, \pm13/2, \pm11/2 \ldots \pm1/2$[61]. Moreover, an external magnetic field (H) is the only factor that can cause an additional splitting of the CF sublevels through a phenomenon known as Zeeman effect[62] (Figure1.6). Therefore, from the perspective of electronic structure, since the trivalent dysprosium ion has a large spin value (s = 5/2) and a large orbital angular momentum (l = 5), the total orbital angular momentum J = 15/2 will lead to a particularly large magnetic anisotropy[63-64]. Therefore, lanthanide single-molecule magnets have been a hot research system in recent years, especially dysprosium ions, which have achieved remarkable single-molecule magnetic properties[65-70]. It describes the effects of various interactions on the splitting of the degenerate $4f^9$ configuration of the Dy^{3+} ion (Figure 1.6).

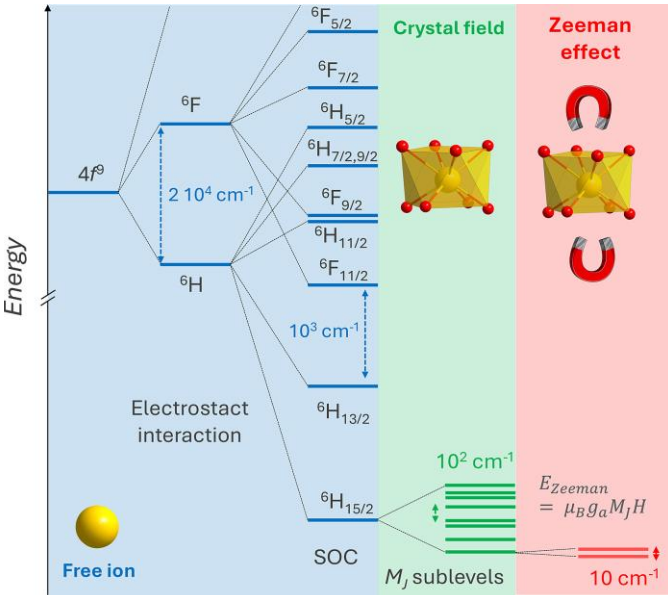

Figure 1.6. Partial energy diagram of Dy^{III} ion, comparing the electrostatic interaction and spin-orbit coupling (SOC) of the free ion, the influence of the crystal field (CF), and the Zeeman splitting (from left to right, interaction is from strong to weak) Copyright © 2025, Elsevier.

1.3 Mononuclear Lanthanide Single-Molecule Magnets

Mononuclear molecule magnets, also known as single-ion magnets, are the simplest single-molecule magnets[71-72]. They facilitate modeling for a deeper understanding of magnetic mechanisms. They can facilitate the design of high-performance single-molecule magnetic materials based on their molecular high symmetry[73-80].

In lanthanide single-molecule magnet systems, phthalocyanine is a very important ligand, capable of forming sandwich-type mononuclear single-molecule magnet structures with lanthanide ions[81-84], which serves as an important model system for studying the structure-property relationships of lanthanide SMMs. In 2003, Ishikawa et al. [85] reported a type of sandwich-shaped, mononuclear rare-earth single-molecule magnet, $[Pc_2Ln]^-$ (Ln = Tb, Dy; Pc = phthalocyanine dianion) (Figure 1.7). This molecule exhibited superior single-molecule magnet performance and pushed the development of single-molecule magnets into a new era. Since there is only one metal paramagnetic center, they are also called single-ion magnets (SIMs).

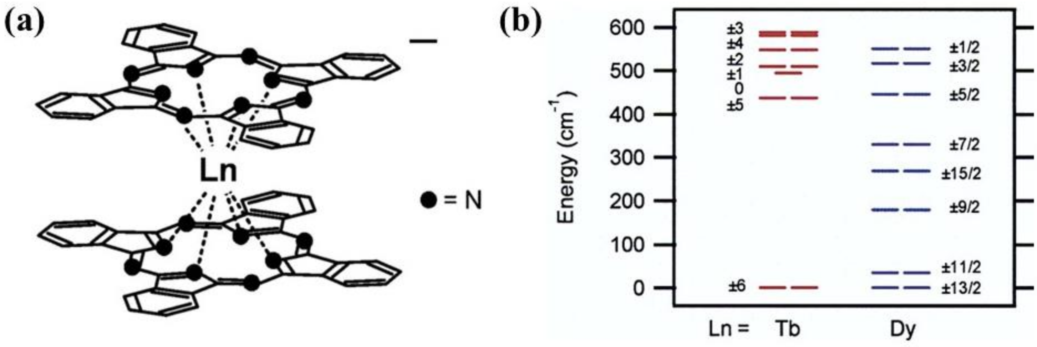

Figure 1.7. The molecular structure of $[Pc_2Ln]^-$. (Ln = Tb, Dy) (a). Energy diagram for the ground-state multiplets of $[Pc_2Ln]^-$ (Ln = Tb, Dy) (b); Copyright © 2003, American Chemical Society.

As shown in Figure 1.7, the central Ln^{III} ion is sandwiched by two Pc ligands. Both lanthanide complexes exhibit slow magnetization relaxation behavior. The spin reversal energy barriers of the dilute complexes are 230 cm^{-1} and 28 cm^{-1} for $[Pc_2Tb]^-$ and $[Pc_2Dy]^-$, respectively. Compared with transition metal single-molecule magnets, the effective energy barrier of mononuclear lanthanides is significantly improved, which is mainly due to the strong magnetic anisotropy caused by the strong axial crystal field energy. Although $[Pc_2Tb]^-$ has an effective energy barrier of 230 cm^{-1}, its blocking temperature is only 1.7 K, which is due to the fast quantum tunneling effect. By using strong electron-donating and bulky dibutylamino groups, they synthesized a similar structure with an effective energy barrier raised to 652 cm^{-1} and a blocking temperature reached to 30 K. In 2010, Layfield et al. [86]reported a dinuclear compound of dysprosium cyclopentadiene bridged by a nitrogen-containing ligand. This was the first magnetic study of organometallic lanthanide compounds. Since then, research on dysprosium-based single-molecule magnets based on cyclopentadiene ligands has been driven, setting off a research boom.

Generally speaking, to obtain single-ion magnets with large effective energy barriers and high blocking temperatures, it is necessary to select appropriate ligands that can coordinate with Dy^{3+} ions (or other lanthanide ions) and place them in a highly symmetric coordination environment. This enhances the axial crystal field while maintaining a weak equatorial crystal field, thereby achieving high magnetic anisotropy.

For example, in 2016, Mingliang Tong's team[87] reported a pentagonal bipyramidal single-molecule magnet $Dy(Cy_3PO)_2(H_2O)_5$, by introducing Cy_3PO ligands in the axial direction to increase the axial crystal field energy. At the same time, the equator was composed of five water molecules and its blocking temperature was obtained at 20 K.

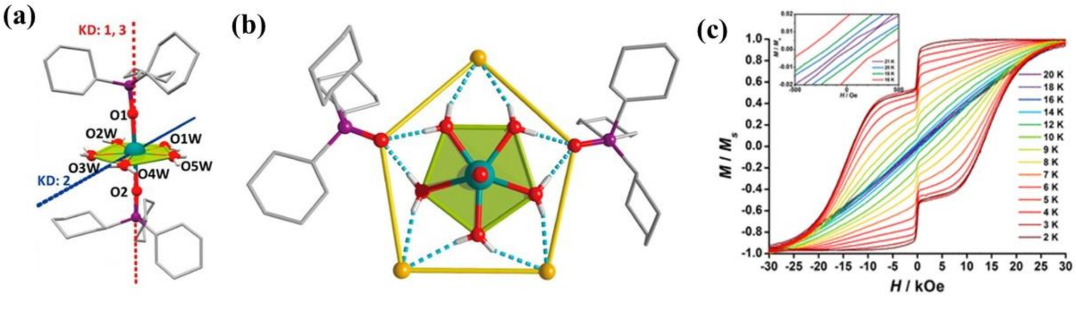

Figure 1.8. Crystal structure (left) and Magnetic hysteresis (right) of $Dy(Cy_3PO)_2(H_2O)_5$; Copyright © 2016, American Chemical Society.

In 2021, Jinkui Tang et al.[88] reported a hexagonal bipyramidal (D_{6h}) Dy(III) SMM, $[Dy(L^{N6})(Ph_3SiO)_2][BPh_4]$ (L^{N6} = 1,2-bis(2,4,6-trifluorophenyl)-ethane-1,2-diamine), in which fluorine atoms were introduced into the equatorial ligands to weaken the equatorial ligand field through electron-withdrawing effects, while simultaneously introducing Ph_3SiO groups axially to increase the axial crystal field, resulting in an effective energy barrier of 1800 K.

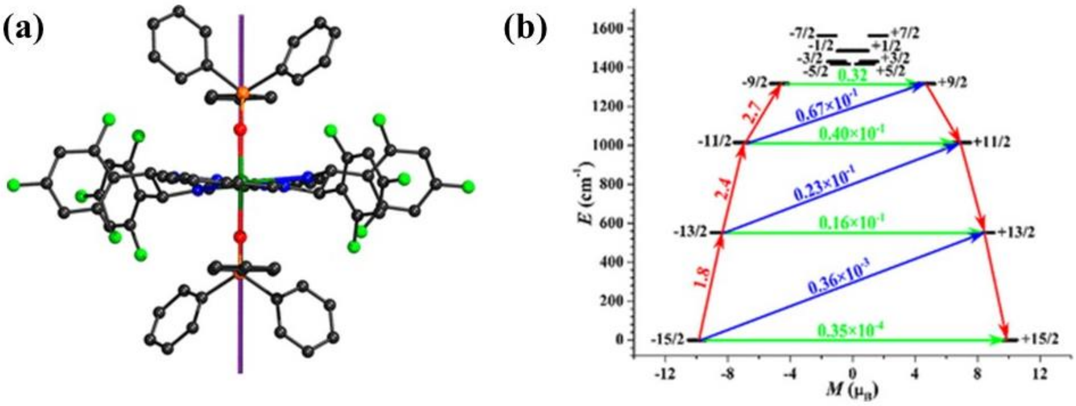

Figure 1.9. Crystal structure (left) and Energy barrier to magnetic relaxation (right) of $[Dy(L^{N6})(Ph_3SiO)_2]$; Copyright © 2021, American Chemical Society.

In addition to the above examples of weakening the equatorial crystal field energy, the linear sandwich structure based on cyclopentadiene has achieved remarkable results, which has greatly increased the blocking temperature of the single-molecule magnet from the previous 20 K to the threshold of 60 K, and further exceeded the upper limit of liquid helium temperature.

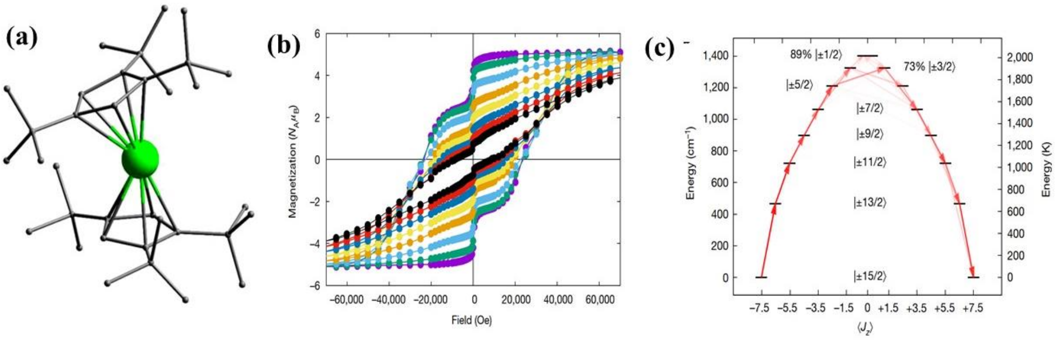

Figure 1.10. Crystal structure (left), Magnetic hysteresis (middle) and Energy barrier to magnetic relaxation (right) of $[Dy(Cp^{ttt})_2]^+$; Copyright © 2017, Springer Nature.

In 2017, Goodwin et al.[89] reported a new compound in Nature, $[Dy(Cp^{ttt})_2][B(C_6F_5)_4]$ (Cp^{ttt}, 1,2,4-tri-tert-butylcyclopentadieny) (Figure 1.10), which was a key breakthrough. This compound is only coordinated with two cyclopentadiene ligands, and there are no other ligands coordinated with it at the equator. This results in a strong axial crystal field, leading to a high magnetic anisotropy barrier of 1261 cm^{-1}. The opening temperature of the hysteresis loop reaches 60 K, and zero-field quantum tunneling is effectively suppressed. At 2 K, 83% of the remanence is retained, and the coercive field exceeds 2 T.

Subsequently, in 2018, Layfield et al. [90]reported a heteroleptic dysprosium metallocene cation $[(Cp^{iPr5})Dy(Cp^*)]^+$ (Cp^{iPr5} = pentaisopropylcyclopentadienyl, Cp^* = pentamethylcyclopentadienyl) , whose thermal cracking temperature exceeded the boiling point of liquid nitrogen (77 K) for the first time, thanks to the shorter Dy−Cp center-of-mass distance and more linear Cp center-of-mass−Dy−Cp center-of-mass angle compared to $[Dy(Cp^{ttt})_2]^+$.

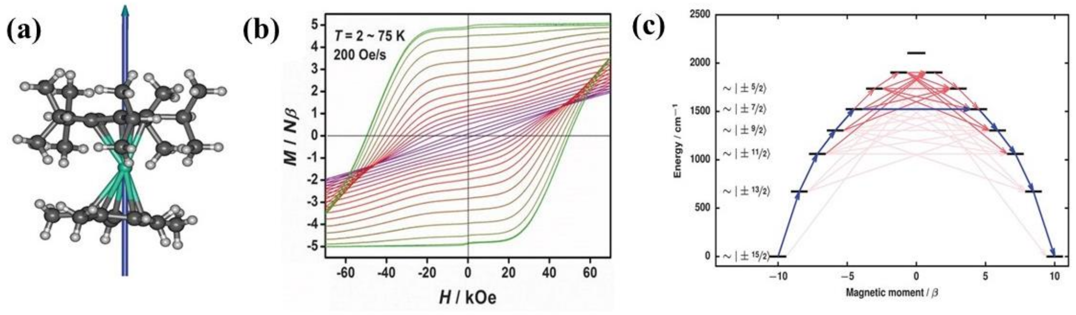

Figure 1.11. Crystal structure (a), Magnetic hysteresis (b) and Energy barrier to magnetic relaxation (c) of $[(CpiPr_5)Dy(Cp^*)]^+$; Copyright © 2018, American Association for the Advancement of Science.

This year, Nicholas F. Chilton of the Australian National University and his collaborators reported a dysprosium bis(amide)-olefin complex which shows $U_{eff} = 1{,}843(11)\ cm^{-1}$ and slow closing of soft magnetic hysteresis loops up to 100 K and a theoretical storage capacity of 3 Tb/cm².[20] The introduction of nitrogen-based axial ligands into the molecule stabilizes the otherwise easily bent structure, significantly enhancing its magnetic properties.

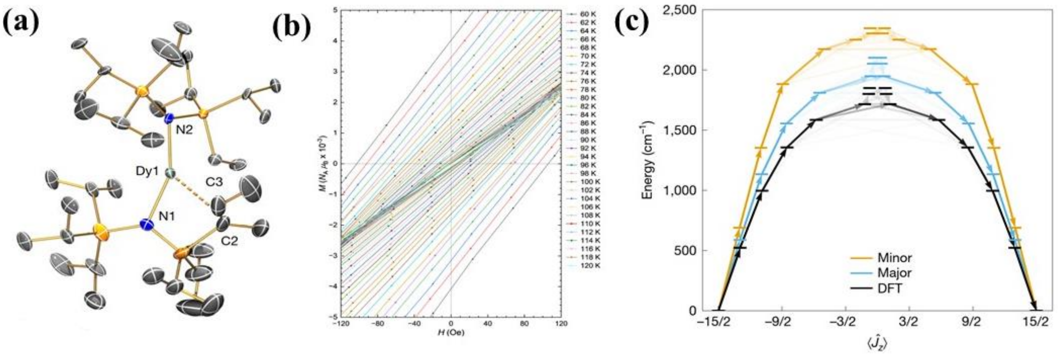

Figure 1.12. Crystal structure (left), Magnetic hysteresis (middle) and Energy barrier to magnetic relaxation (right) of $[Dy\{N(SiiPr_3)[Si(iPr)_2C(CH_3){=}CHCH_3]\}$; Copyright © 2025, Springer Nature.

1.4 Dinuclear Lanthanide Single-Molecule Magnets

Although single-ion magnets can achieve high performance through high molecular symmetry, quantum tunneling is often unavoidable. Dinuclear single-molecule magnets, on the other hand, have unique advantages in increasing the magnetic ground state, enhancing magnetic anisotropy, and suppressing quantum tunneling through exchange interaction to enhance magnetic coupling and increase energy level splitting, thereby achieving a large effective energy barrier[91-98].

As a model of dinuclear single-molecule magnets, which are usually arranged side by side or head to tail, we can regard each lanthanide ion as a bar magneton generating a set of magnetic field lines[99] (with north and south poles). (Figure1.13)

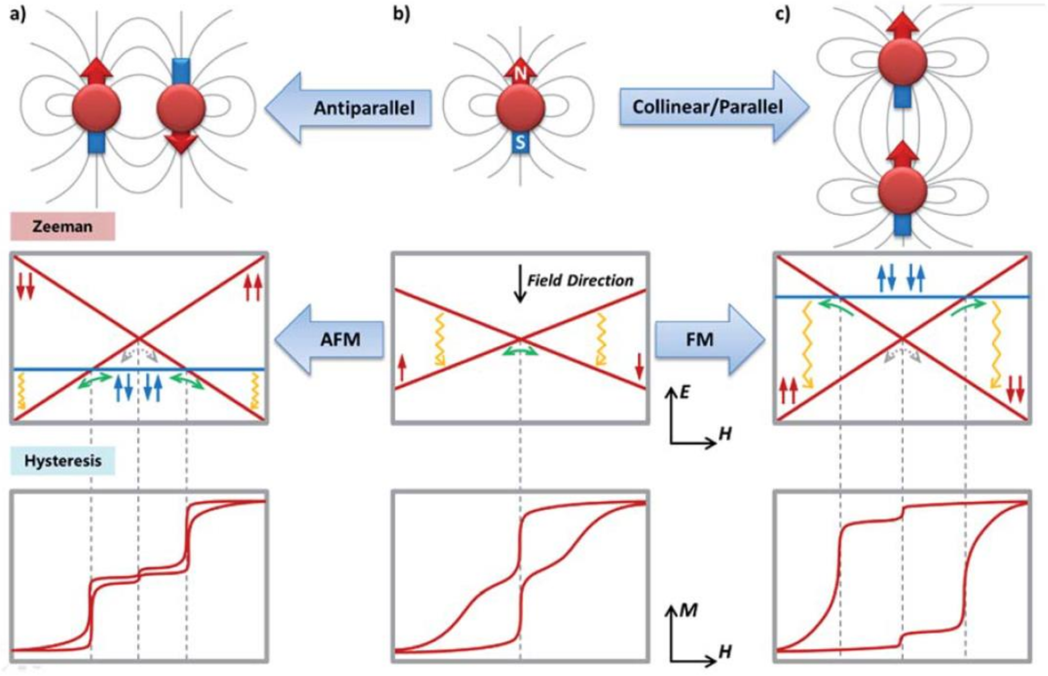

Figure 1.13. Three molecular magnetism models, hysteresis loops, and corresponding Zeeman diagrams; Copyright © 2022, The Royal Society of Chemistry.

For a single-ion magnet, a rapid magnetic moment reversal occurs near zero field, which manifests as a zero-field energy level crossing on the Zeeman diagram and a large jump in magnetization intensity at zero field on the hysteresis loop (Figure 1.13b). Compared to single-ion magnet models, dinuclear molecular magnets typically exhibit a side-by-side, antiparallel arrangement of the lanthanide anisotropic magnetic moments and a head-to-tail parallel arrangement of the lanthanide ion anisotropic magnetic moments. In this side-by-side, antiparallel arrangement of the lanthanide anisotropic magnetic moments, each anisotropic lanthanide ion generates a self-generated magnetic field, forming a built-in magnetic field. Under low external magnetic fields, an antiferromagnetic ground state is exhibited near zero field. When a sufficiently strong magnetic field is applied, it can reverse the antiparallel magnetic moments, thereby suppressing the zero-field quantum tunneling of magnetization (QTM), which is reflected in the hysteresis loop as a diamagnetic ground state at zero field (Figure 1.13a). Furthermore, in this head-to-tail parallel arrangement of the lanthanide anisotropic magnetic moments, the application of an external magnetic field requires the simultaneous reversal of both magnetic moments, reducing the probability of quantum tunneling at zero field and increasing the relaxation time, resulting in a wide hysteresis loop with large remanent magnetization and coercivity (Figure 1.13c).

In 2011, the Muralee Murugesu group[100] reported a trivalent lanthanide dimer $[Dy^{III}_2(valdien)_2(NO_3)_2]$ (H_2valdien = N1,N3-bis(3-methoxysalicylidene)diethylenetriamine) compound with an effective energy barrier at 76 K and exhibiting a weak antiferromagnetic interaction constant of $J_{Dy\text{-}Dy} = 0.21\ cm^{-1}$.

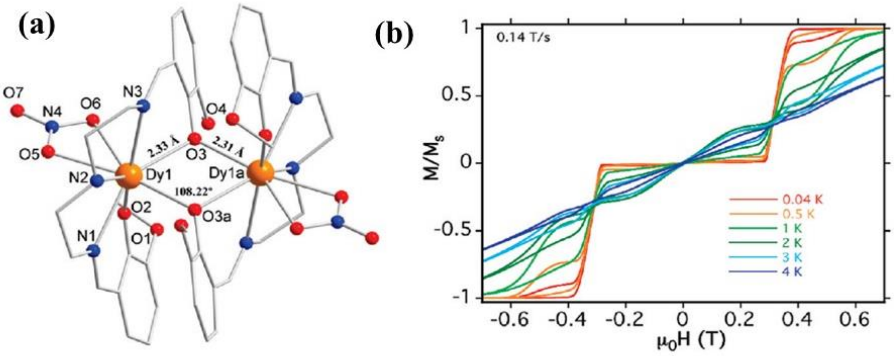

Figure 1.14. Crystal structure (left), Magnetic hysteresis (right) of $[Dy^{III}_2(valdien)_2(NO_3)_2]$ Copyright © 2011, American Chemical Society.

In 2011, Liviu F. Chibotaru's group [101]reported a new alkoxido-bridged asymmetric dinuclear Dy^{III} ferromagnetically coupled dimer, $[Dy_2(ovph)_2Cl_2(MeOH)_3]_3$·MeCN ($H_2$ovph = pyridine-2-carboxylic acid [(2-hydroxy-3-methoxyphenyl)methylene] hydrazide). At low enough temperature, the Dy_2 dimer enters the exchange-blocking regime, exhibiting a sluggish relaxation (τ_{QTM} = 35 s).

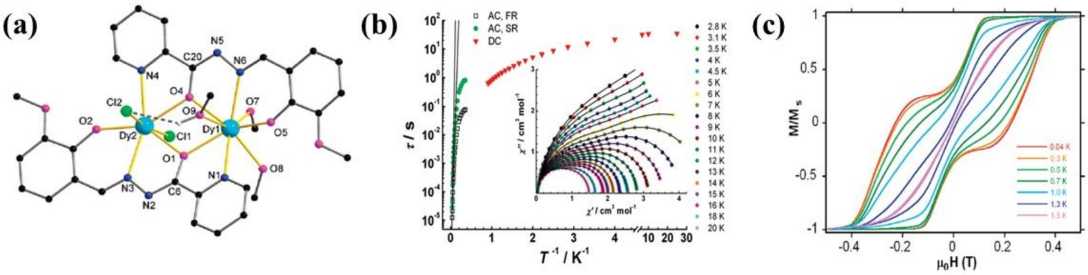

Figure 1.15. Crystal structure (left), Arrhenius plot and inset: Cole-Cole plot (middle) and hysteresis loop (right) of $[Dy_2(ovph)_2Cl_2(MeOH)_3]_3$·MeCN Copyright © 2011, American Chemical Society.

Radical-bridged lanthanide dimer single-molecule magnets have been a hot topic in recent decades. Radical ligands offer unique performance advantages, which carry unpaired electrons with their own spin, which exchange with the unpaired electrons of the lanthanide metal ion to form a strong magnetic coupling. Manipulating the coordination environment with the metal center alters the local electron distribution and crystal field, thereby enhancing the magnetic anisotropy of the system.

The magnetic exchange between rare earth ions can be effectively enhanced by radical bridging. Based on this strategy, researchers used KC_8 to reduce the N_2^{2-} bridging group to N_2^{3-} radicals and synthesized a series of free radical-bridged single-molecule magnets. In 2011, Jeffrey R. Long's group[102] reported the first N_2^{3-} bridged radical single-molecule magnet, [K(18-crown-6)]{[$(Me_3Si)_2N]_2$(THF)Ln}$_2$(μ-η^2: η^2-N_2). The Dy compound exhibited an effective energy barrier of 123 cm⁻¹ and a blocking temperature of 8.0 K (Figure 1.16a). The presence of the N_2^{3-} bridged radical enables exceptionally strong magnetic exchange between lanthanide ions. Gd (III) exhibits strong magnetic coupling to this ion, while the incorporation of the highly anisotropic Dy (III) ion yielded a molecule with a record magnetic blocking temperature of 8.3 K at a scan rate of 0.08 T s⁻¹. At the same time, in the same year, Jeffrey R. Long reported another N_2^{3-} radical-bridged Tb(III) compound, {[$(Me_3Si)_2N]_2$(THF)Tb}$_2$(μ-η^2:η^2-N_2)[103], which exhibited magnetic hysteresis at 15 K and a 100 s blocking temperature of 13.9 K (Figure 1.16b). The results showed that the strong magnetic anisotropy of Tb (III) and the effective exchange coupling ability of N_2^{3-} radicals synergistically create hard molecular magnets. By comparing with the non-radical-bridged AC magnetic susceptibility measurements, the magnetic exchange coupling hinders the zero-field fast relaxation path, thereby forcing the thermally activated relaxation behavior to occur over a wider temperature range. In 2017, Jeffrey R. Long's research group reported another N_2^{3-} radical bridged single-molecule magnet [K(crypt-

222)][$(Cp^{Me4H}{}_2Tb)_2(\mu{-}N_2)$][104], Pairing the axial magnetic anisotropy enforced by tetramethylcyclopentadienyl (Cp^{Me4H}) capping ligands with the strong magnetic coupling exchange provided by N_2^{3-} radical-bridging ligands, which reduces the coordination number of the metal center, appears to increase the axial magnetic anisotropy, resulting in a larger magnetic relaxation barrier. These complexes exhibit unusually large hysteresis loops, and these hysteresis loops remain stable at high temperatures, raising the 100-second magnetic blocking temperature to 20 K (Figure 1.14c).

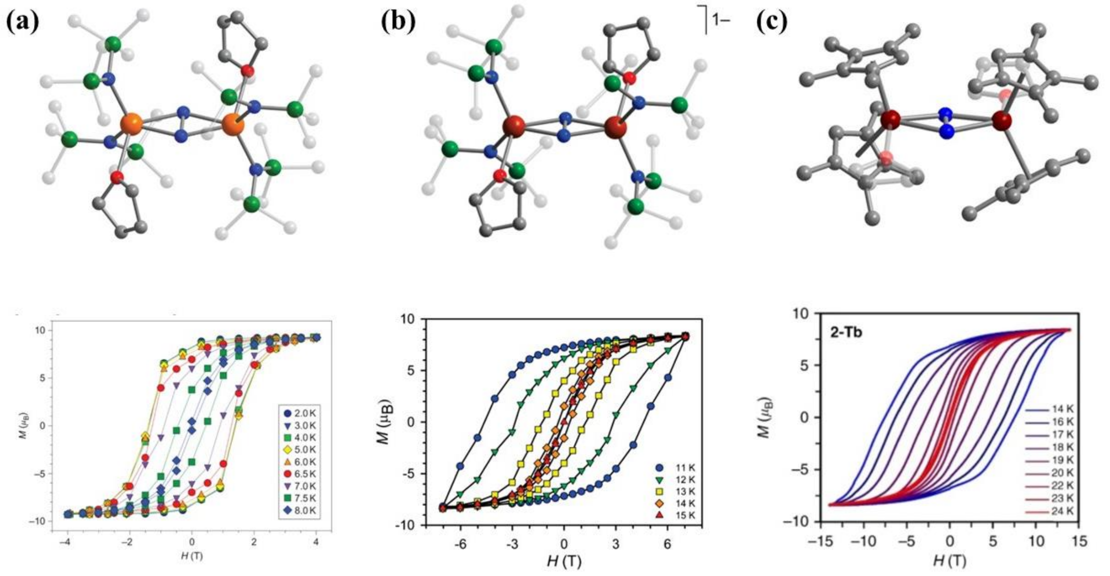

Figure 1.16. the structure (top) and hysteresis loop (down) of [$\{[(Me_3Si)_2N]_2Gd(THF)\}_2(\mu\text{-}\eta^2{:}\eta^2\text{-}N_2)$] (a) Copyright © 2011, Springer Nature ; $\{[(Me_3Si)_2N]_2(THF)Ln\}_2(\mu\text{-}\eta^2{:}\eta^2\text{-}N_2)$ (b) Copyright © 2011, American Chemical Society; and $[K(crypt\text{-}222)][(CpMe_4H_2Ln)_2(\mu{-}N_2)]$ (c) Copyright © 2011, Springer Nature.

In addition to using N_2^{3-} radicals as bridges to connect two lanthanide ions, in 2012, Jeffrey R. Long's group[105] reported a single-molecule magnet $[(Cp^*{}_2Ln)_2(\mu\text{-bpym}\bullet)]^+$ using 2,2′-bipyrimidine ($pbym\bullet^-$) as a bridge radical. Tb^{III} and Dy^{III} homologues exhibited single-molecule magnetic behavior with

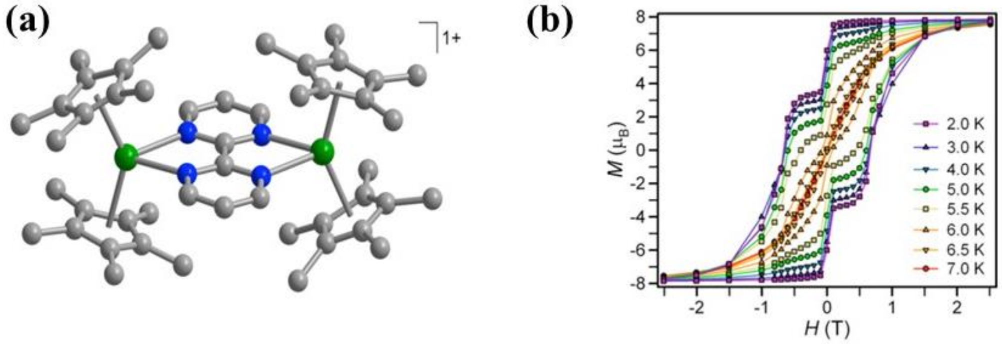

Figure 1.17. the structure (top) and hysteresis loop (down) of $[(Cp^*_2Ln)_2(\mu\text{-bpym}\bullet)]^+$ Copyright © 2012, American Chemical Society.

U_{eff} = 44(2) and 87.8(3) cm^{-1}, respectively, which was due to the large magnetic anisotropy imparted by these ions. It is worth noting that the Dy^{III} complex showed a difference in field-cooled and zero-field-cooled dc magnetic susceptibility data at 6.5 K, and exhibited magnetic hysteresis below this temperature.

1.5 Lanthanide Photoluminescence

Lanthanide ions are widely studied for their unique luminescence properties, with emission line spectra ranging from the visible to the near-infrared (NIR) and lifetimes from microseconds to milliseconds[106-107]. These emission properties are often exploited in fields such as bioimaging, optical communication devices, or materials science. The luminescence of trivalent lanthanide ions (Ln^{3+}) originates from 4f–4f electron transitions within partially filled $4f_n$ orbitals[108-111], with the exception of Ce^{3+}, which is characterized by 5d–4f radiative electron transitions. However, the f−f transitions are Laporte forbidden, resulting in a small molar absorption coefficient[112-113]. It requires the help of a ligand to effectively sensitize it. In general, the advantages of Ln^{3+} luminescence are[114-116]: (1) narrow linear emission; (2) long lifetime; (3) high quantum yield[117].

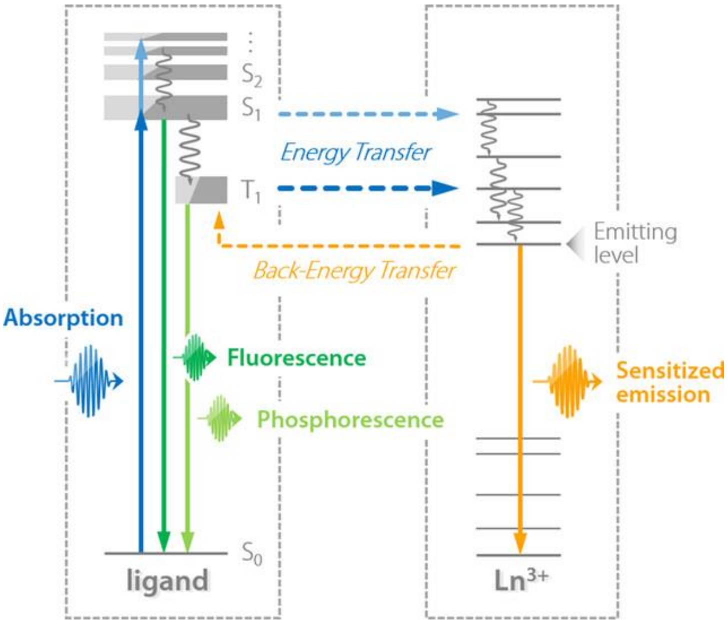

Figure 1.18. Schematic representation of the mechanisms involved in the luminescence of a Ln^{3+} ion in a complex; Copyright © 2021, Wiley-VCH Verlag GmbH.

The luminescence mechanism of trivalent lanthanide ions is as follows (Figure 1.18): the light absorption capacity of most organic ligands is far greater than that of trivalent lanthanide ions[118-121]. First, the ground-state electrons of the ligand absorb the light of a specific wavelength, gaining energy. Molecules are excited from the ground state to the singlet state (S1). Once the molecule is excited, it will undergo vibrational relaxation (VR) and return to its lowest excited state. Some of the excited-state molecules will undergo nonradiative transitions back to the ground state. Most molecules in the singlet state are unstable and return to the ground state, releasing energy as fluorescence. Additionally, some of excited molecules go from the singlet state (S1) to the triplet state (T1) through the intersystem crossing (ISC) [122-129]. Some of the excited-state molecules return to the ground state, and release energy as phosphorescence, while the remaining energy is transferred to the coordinated lanthanide ion. The excited-state ligand transfers energy to the coordinated lanthanide ion, which then releases the energy in the form of characteristic emission. [130-146].

For different trivalent lanthanide ions, when the energy level between the ion's emission level and the T1 level is comparable, energy is efficiently transferred from the ligand to the metal (LETM), maximizing the photoluminescence quantum yield[147-148]. These values are due to the fact that the transferred energy may be transferred back to the ligand through a thermally activated process (Figure 1.18), resulting in a decrease in the trivalent lanthanide ions energy level[149-158].

Therefore, the single electron and f-f electron transition characteristics of lanthanide ions in the 4f orbital give a unique advantages to generate single-molecule magnetism and photoluminescence properties. Combining these two properties in the same material has been a persistent pursuit of scientists for decades[159-168].

In 2022, Raju Mondal's group[169] reported a 3d-4f bifunctional compound $[Ln^{III}_2Zn^{II}_6(CPPC)_2(DMF)_8Cl_{10}](DMF)_2$ (H_2CPPC= (10E)-N′-[1-[6-[(E)-1-[5-(pyridin-2-yl)-1H-pyrazole-3-carboylimino]ethyl]pyridin-2-yl]ethylidene]-3-(pyridin-2-yl)-1H-pyrazole-5-carbohydrazide). The magnetic characteristics of the Dy_2Zn_6 complex confirmed its single-molecule magnetic behavior and had a suitable frequency- and temperature-dependent out-of-phase signal with a U_{eff} value of ~5 K (Figure 1.19b) and a relaxation time of 8.52×10^{-6} s. At the same time, the Eu_2Zn_6 and Tb_2Zn_6 complexes produced encouraging characteristic red and green photoluminescence properties, respectively. (Figure 1.19 c, d)

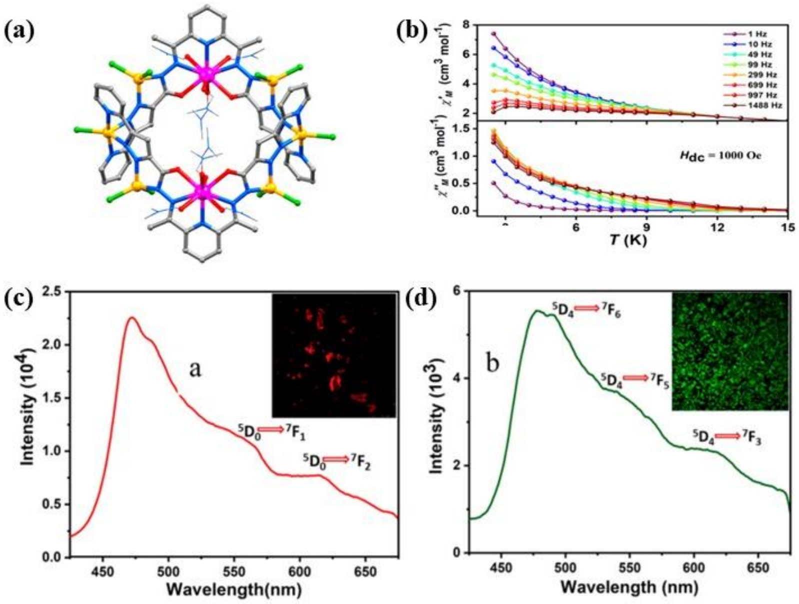

Figure 1.19. the structure (a), magnetic data (b), PL spectra of Eu_2Zn_6 and the Tb_2Zn_6 of $[Ln^{III}_2Zn^{II}_6(CPPC)_2(DMF)_8Cl_{10}](DMF)_2$ Copyright © 2022, American Chemical Society.

In addition to the examples mentioned above, research on lanthanide photomagnetism over the past decade has primarily focused on antenna ligands formed from divalent Zn and Schiff base complexes coordinated with lanthanides. This is primarily because divalent Zn has no d-d transition, which avoids luminescence competition with the f-f transition of lanthanide and causes luminescence quenching. In 2012, Jerome Long and his collaborators[170] reported a lanthanide luminescent single-molecule magnet $[Zn(NO_3)(L)Dy(NO_3)_2(H_2O)]$ (H_2L = *N,N'*-bis(3-methoxysalicylidene)-1,2-diaminoethane)). Temperature and frequency dependence of the out-of-phase component of the AC magnetic susceptibility at this optimal field revealed a single frequency-dependent peak associated with slow relaxation of the magnetization, with an effective energy barrier of 39.41 K. The photoluminescence properties were studied and revealed a distinct emission peak characteristic of trivalent dysprosium ions (Figure 1.20a).

A similar work was reported in 2016 by Enrique Colacio and collaborators[171]. They reported a photoluminescent single-molecule magnet material [ZnBrDy(L)(ovan)(NO_3)(H_2O)] with L = *N,N'*-2,2-dimethylpropylenedi(3-methoxysalicyli-deneiminato) as the host ligand. This compound exhibited a frequency-dependent inverse magnetic susceptibility (χ''_M), with a peak at 27 K at the highest frequency used (10,000 Hz). Luminescence studies were also conducted, revealing that the compound exhibited characteristic emission peaks typical of trivalent dysprosium. Interestingly, the blue emission intensity from the $^4F_{9/2} \rightarrow {}^6H_{15/2}$ transition was much stronger than the yellow emission intensity from the $^4F_{9/2} \rightarrow {}^6H_{13/2}$ transition (Figure 1.20b).

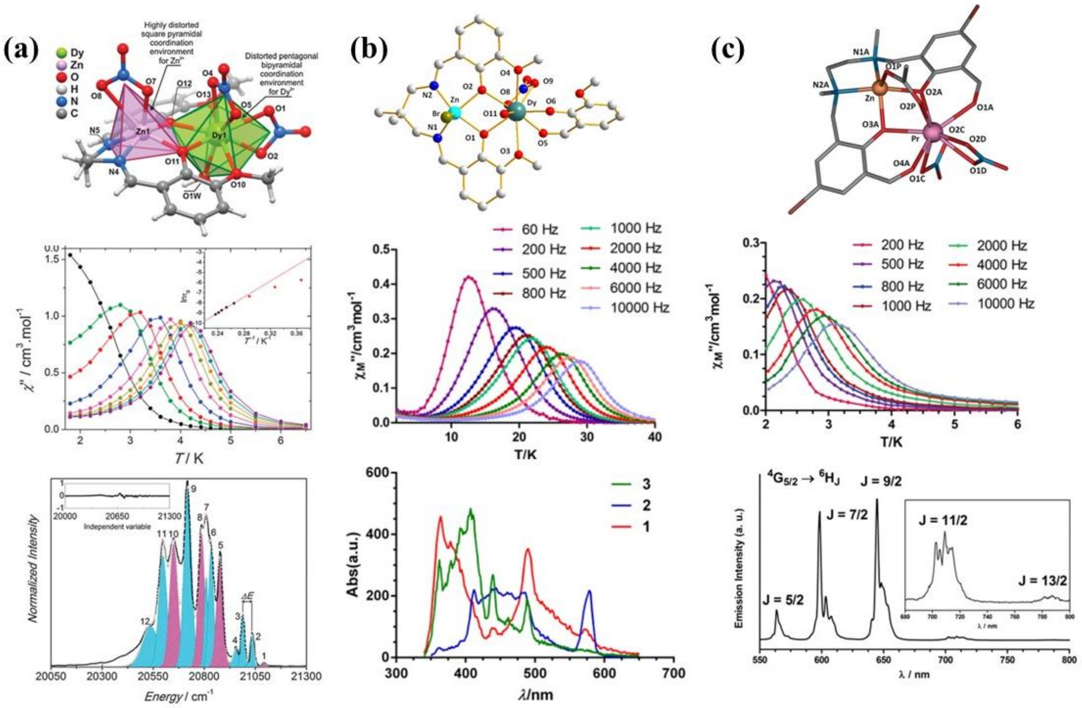

Figure 1.20. The structure (top), the out-of-phase susceptibility plot (middle) and the Sensitized emission spectra of complexes: (a) [Zn(NO_3)(L)Dy(NO_3)$_2$(H_2O)] (L=*N,N'*-bis(3-methoxysalicylidene)-1,2-diaminoethane) Copyright © 2012, The Royal Society of Chemistry; [(LZnBrDy(ovan)(NO_3)(H_2O)](H_2O)·0.5(MeOH)(b) Copyright © 2016, American Chemical Society; [Zn(μ-L)(μ-OAc)Ln(NO_3)$_2$] (C) Copyright © 2016, The Royal Society of Chemistry.

In 2016, Ánrique Colacio and his collaborators[172] reported another photoluminescent single-molecule magnet material, [Zn(μ-L)(μ-OAc)Ln$(NO_3)_2$]·CH_3CN, based on the Zn-Schiff base antenna ligand *N,N′*-dimethyl-*N,N′*-bis(2-hydroxy-3-formyl-5-bromo-benzyl) ethylenediamine. This material exhibited slow magnetization relaxation, with the maximum out-of-phase signal (χ''_M) ranging from 2 K (1000 Hz) to 4.25 K (10,000 Hz). Simultaneously, its isostructural compound, Eu, exhibited characteristic emission peaks (Figure 1.20c).

1.6 Motivation

The main objective of this thesis is to advance the development of multifunctional lanthanide-based molecular materials through the use of varied synthetic and structural strategies, with the main focus on single-molecule magnetism, but also addressing the relationship between molecular structure and luminescent properties.

A molecule $[Dy_2(psq)_4(MeOH)_2(NO_3)_2]$ which has been under investigation in the Powell group for many years. The original compound was synthesized by Dr. Thomas Kriese[173]. Two further PhD students Dr. Anthony Blue Carter and Dr. Jonas Braun[174] have since worked on this system. Dr. Carter succeeded in developing a robust synthetic procedure for the system and Dr. Braun managed to extend the family of compounds by varying structural parameters such as the solvent-derived co-ligand. This is the starting point for the work presented here, in which the main aim was to introduce axial neutral co-ligands in order to tune the magnetic properties of this family of SMMs.

The magnetic behavior of dinuclear lanthanide–9,10-phenanthrenesemiquinone radical complexes is tuned by replacing axial ligands with designed donors such as triphenylphosphine oxide (tppo) and tricyclohexylphosphine oxide (tcypo), allowing a systematic evaluation of how axial coordination affects magnetic anisotropy and slow relaxation. Moreover, the semiquinone ligand framework is expanded from phsq$^{\cdot -}$ to pysq$^{\cdot -}$, enabling the influence of a larger π-system and increased rigidity on single-molecule magnet performance to be examined. In parallel, the scope of lanthanide SMMs is broadened by synthesizing a series of Ln-complexes so that promising ions other than Dy^{3+} can be identified. In another strategy, transition metals are introduced into classical DOTA-based structures, and DOTA derivatives with additional coordination sites are prepared to generate new 3d–4f heterometallic systems with both magnetic and luminescent properties. Overall, these varied strategies are used to establish clear relationships between molecular structure and physical properties, thereby underpining the rational design of advanced lanthanide magnetic and luminescent materials.

Chapter 2. Single-Molecule Magnet Behavior in Lanthanide–9,10-semiquinonate Radical Complexes

2.1 Introduction

In recent decades, radical single-molecule magnets have been a hot research topic, with a particular focus on nitrogen-based radical SMMs. Radical-bridging can effectively enhance the magnetic exchange between rare earth ions given the enhanced overlap between 2p and 4f orbitals when compared to direct 4f-4f overlap. Based on this strategy, researchers used KC_8 (potassium graphite) to reduce N_2^{2-} bridging groups to N_2^{3-} radicals[102-104], synthesizing a series of radical-bridged single-molecule magnets. In the S = 1/2 N_2^{3-} radical-bridged dinuclear Ln (III) monomolecular magnet $\{[(Me_3Si)_2N]_2(THF)Ln\}_2(\mu\text{-}\eta^2\text{:}\eta^2\text{-}N_2)]^-$ (Ln = Gd, Tb, Dy), there is a strong magnetic exchange coupling (J_{ex}=-27 cm^{-1}) between the Ln (III) ions, which effectively suppresses zero-field quantum tunneling[102].

This chapter is focused on the 9,10-phenanthrenequinone ligand. By introducing triphenylphosphine oxide (tppo) or tricyclohexylphosphine oxide (tcypo) ligands along with the 9,10-phenanthrene semiquinone (phq) ligand, 12 dinuclear air-stable radical lanthanide compounds (Ln = Ce, Nd, Sm, Eu, Gd, Tb, Dy, Ho, Er, Tm, Yb, Lu) were obtained. The compounds using Sm to Lu are isostructural. In contrast, the larger atomic radii of Ce and Nd compared to the other lanthanide ions result in a different arrangement of the $phsq^-$ ligands. In the following, the structures of the Nd, Dy, and Tb analogues are described and their magnetic properties characterized. In particular, theoretical magnetic data for Dy complex were calculated using CASSCF.

2.2 Structure and Characterization of $[Dy_2(phsq)_4(tppo)_2(NO_3)_2]$

2.2.1 Cystal structure of $[Dy_2(phsq)_4(tppo)_2(NO_3)_2]$

This compound can be prepared in sealed vessels without the need for exclusion of air or water, producing stable, dark crystals. Single crystal X-ray diffraction analyses show that all compounds are isomorphous, crystallizing in the triclinic space group P-1. Each centrosymmetric dinuclear lanthanide molecule, bridged by four phsq$^-$ ligands (Figure 2.1), is generated from half of the molecule in the asymmetric unit by inversion symmetry. The lanthanides are nine-coordinate in a capped square-antiprismatic O_9 geometry. Among them, 6 oxygen atoms come from four radical phsq$^{\cdot -}$ ligands, another oxygen atom comes from the tppo ligand, and the other two oxygen atoms come from the nitrate ion. A feature of this compound is the surprisingly strong inter-radical interaction between pairs of 9,10-phenanthrenequinone units with the shortest carbon-carbon (C2-C4) distance being just 2.683(4) Å, significantly shorter than twice the van der Waals radius of carbon at 3.40 Å, and the same is also true for the closest oxygen-oxygen (O2-O4) distance of 2.579(3) Å. The Dy---Dy distance of 3.425 (2) Å is significantly shorter than the distances observed in similar compounds in the literature which are usually at least 3.700 Å[175-180].

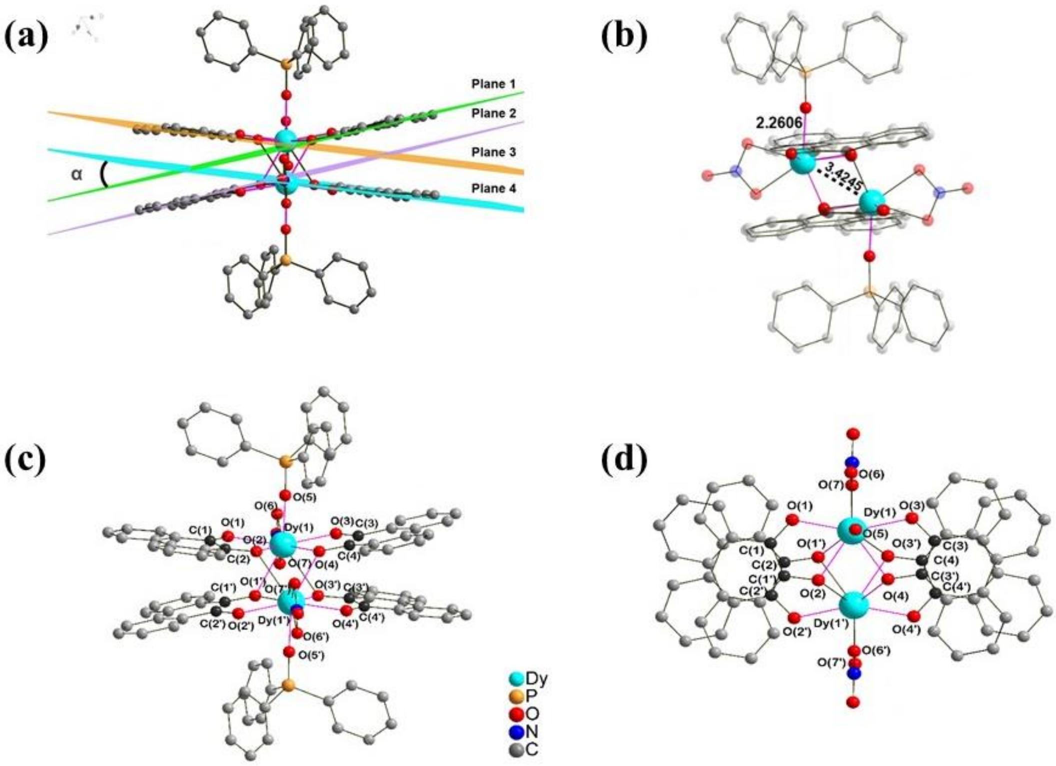

Figure 2.1. Top views(left) and coordination environment of Dy atoms (right) of the molecular structure of [$Dy_2(phsq)_4(tppo)_2(NO_3)_2$]; organic H-atoms omitted for clarity.

It can be seen from Figure 2.1 that the four radical ligands tightly bind the two Dy ions together, wrapping them together. Figure 2.1 right shows the coordination environment of Dy, where the axial Dy-O bond length is 2.261 Å, which is shorter than most Dy-O bond lengths.

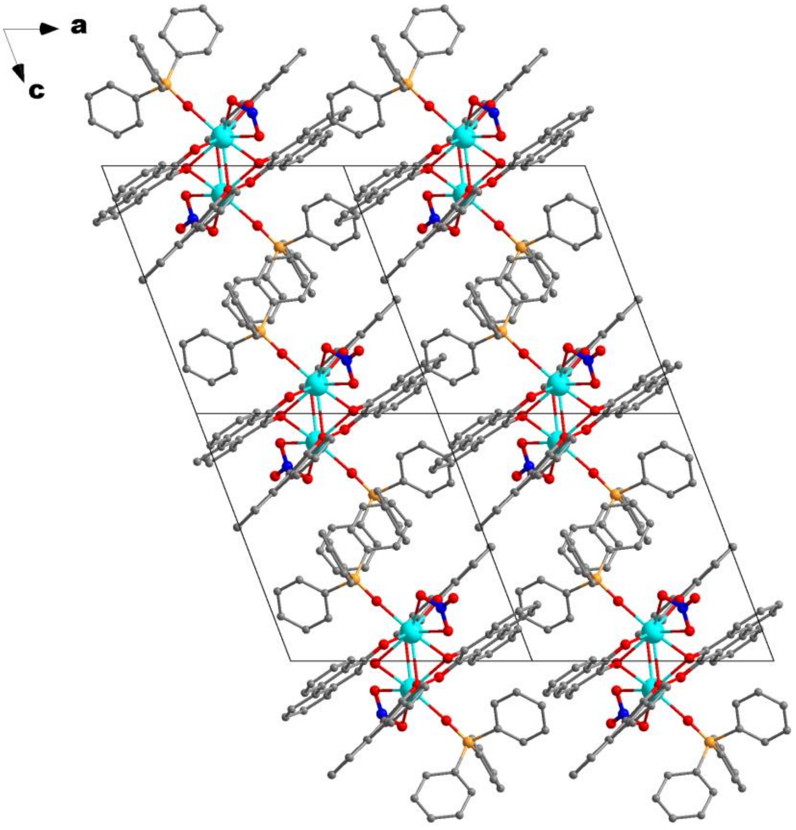

Figure 2.2. Overall views of the molecular structure of $[Dy_2(phsq)_4(tppo)_2(NO_3)_2]$; organic H-atoms omitted for clarity.

Based on the structural perspective in figure 2.1, we found that the angle between the two radical phsq·⁻ ligands on the same side is α = 20.126 ° (between plane 1 with plane 4 or between plane 2 with plane 3). In addition, as we can be seen from the Figure 2.2, the arrangement of the entire structure is consistent, which makes it possible to construct a large magnetic anisotropy.

2.2.2 Bulk purity (PXRD) and ATR-IR spectroscopic analysis

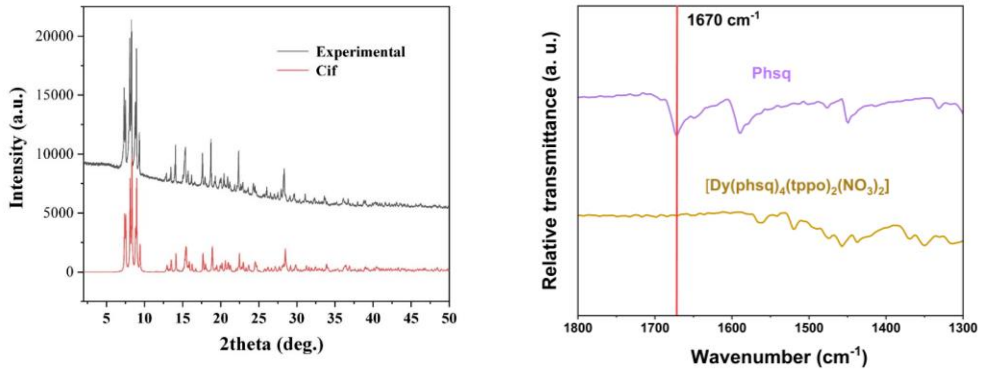

Figure 2.3. Powder-XRD (left) and ATR-IR (right) of the $[Dy_2(phsq)_4(tppo)_2(NO_3)_2]$ compound

The powder-XRD data show a perfect match between the experimental data and the structural simulation data (Figure 2.3). The infrared spectra show a characteristic C=O peak at 1670 cm^{-1}. In some compounds, the peak at 1670 cm^{-1}, compared to the characteristic peak of the ligand phsq, has disappeared, suggesting that the carbonyl has been hydrated. This also indicates that the sample is without unreacted phq ligand precursor (Figure 2.3).

2.2.3 Evidence for radicals in $[Dy_2(phsq)_4(tppo)_2(NO_3)_2]$

How can we determine whether the coordinating ligand in the $[Dy_2(phsq)_4(tppo)_2(NO_3)_2]$ compound is a kind of radical ligand? The raw quinone-type ligand, psq, generally undergoes two transformations: a semiquinone-type ligand and a diol-type ligand, as shown in Figure 2.4. The three redox states of phenanthrenequinone can be distinguished by bond length. As shown in Table 2.1, the characteristic bond lengths of the three redox states of phenanthrenequinone are annotated. Specifically, the variation in bond length B makes it easy to distinguish the three oxidation states of the compound: approximately 1.2 Å for the quinone type, approximately 1.3 Å for the semiquinone type, and approximately 1.4 Å for the diol type.

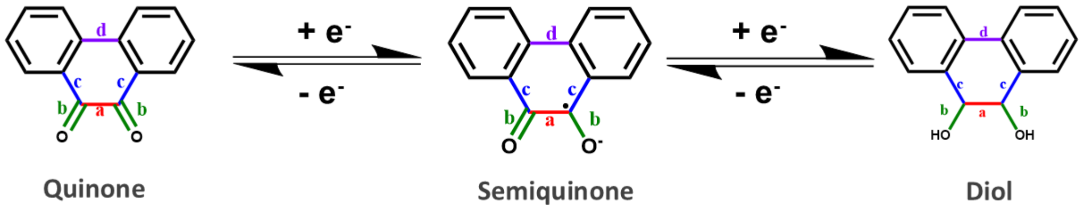

Figure 2.4. Phenanthrenesemiquinonate radical ligand with the significant bonds a, b, c, d to determine the radical character.

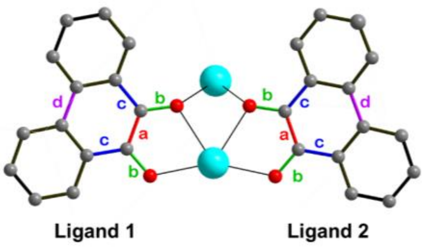

Figure 2.5. Coordinated ligand of the Dy_2 dimer with the significant bonds a, b, c, d to determine the radical character.

	a	b	c	d
Quinone	1.541(3)	1.208(4)	1.459(5)	1.499(5)
Semiquinone	1.438(3)	1.293(2)	1.446(3)	1.471(3)
Diol	1.345(3)	1.383(2)	1.432(3)	1.461(3)
ligand 1	1.448(5)	1.268(7)	1.449(6)	1.461(7)
ligand 2	1.444(1)	1.273(4)	1.456(9)	1.466(2)

Table 2.1. Comparison of selected bond lengths (Å) of the semiquinone ligands coordinated to Dy in the crystallography of $[Dy_2(phsq)_4(tppo)_2(NO_3)_2]$ (ligand 1 (bonds a, b, c, d) and ligand 2 (bonds a, b, c, d)) with the corresponding bond lengths from the

literature for 9,10-phenanthrenequinone, 9,10-phenanthrene semiquinone, and phenanthrene-9,10-diol.

In addition, by comparing the bond lengths of the ligands in the compound, we found that the bond length characteristics of the $[Dy_2(phsq)_4(tppo)_2(NO_3)_2]$ compound (Table 2.1) are consistent with the bond length characteristics of the semiquinone type compound, and the semiquinone type is the only one with radical characteristics, so it can be determined that the compound contains semiquinone radicals.

2.2.4 Magnetic properties of $[Dy_2(phsq)_4(tppo)_2(NO_3)_2]$

Direct current (dc) magnetic susceptibility measurements were performed on microcrystalline samples of $[Dy_2(phsq)_4(tppo)_2(NO_3)_2]$ in the range 2−300 K under applied magnetic fields of 0.1 T and 1 T. The room temperature $\chi_M T$ value of 27.13 cm^3 K mol^{-1} is close to the theoretical value of 28.34 cm^3 K mol^{-1} for two noninteracting free Dy^{III} ions (ground state $^6H_{15/2}$, S = 5/2, L = 5, and g = 4/3). The χ_MT product remains almost constant until ~100 K, then it decreases smoothly upon further cooling until ~30 K, and more sharply at the end, reaching a value of 6.5 cm^3 K mol^{-1} at 2 K for 0.1 T, and reaching a value of 8 cm^3 K mol^{-1} at 2 K for 1 T (Figure 2.6 left). The rapid decline of the χ_MT product upon lowering the temperature is likely due to the depopulation of the crystal field m_J sub-levels and intramolecular antiferromagnetic interactions between the two Dy^{III} ions[181-182].

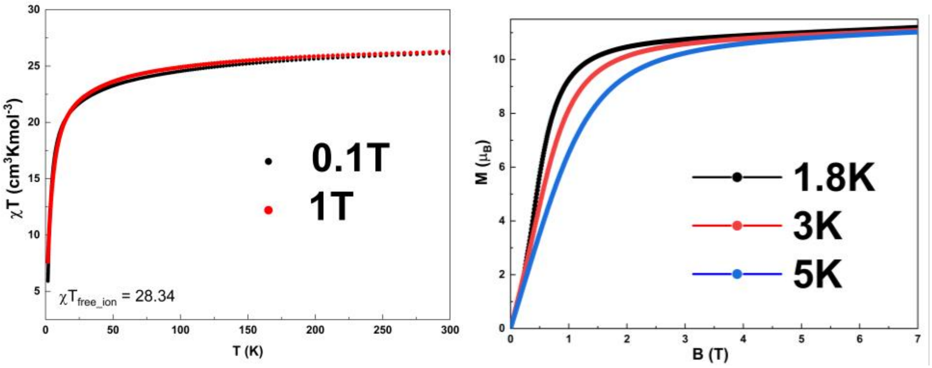

Figure 2.6. χ_MT vs T (left) plot of [$Dy_2(phsq)_4(tppo)_2(NO_3)_2$] (right) obtained at temperatures between 1.8 and 300 K with an applied magnetic dc field of 0.1 T and 1 T. Plots of M vs. H (right) at different temperatures.

In the reduced magnetisation plots the curves do not overlap suggesting significant anisotropy and/or the presence and involvement of low-lying excited states. The magnetizations of [$Dy_2(phsq)_4(tppo)_2(NO_3)_2$] complex measured using applied magnetic fields at 1.8, 3 and 5 K reveal a rapid increase at low magnetic fields up to 2.0 T (Fig 2.6 right). At high magnetic fields, magnetization increases gradually and finally reaches ca. 10.95 μ_B at 7 T (Figure 2.6 right), which almost achieves the expected saturation value of 5 μ_B for an Ising-like Dy^{III}[183].

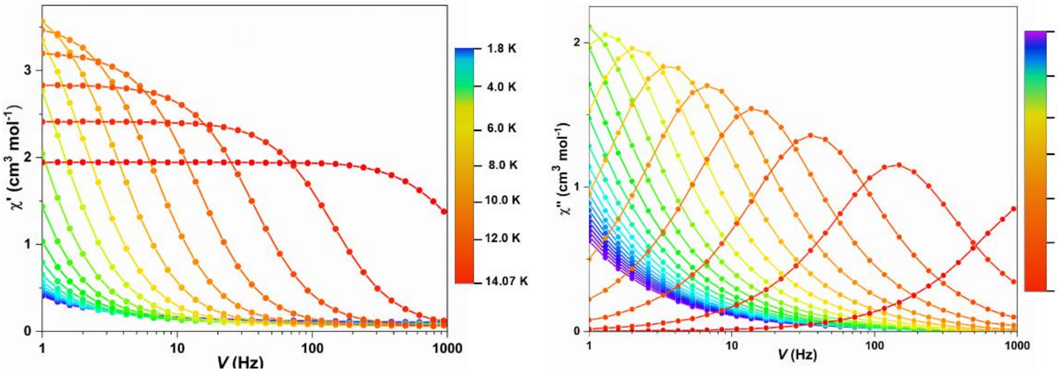

Figure 2.7. In- and out-of-phase susceptibility at ac field frequencies between 1 and 1000 Hz and temperatures between 1.8 and 14 K of [$Dy_2(phsq)_4(tppo)_2(NO_3)_2$] (left and right, respectively).

AC susceptibility experiments were conducted at zero applied DC field in the temperature range 1.8 K to 14.07 K (Figure 2.7). Slow relaxation of magnetization can be observed with maxima in the out-of-phase susceptibility in measurements with ac fields switching direction at frequencies between 1 and 1000 Hz, which indicates the existence of a slow magnetization relaxation phenomenon characteristic of to SMMs. A generalized Debye model was used to analysize the relaxation processes.

The Cole-Cole plot approximates a semicircle (Figure 2.8 left), consistent with the generalized Debye model. From this the relaxation times of complex [$Dy_2(phsq)_4(tppo)_2(NO_3)_2$] can be extracted at different temperatures as shown in Figure 2.8 right. The plot of ln(τ) versus 1/T deviates from a straight line and exhibits a bend at high temperatures, indicating the presence of Raman and Orbach processes.

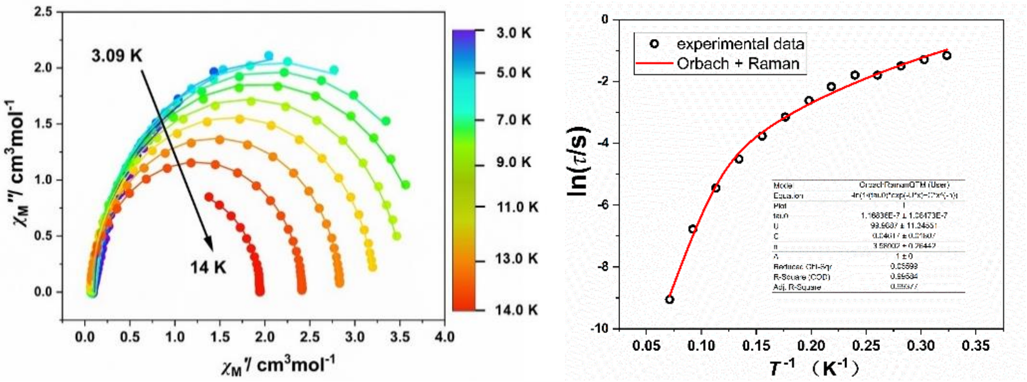

Figure 2.8. Cole-Cole plot at different temperatures (left). ln(τ) versus T^{-1} for [$Dy_2(phsq)_4(tppo)_2(NO_3)_2$], solid red line represents the best-fit for magnetization relaxation (right).

Equation	$\tau^{-1} = AT + B + CT^{n} + \tau_0{}^{-1}\, exp^{-\frac{U_{eff}}{K_B T}}$
A	0
B	0
C	0.04617 ± 0.01807
n	3.58902 ± 0.26442
$\boldsymbol{\tau_0}$	1.16836E-7 ± 1.08473E-7
U_{eff}	99.9887 ± 11.34551
Reduced Chi-Sqr	0.03599
R-Square (COD)	0.99584
Adj. R-Square	0.99377

Table 2.2. Fitting parameters for the relaxation process of figure 2.8 right

A plot of the natural logarithm of ln(τ) versus 1/T (Figure 2.8 right) shows a linear relationship at high temperatures, indicating that thermally activated spin reversals cross a potential energy barrier, commonly known as Orbach relaxation. This relaxation exhibits an exponential temperature dependence according to the formula [$\tau_0{}^{-1}$exp ($-U_{eff}/k_B T$)], where τ_0 is the pre-exponential factor, k_B is the Boltzmann constant, and U_{eff} is the effective barrier to magnetic relaxation. Thus, the relaxation barrier can be estimated by extracting the slope of the temperature-dependent Arrhenius plot. The temperature dependence of the relaxation time was investigated, revealing a strong temperature dependence at high temperatures and a power-law temperature dependence at low temperatures, indicating exponential (Orbach-like) and Raman relaxation mechanisms, respectively (Figure 2.8 right). The relationship between ln(τ) and 1/T can be modeled using Equation (1),

$$\tau^{-1} = \tau_0{}^{-1}\, exp^{-\frac{U_{eff}}{K_B T}} + CT^{n} \qquad (1)$$

where the Orbach [$\tau_0^{-1}\exp(-U_{eff}/k_BT)$] and Raman ($CT^n$) relaxation processes were taken into account. A best fit was obtained for [$Dy_2(phsq)_4(tppo)_2(NO_3)_2$] yielding the parameters τ_0 = 1.17 x 10^{-7} s, U_{eff} = 99.99 K (69.5 cm^{-1}), C = 0.04617 K^{-n} s^{-1}, n = 3.589 (table 2.2). This means that the QTM relaxation process is effectively suppressed. Generally, QTM occurs at low temperatures. Therefore, we will use Micro-SQUID at ultra-low temperatures to further verify whether the QTM process is suppressed.

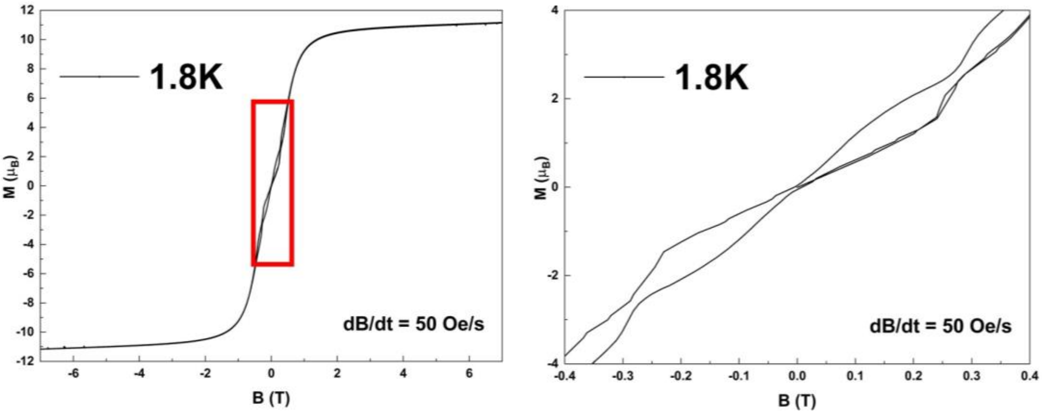

Figure 2.9. Hysteresis loop (left) and narrow hysteresis near zero field shown by [$Dy_2(phsq)_4(tppo)_2(NO_3)_2$] at 1.8 K between fields of -0.4 and 0.4 T indicating SMM behavior at this temperature

We measured the hysteresis loop at 1.8 k and found that the plots a hysteresis opens at temperatures 1.8 k near zero applied dc field (Figure 2.9), which means that the compound exhibits single-molecule magnetic behavior at temperatures below 1.8 K, which would mean that the hysteresis loop of the [$Dy_2(phsq)_4(tppo)_2(NO_3)_2$] complex would also be open at lower temperatures. Therefore, we further conducted Micro-SQUID measurement to investigate the magnetic behavior at lower temperatures. Micro-SQUID measurements on single crystals of the [$Dy_2(phsq)_4(tppo)_2(NO_3)_2$] complex were performed. At the center of the plots a hysteresis opens at temperatures between 0.03 and 0.3 K that is sweep rate independent indicating slow relaxation behaviors and excluding the possibility of ZFQTM in line with the results of the fit to the Arrhenius plot above, which is also confirmed in the first-order derivative graph (Figure 2.10c). At a field strength of ± 0.25 T, the magnetization of $[\mathrm{Dy_2(phsq)_4(tppo)_2(NO_3)_2}]$ increases vertically, indicating the occurrence of quantum tunneling at level crossing, as clearly visible in the derivative plot (Figure 2.10 c). As shown, an antiferromagnetic ground state[184-185] exists within the field strength range of -0.25 to 0.25 T, further confirming that quantum tunneling is effectively suppressed near zero field. This suppression of QTM was attributed to the presence of a strong dipolar bias-field between the Dy ions in a recent publication from the Powell group[186].

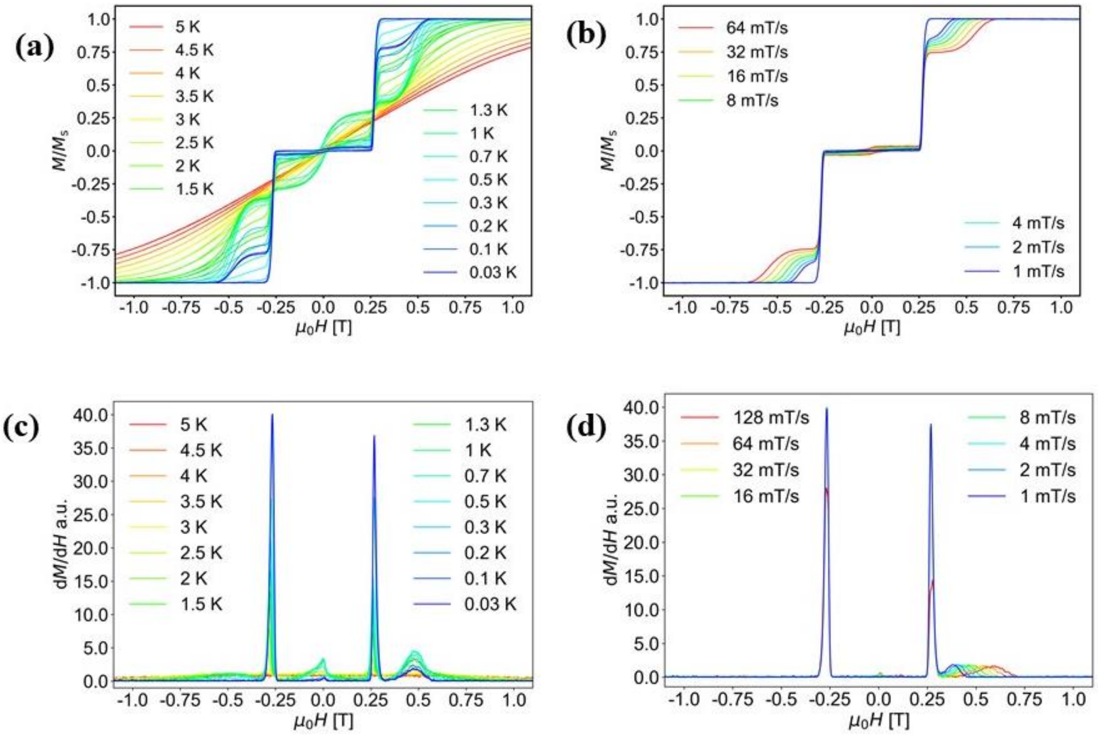

Figure 2.10. Micro-SQUID measurements performed on single crystals of $[\mathrm{Dy_2(phsq)_4(tppo)_2(NO_3)_2}]$. Temperature dependence between 0.03 and 5 K (a) and sweep rate dependence between 1 and 128 mT/s (b). Derivative plots (c,d) for both dependencies highlighting the switching field of the level crossing from the essentially non-magnetic ground state.

2.2.5 Quantum chemical caculations

In order to understand the mechanism of magnetic relaxation of Dy dimer, CASSCF[187] calculations were performed on the Dy dimer compound using MOLCAS 8.2 and SINGLE_ANISO program. First, the χT and M(B) data of $[Dy_2(phsq)_4(tppo)_2(NO_3)_2]$ are fitted (it is likely that the solvent molecules are not taken into account so that the curve does not reach the theoretical value). After applying a scaling factor, it perfectly fits the experimental data (Figure 2.11a). We found that at this level of theory, the exchange interaction between two Dy sites (effective S = 1/2) is only 0.098 cm^{-1} (and does not exceed 1 cm^{-1}), which means that the dipole-dipole term dominates the Dy-Dy interaction.

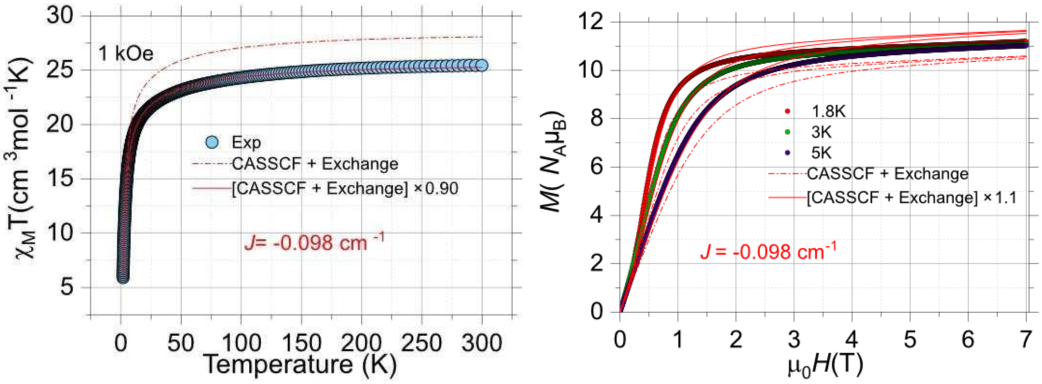

Figure 2.11. Left: Experimental susceptibility (dashed line) and ab initio calculation with CASSCF/SO-RASSI/POLY_ANISO approach (red solid line). Right: Experimental (dashed lines) vs. calculated (solid line) magnetization data of $[Dy_2(phsq)_4(tppo)_2(NO_3)_2]$ complex. The red, green and blue lines correspond to the data at 1.8K, 3K and 5K, respectively.

Comparing the hysteresis loops obtained by the Micro-SQUID with the Zeeman plots obtained through theoretical calculations revealed a perfect match. Levels crossings occur at an external field of approximately ±0.25 T, indicating a reversal of the magnetic moment, i.e., quantum tunneling[188-190]. However, at zero field, further magnetic moment reversals are suppressed. Therefore, the suppression of QTM at zero field was confirmed by the caculation of the Zeeman-splitting (Figure 2.12) and results from an internal dipolar magnetic field.

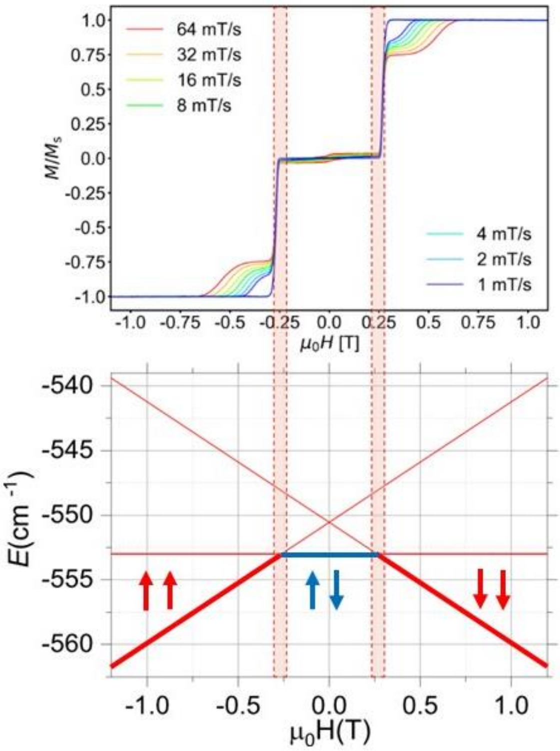

Figure 2.12. Micro-SQUID measurements of [Dy$_2$(phsq)$_4$(tppo)$_2$(NO$_3$)$_2$] (top) with the corresponding Zeeman plot (bottom)

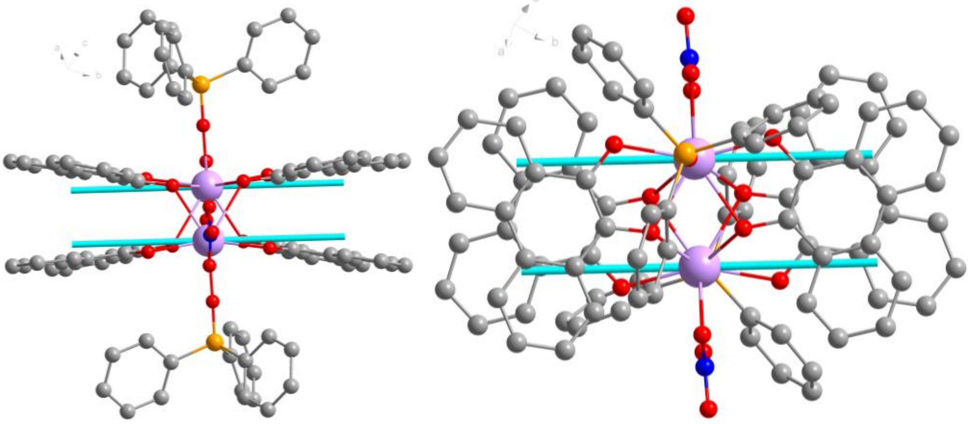

Figure 2.13. The side view (left) and top view (right) of anisotropy axes of the Dy^{III} ions in [Dy$_2$(phsq)$_4$(tppo)$_2$(NO$_3$)$_2$] calculated using MAGELLAN

The anisotropy axes of $[Dy(phsq)_4(tppo)_2(NO_3)_2]$ were calculated using MAGELLAN[191] (Figure 2.13). The axes are essentially orthogonal to the Dy-Dy vector which, means the dipolar interaction will be antiferromagnetic, which is consistent with the experimental results.

2.2.6 Magnetic properties of Y-doped $[Dy_xY_{(1-x)}(phsq)_4(tppo)_2(NO_3)_2]$

To further confirm that quantum tunneling in the Dy dimer is caused by the internal magnetic field arising from dipolar interactions, we replaced most of the Dy^{III} ions with diamagnetic Y^{III}. This substitution converts the Dy^{3+} dimer into a single-ion paramagnetic Dy system, effectively eliminating the internal antiferromagnetic field present in the original dimer. Therefore, we successfully obtained the Y-doped compound $[Dy_xY_{(1-x)}(phsq)_4(tppo)_2(NO_3)_2]$ by using 90% diamagnetic Y^{III} and 10% paramagnetic Dy^{III} as raw materials through molar ligands. Meanwhile, we also completely replaced Dy^{III} with Y^{III} and obtained isomorphic compounds of pure Y^{III}. These powder-XRD data show good agreement between the experimental pattern and the simulated pattern of $[Dy_2(phsq)_4(tppo)_2(NO_3)_2]$ (Figure 2.14). The pure Y^{III} sample did not exhibit single-molecule magnetic (SMM) behavior. Moreover, the Y^{III}-Dy^{III} sample with doping exhibited SMM properties.

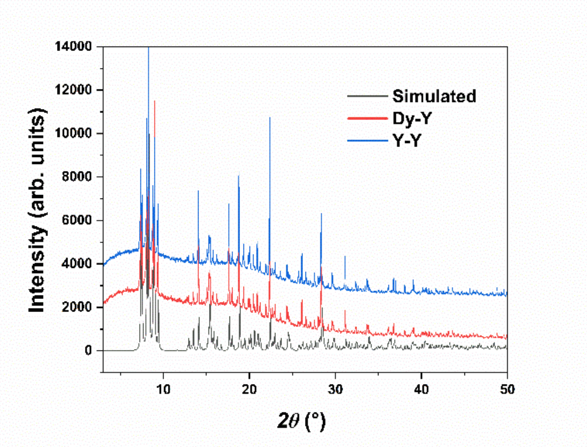

Figure 2.14. Comparison of powder-XRD patterns of the original

$[Dy_2(phsq)_4(tppo)_2(NO_3)_2]$ compound and Y^{III}-doped $[Dy_xY_{1-x}(phsq)_4(tppo)_2(NO_3)_2]$ samples.

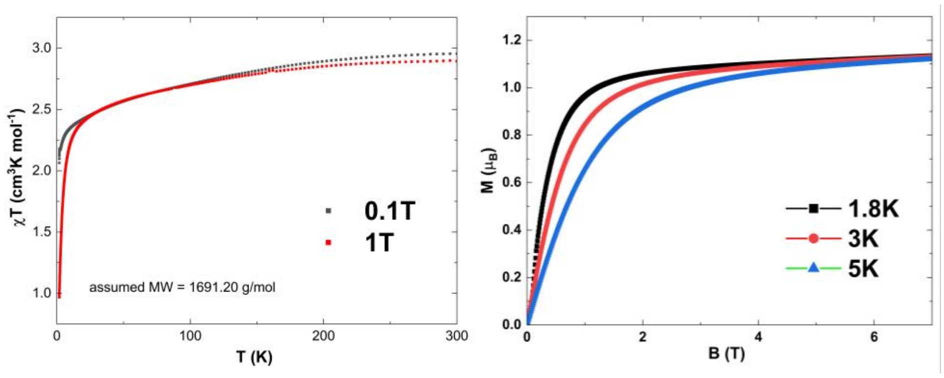

Figure 2.15. $\chi_M T$ vs T (left) plot of $[Dy_xY_{(1-x)}(phsq)_4(tppo)_2(NO_3)_2]$ (right) obtained at temperatures between 1.8 and 300 K with an applied magnetic dc field of 0.1 T and 1 T. Plots of M vs. H (right) at different temperatures.

Direct current (dc) magnetic susceptibility measurements were performed on microcrystalline samples of $[Dy_XY_{(1-x)}(phsq)_4(tppo)_2(NO_3)_2]$ in the range of 2−300 K under an applied magnetic field of 0.1 T and 1 T. The $\chi_M T$ product decreases smoothly upon further cooling until ~30 K (Figure 2.15 left). There is an antiferromagnetic interaction between Dy. The field dependence of magnetization for $[Dy_xY_{(1-x)}(phsq)_4(tppo)_2(NO_3)_2]$ was measured in the 0-7 T field range and at different temperatures. The magnetizations of $[Dy_xY_{(1-x)}(phsq)_4(tppo)_2(NO_3)_2]$ complex measured against applied magnetic fields at 1.8, 3 and 5 K reveal a rapid increase at low magnetic fields (Fig 2.15 right).

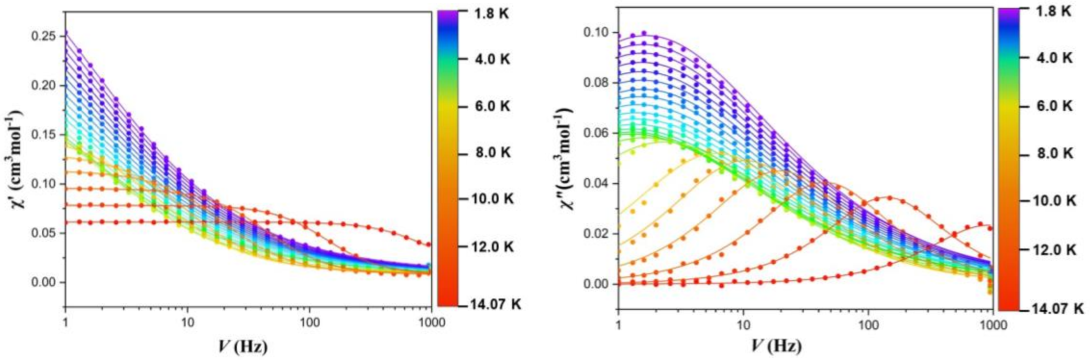

Figure 2.16. In- and out-of-phase susceptibility at ac field frequencies between 1 and 1000 Hz and temperatures between 1.8 and 14 K of $[Dy_xY_{(1-x)}(phsq)_4(tppo)_2(NO_3)_2]$ (left and right, respectively).

AC susceptibility experiments were conducted at zero applied dc field in the temperature range 1.8 K to 14.07 K (Figure 2.16). Slow relaxation of magnetization can be observed with maxima in the out-of-phase susceptibility in measurements with ac fields switching direction at frequencies between 1 and 1000 Hz, which indicates the existence of a slow magnetization relaxation phenomenon characteristic of SMMs.

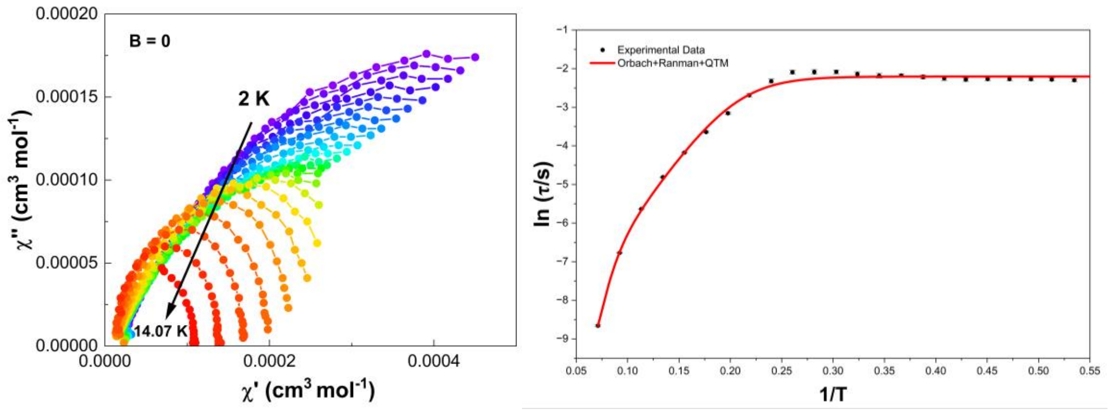

Figure 2.17. Cole-Cole plot at different temperatures (left). ln(τ) versus T^{-1} for $[Dy_xY_{(1-x)}(phsq)_4(tppo)_2(NO_3)_2]$, solid red line represents the best-fit for magnetization relaxation (right).

Equation	$\tau^{-1} = AT + B + V\frac{e^{\frac{-w}{K_B T}}}{\left(e^{\frac{-w}{K_B -1}}\right)^2} + \tau_0{}^{-1}\, exp^{-\frac{U_{eff}}{K_B T}}$
A	0
B	9.0598
C	16721.62067
n	36.79105
τ_0	1.48315E-8
U_{eff}	135.80182

Reduced Chi-Sqr	0.21647
R-Square (COD)	0.9968
Adj. R-Square	0.99613

Table 2.3. Fitting parameters for the relaxation process of Figure 2.17 right

In the relaxation process graph of the natural logarithm of ln(τ) and 1/T, we can see that a clear platform appears in the fitting curve in the low-temperature region, which means that the QTM relaxation process under zero field has been observed (Figure 2.17). We fit the experimental data based on the following equation (2):

$$\tau^{-1} = AT + B + V\frac{e^{\frac{-w}{K_BT}}}{\left(e^{\frac{-w}{K_B-1}}\right)^2} + \tau_0{}^{-1}\, exp^{-\frac{U_{eff}}{K_BT}} \qquad (2)$$

where there are multiple relaxation process including the Orbach [$\tau_0{}^{-1}$exp (-$U_{eff}/k_B{}^T$)] , Raman ($V\frac{e^{\frac{-w}{K_BT}}}{\left(e^{\frac{-w}{K_B-1}}\right)^2}$) ,Direct($AT$) and QTM ($B$) relaxation processes. A best fit was obtained for [$Dy_xY_{(1-x)}(phsq)_4(tppo)_2(NO_3)_2$] yielding the parameters τ_0 = 2.94 x 10^{-8} s, U_{eff} = 135.00 K, V = 16721.62 s^{-1}, W = 36.79 K (Table 2.3). Therefore, the Orbach and Raman process were taken into account. Meanwhile, the QTM relaxation process is effectively observed again, and $\tau_{QTM} = 0.11\,s$. Therefore, in this system, when the majority of the paramagnetic Dy (III) ions are replaced by diamagnetic Y (III) ions, the quantum tunneling effect (QTM) suppressed under zero field will be observed again. The above result will be further confirmed using Micro-SQUID.

Micro-SQUID measurements on single crystals of [$Dy_XY_{(1-x)}(phsq)_4(tppo)_2(NO_3)_2$] complex were performed (each single crystal containing 81% Y_2, 18% Dy-Y, and 1% Dy_2 when assuming Dy and Y ions react with the same rate). At the center of the plots a hysteresis opens at temperatures between 0.03 and 0.2 K that is sweep rate independent indicating slow relaxation behavior. Most importantly, the magnetization of $Dy_2(Rad)_4$ increases vertically under zero field, indicating the occurrence of quantum tunneling, as clearly visible from the derivative plot (Fig. 2.18c). The quantum tunneling effect under zero field was observed again. Therefore, this further confirmed that the quantum tunneling of $[Dy_2(phsq)_4(tppo)_2(NO_3)_2]$ under zero field was effectively suppressed due to the internal magnetic field of the dipole in the dimer.

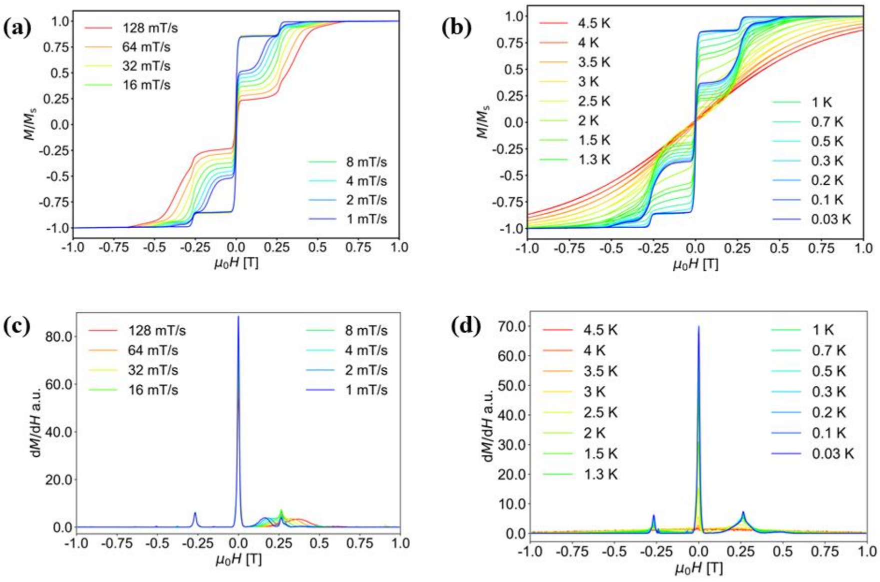

Figure 2.18. Micro-SQUID measurements performed on single crystals of Y-doping. Temperature dependence between 0.03 and 5 K (a,b) and sweep rate dependence between 1 and 128 mT/s (c,d).

2.3 Structure and Characterization of $[Nd_2(phsq)_4(tppo)_2(NO_3)_2]$

2.3.1 Crystal structure of $[Nd_2(pysq)_4(tppo)_2(NO_3)_2]$

The same method was used to synthesize the radical phsq-tppo complexes of Nd^{III} and Ce^{III}, which form a twisted isomer with an alternative arrangement of the phsq$\cdot^-$ radicals. Compared with Dy^{III} ions, the larger ionic radii of Ce^{III} and Nd^{III} are likely to alter the arrangement of the radical ligands [192]. Powder -XRD data analysis showed that the compounds of Ce^{III} and Nd^{III} are isomorphic. The Nd^{III}_2 dimer is used as an example to illustrate the structural characteristics of this system. The compound crystallizes in the space group Iba2. In the non-centrosymmetric molecular unit, the two Nd^{III} ions are tightly bound by four semiquinone radical $phsq^-$ ligands and are additionally bridged by oxygen atoms (figure 2.19a,b). Similar to the structure of Dy^{III}_2, each Nd^{III} ion is coordinated by nine oxygen atoms, forming an O9 coordination geometry. Six of these oxygen atoms are provided by the radical $phsq^-$ ligands, two by nitrate ions, and one by the axial tppo ligand. Compared to the structure of Dy^{III}_2, the arrangement of the $phsq^-$ ligands is distorted. As shown in Figure 2.19, the angle between the radical ligands on the same side is 17.88°. The semiquinone ligands on opposite sides of each Nd ion are arranged in a cross-like pattern, with an angle of 80.70° between them.

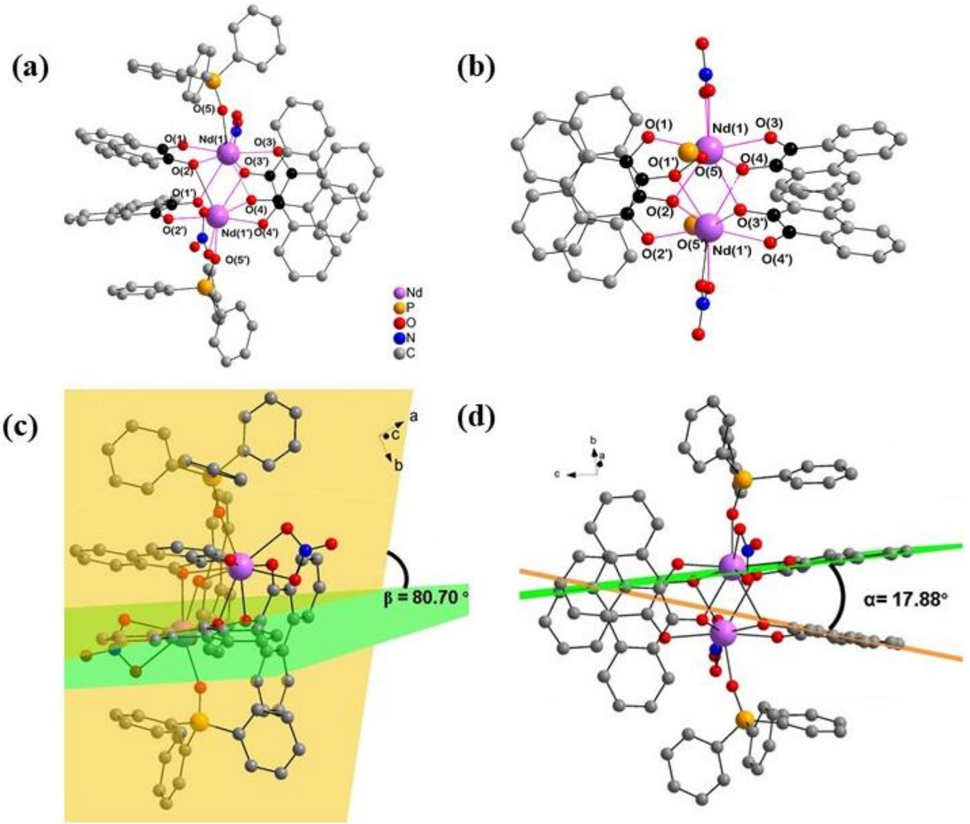

Figure 2.19. side views (a) and coordination environment of Nd atoms (b) of the molecular structure of $[Nd_2(phsq)_4(tppo)_2(NO_3)_2]$; organic H-atoms omitted for clarity.

Moreover, the Nd---Nd distance is 3.644 Å. In a system surrounded by four free radicals, the distance between O(1)-O(3) or O(2')-O(4') is 4.707 Å. The distance between O(2)-O(3') or O(1')-O(4) is 2.619 Å. The $Nd\text{-}O_{tppo}$ distance is 2.372 Å, which is longer than that in the Dy_2 dimer and likely a result of the larger ionic radius of Nd^{III} consequence of the lanthanide contraction (Figure 2.21). The packing arrangement of the structure is shown in Figure 2.20.

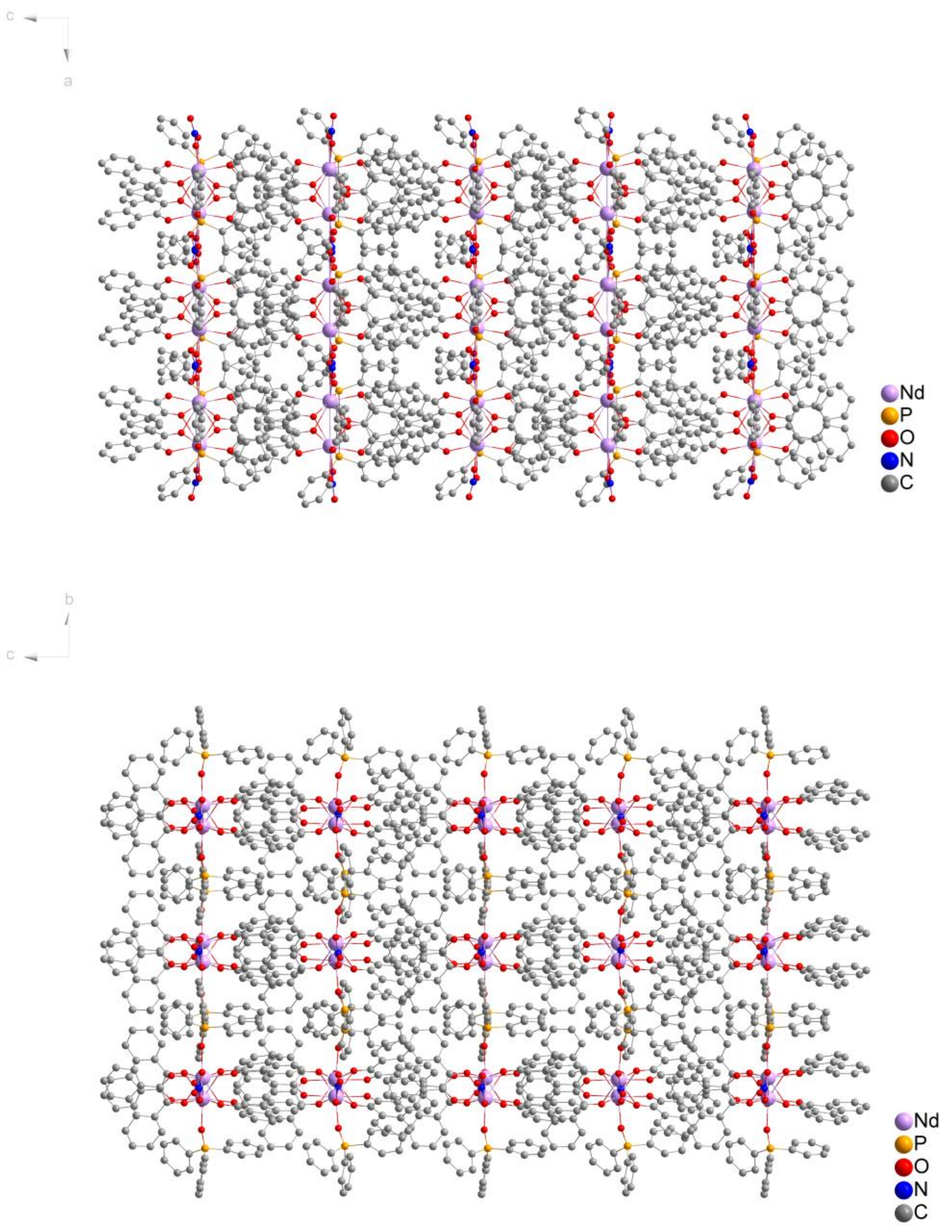

Figure 2.20. Crystal packing of the molecular structure of $[Nd_2(phsq)_4(tppo)_2(NO_3)_2]$; organic H-atoms omitted for clarity.

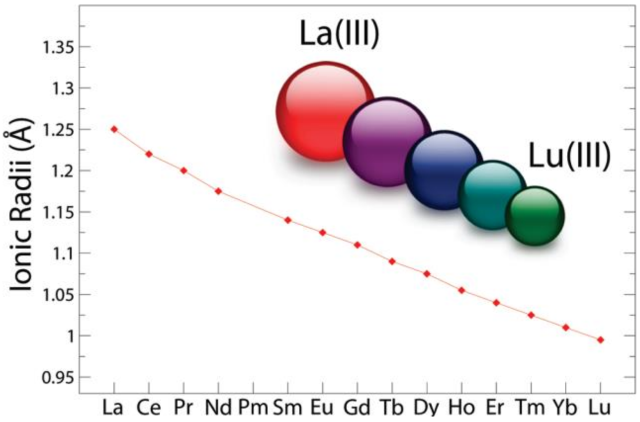

Figure 2.21. Comparison of ionic radii in the lanthanide series

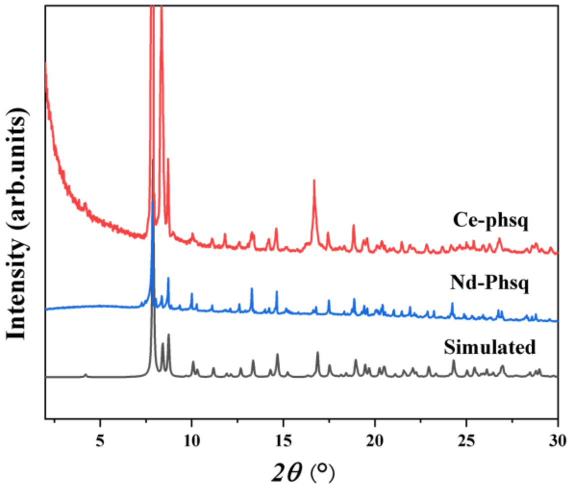

Figure 2.22. Powder-XRD patterns of $[Ln_2(phsq)_4(tppo)_2(NO_3)_2]$ compounds (Ln=Ce, Nd)

2.3.2 Magnetic properties of $[Nd_2(phsq)_4(tppo)_2(NO_3)_2]$

Direct current (dc) magnetic susceptibility measurements were performed on microcrystalline samples of $[Nd_2(phsq)_4(tppo)_2(NO_3)_2]$ in the range of 2−300 K under an applied magnetic field of 0.1 T and 1 T. The room temperature $\chi_M T$ value of 3.08 cm^3 K mol^{-1} is close to the theoretical value of 3.28 cm^3 K mol^{-1} for two noninteracting free Nd^{III} ions (ground state S = 3/2, L = 6, $^4I_{9/2}$, J = 9/2, *g* = 8/11, $\chi_M T_{Cacl}$ =1.64 cm^3 K mol^{-1}). The χ_MT product reduce gradually until ~3.8 K, then it increases sharply until 2 K under an applied 0.1 T DC field, reaching a value of 2.27 cm^3 K mol^{-1} at 2 K. In addition, the χ_MT product reduce gradually until ~3.5 K, then it increases slightly, and increases sharply until 2 K under an applied 1 T dc field, reaching a value of 1.76 cm^3 K mol^{-1} at 2 K (Figure 2.23 left). With decreasing temperature, the χ_MT value decreases gradually, probably due to the progressive depopulation of the excited Stark sublevels, which means the depopulation of the crystal field m_J sub-levels and the intramolecular ferromagnetic interactions between the two Nd^{III} ions[193].

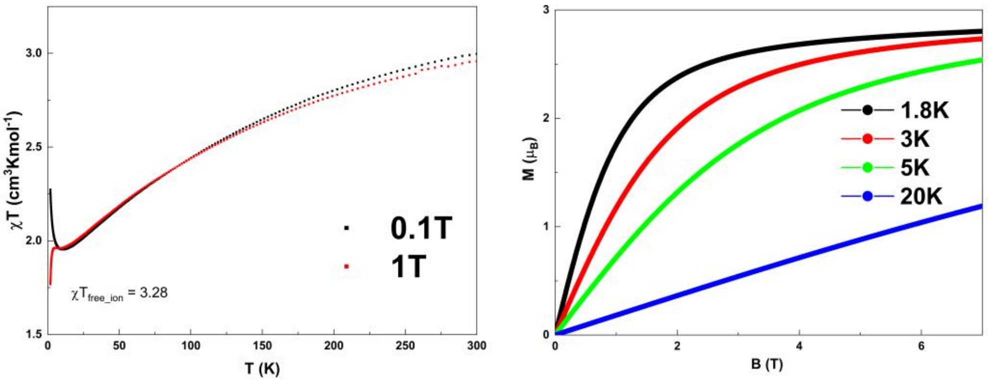

Figure 2-23. χ_MT vs T (left) plot of [$Nd_2(phsq)_4(tppo)_2(NO_3)_2$] (right) obtained at temperatures between 1.8 and 300 K with an applied magnetic dc field of 0.1 T and 1 T. Plots of M vs. H (right) at different temperatures.

The field dependence of magnetization for [$Nd_2(phsq)_4(tppo)_2(NO_3)_2$] was measured in the 0-7 T field range and at different temperatures. The magnetization of the [$Nd_2(phsq)_4(tppo)_2(NO_3)_2$] complex against applied magnetic fields at 1.8, 3 and 5 K reveal a rapid increase at low magnetic fields (Fig 2.23 right). The maximum value of 2.85 μ_B was observed at 1.8 K and 7 T, lower than the theoretical saturated value of 3 μ_B (S = 7/2) expected for two independent Nd (III) ions which can be attributed to the ligand-field-induced splitting of the Stark levels as well as the magnetic anisotropy.

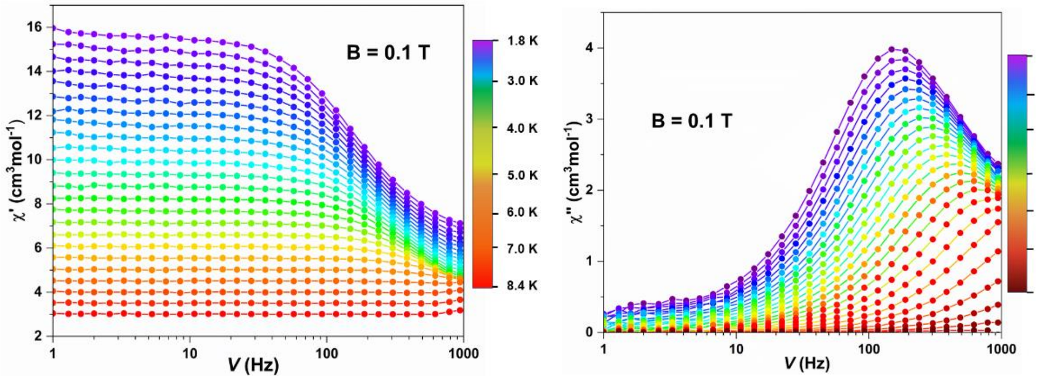

Figure 2.24. In- and out-of-phase susceptibility at ac field frequencies between 1 and 1000 Hz and temperatures between 1.8 and 8.4 K of [Nd$_2$(phsq)$_4$(TPPO)$_2$(NO$_3$)$_2$] (left and right, respectively).

Alternating current (ac) susceptibility experiments were conducted at 0.1 T applied dc field in the temperature range 1.8 K to 8.4 K (Figure 2.24). Slow relaxation of magnetization can be observed with maxima in the out-of-phase susceptibility in measurements with ac fields switching direction at frequencies between 1 and 1000 Hz under 0.1 T applied dc field, which indicates the existence of a slow relaxation behavior. A double generalized Debye model (sum of two Debye models) was used to analyze the relaxation processes.

The Cole-Cole plot approximates a semicircle (Figure 2.25 left), consistent with the generalized Debye model. It plots the relaxation time of complex [Nd$_2$(phsq)$_4$(tppo)$_2$(NO$_3$)$_2$] at different temperatures in the Figure 2.25 right. The plot of ln(τ) versus 1/T deviates from a straight line and exhibits a bend at high temperatures, indicating the presence of Raman, Orbach processes.

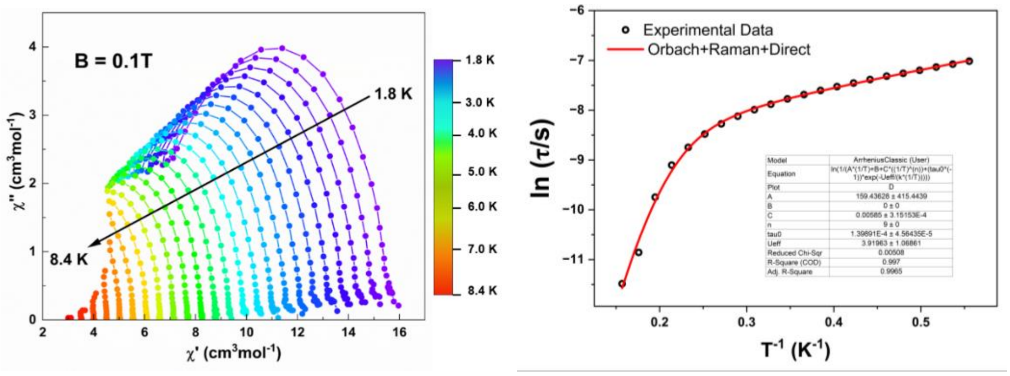

Figure 2.25. Cole-Cole plot at different temperatures (left). ln(τ) versus T^{-1} for $[Nd_2(phsq)_4(tppo)_2(NO_3)_2]$, solid red line represents the best-fit for magnetization relaxation (right).

Equation	$\tau^{-1} = AT + B + CT^n + {\tau_0}^{-1}\, exp^{-\frac{U_{eff}}{K_B T}}$
A	159.43628 ± 415.4439
B	0
C	0.00585 ± 3.15153E-4
n	9
$\boldsymbol{\tau_0}$	1.39891E-4 ± 4.56435E-5
U_{eff}	3.91963 ± 1.06861
Reduced Chi-Sqr	0.00508
R-Square (COD)	0.997
Adj. R-Square	0.9965

Table 2.4. Fitting parameters for the relaxation process of Figure 2.25 right

A plot of the natural logarithm of ln(τ) versus 1/T was shown in the figure 2.25 right. According to equation (1), a best fitting was obtained for $[Nd_2(phsq)_4(tppo)_2(NO_3)_2]$ yielding the parameters τ_0 = 1.40 x 10^{-4} s, U_{eff} = 3.92 K, C = 5.85 x 10^{-3} $s^{-1}K^{-n}$, n = 9.00 K and A = 159.44 $s^{-1}K^{-1}$ (Table 2.4), which means that the direct, Orbach and Raman relaxation process were taken into account.

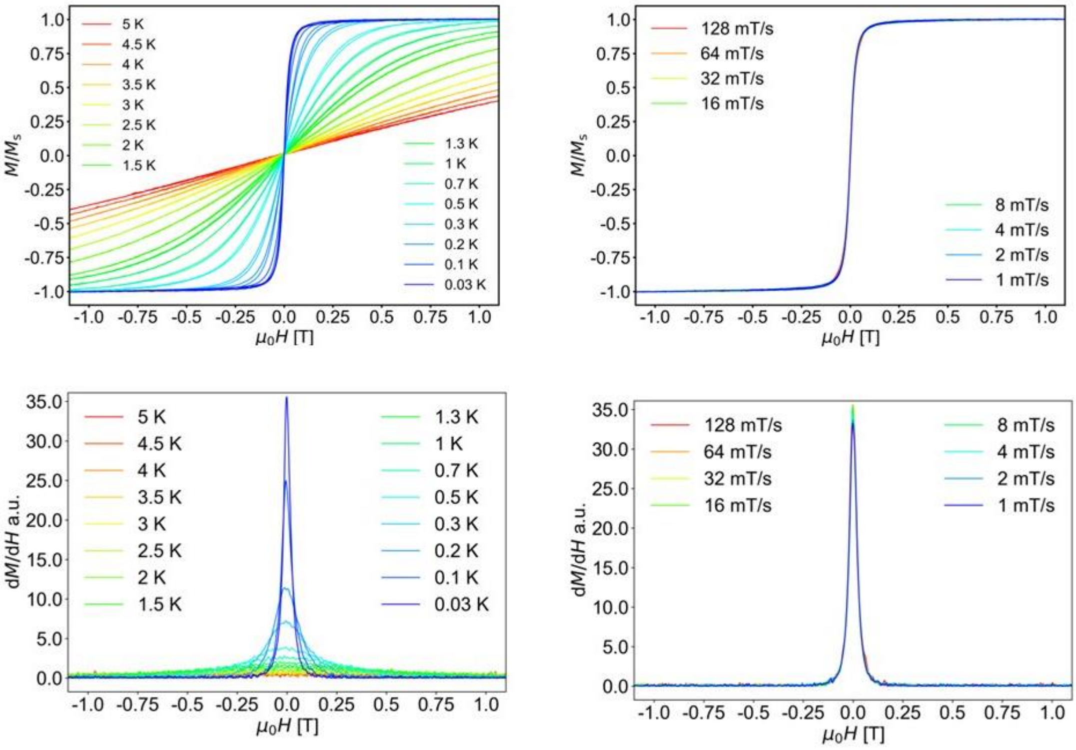

Figure 2.26. Micro-SQUID measurements performed on single crystals of [$Nd_2(phsq)_4(tppo)_2(NO_3)_2$]. Temperature dependence between 0.03 and 5 K (left) and sweep rate dependence between 1 and 128 mT/s (right), and the corresponding derivative curve (bottom).

Micro-SQUID measurements on single crystals of [$Nd_2(phsq)_4(tppo)_2(NO_3)_2$] were performed in order to investigate the magnetic behavior at very low temperatures (Figure 2.26). From the Micro-SQUID, we can see that its hysteresis loop is completely closed, with no obvious hysteresis behavior, implying that slow magnetic relaxation characteristic of single-molecule magnets is absent in this system.

2.4 Further Analysis of the Archetype Complexes [$Ln_2(phsq)_4(tppo)_2(NO_3)_2$]

Using the same experimental method, a series of isostructural radical compounds $[Ln_2(phsq)_4(NO_3)_2(tppo)_2]$ (Ln= Sm, Eu, Gd, Tb, Ho, Er, Tm, Yb, Lu) was obtained. The Dy-analogue has been discussed previously (section 2.2). In the following other Ln-analogues are shown. PXRD was performed to confirm the phase purity of the product, while ATR-IR was used to identify the characteristic vibrational modes of the attached ligands. A very good agreement was observed between the experimental PXRD pattern and the simulated pattern (Figure 2.27). The IR spectrum exhibits a characteristic C=O stretching band at 1670 cm^{-1}. Compared with the free phsq ligand (Figure 2.28), this peak disappears in some compounds, suggesting that the C=O group has reacted and coordinated with the lanthanide center. This also indicates the absence of unreacted phsq ligand in the sample.

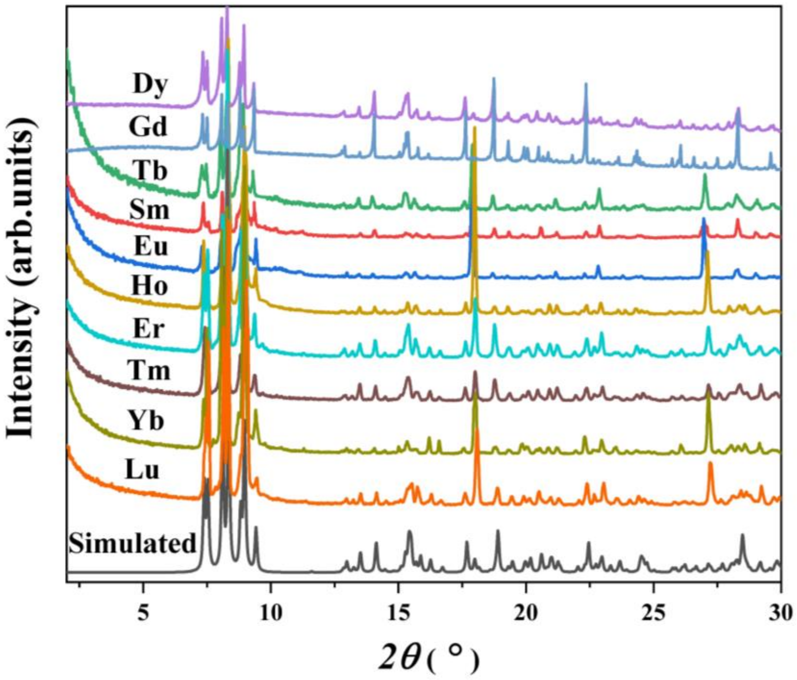

Figure 2.27. Powder-XRD of a series of $[Ln_2(phsq)_4(NO_3)_2(tppo)_2]$ compounds

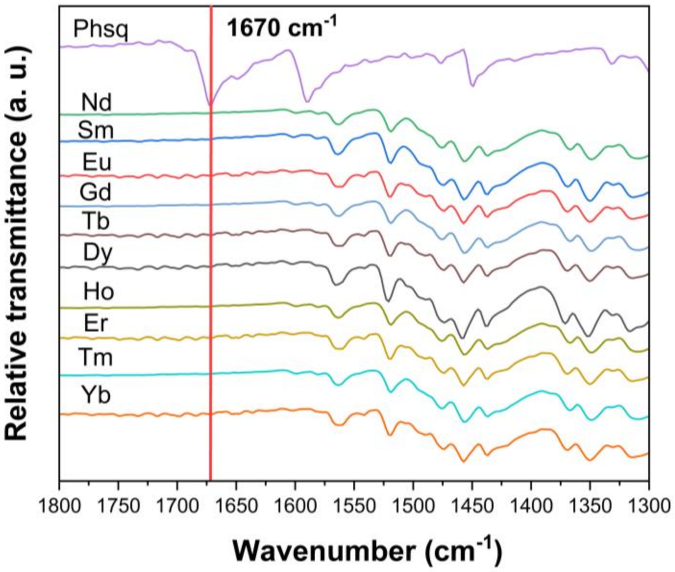

Figure 2.28. FT-IR spectra of a series of $[Ln_2(phsq)_4(tppo)_2(NO_3)_2]$ compounds

2.4.1 Magnetic properties of $[Gd_2(phsq)_4(tppo)_2(NO_3)_2]$

Direct current (dc) susceptibility measurements of $[Gd_2(phsq)_4(NO_3)_2(tppo)_2]$ were performed under a 0.1T and 1 T dc field in the range of 2−300 K. As shown in Figure 2.29, the $\chi_M T$ value at room temperature is 15.81 $cm^3\ K\ mol^{-1}$, which is close to the expected value of 15.76 $cm^3\ K\ mol^{-1}$ for two uncoupled Gd(III) ions ($4f^7$, $^8S_{7/2}$, L=0, J=7/2, g = 2, $\chi_M T_{calc}$=7.88 $cm^3\ K\ mol^{-1}$). This $\chi_M T$ value gradually decreases in the temperature range 300 – 14 K and then drops sharply and reached a minimum value of 8.14 $cm^3\ K\ mol^{-1}$ at 2 K. There is an antiferromagnetic interaction between Gd^{III} ions. The magnetic susceptibility of ac in this compound was also measured, but it did not exhibit slow relaxation behavior.

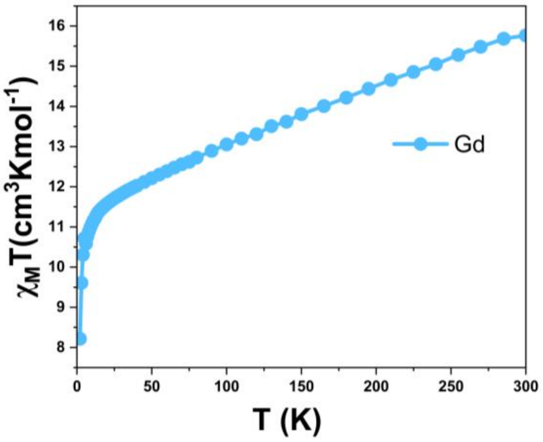

Figure 2.29. χ_MT vs T (left) plot of [$Gd_2(phsq)_4(tppo)_2(NO_3)_2$] (right) obtained at temperatures between 1.8 and 300 K with an applied magnetic dc field of 0.1 T.

2.4.2 Magnetic properties of [$Tb_2(phsq)_4(tppo)_2(NO_3)_2$]

Direct current (dc) magnetic susceptibility measurements were performed on microcrystalline samples of [$Tb_2(phsq)_4(tppo)_2(NO_3)_2$] in the range of 2−300 K under an applied magnetic field of 0.1 T. The room temperature χ_MT value of 23.83 cm^3 K mol^{-1} is close to the theoretical value of 23.62 cm^3 K mol^{-1} for two noninteracting free Tb^{III} ions (ground state $^7F_6$, S = 3, L = 3 and g = 3/2). The χ_MT product increases slightly until ~50 K, then it decreases sharply upon further cooling until ~2 K under an applied dc field 0.1 T, and reaching a value of 12.4 cm^3 K mol^{-1} at 2 K (Figure 2.30). The rapid decline of the χ_MT product upon lowering the temperature is mostly due to the depopulation of the crystal field m_J sub-levels and the intramolecular antiferromagnetic interactions between the two Tb^{III} ions.

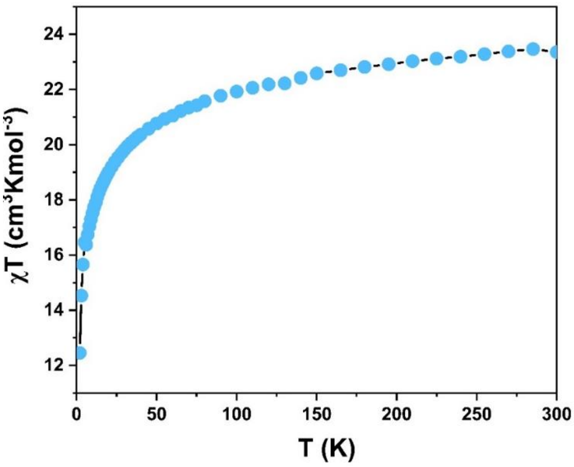

Figure 2.30. $\chi_M T$ vs T (left) plot of $[Tb_2(phsq)_4(tppo)_2(NO_3)_2]$ (right) obtained at temperatures between 1.8 and 300 K with an applied magnetic dc field of 0.1 T.

Alternating current (ac) susceptibility experiments were conducted at zero applied DC field in the temperature range 1.8 K to 4.0 K (Figure 2.31). Slow relaxation of magnetization can be observed with maxima in the out-of-phase susceptibility in measurements with ac fields switching direction at frequencies between 1 and 1500 Hz under 0.3 T applied dc field, which indicates the existence of a slow relaxation behavior to SMM. Due to its poor performance, it cannot achieve a proper fit.

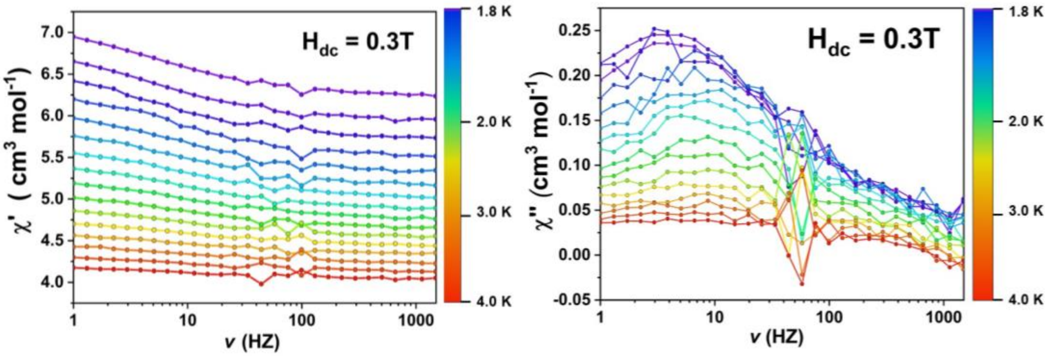

Figure 2.31. out-of-phase susceptibility at ac field frequencies between 1 and 1500 Hz and temperatures between 1.8 and 4 K of $[Tb_2(phsq)_4(tppo)_2(NO_3)_2]$.

2.5 Structure and Characterization of $[Dy_2(phsq)_4(tcypo)_2(NO_3)_2]$

2.5.1 Introduction

Previously, the tppo ligand was introduced as co-ligand in the semiquinone radical phsq$^{\cdot-}$ system. Its Dy-O$_{tppo}$ bond length is 2.26 Å, which is shorter than the average Dy-O bond length. Compared with the tppo ligand, the cyclohexane group in the tricyclohexanephosphine oxide (tcypo) ligand is less rigid than the benzene ring, which will also result in less steric hindrance and modifies the structure. Based on this, one novel addition to the Ln_2Rad_4 family of compounds $[Dy_2(phsq)_4(tcypo)_2(NO_3)_2]$ was successfully obtained.

2.5.2 Crystal structure of $[Dy_2(phsq)_4(tcypo)_2(NO_3)_2]$

In addition to the tppo ligand, the less rigid tricyclohexanephosphine oxide (tcypo) was selected to replace the axial tppo ligand leading to $[Dy_2(phsq)_4(tcypo)_2(NO_3)_2]$. The synthetic procedure was the same as that used for $[Dy_2(phsq)_4(tppo)_2(NO_3)_2]$. The compound crystallizes in space group P-1 which was confirmed with SCXRD. The overall structure and coordination environment of the Dy ions are basically the similar to those in $[Dy_2(phsq)_4(tppo)_2(NO_3)_2]$. It is worth noting that the distance between Dy ions in the dimer is 3.42 Å, which is slightly longer than that observed in $[Dy_2(phsq)_4(tppo)_2(NO_3)_2]$ structure. At the same time, the Dy-O distance in the axial direction is 2.24 Å (Figure 2.32), which is 0.02 Å shorter than $[Dy_2(phsq)_4(tppo)_2(NO_3)_2]$. This may be result from the fact that tcypo is less rigid than tppo, resulting in less steric hindrance for tcypo. Figure 2.33 shows the arrangement of the packing structure in the a-axis and b-axis directions.

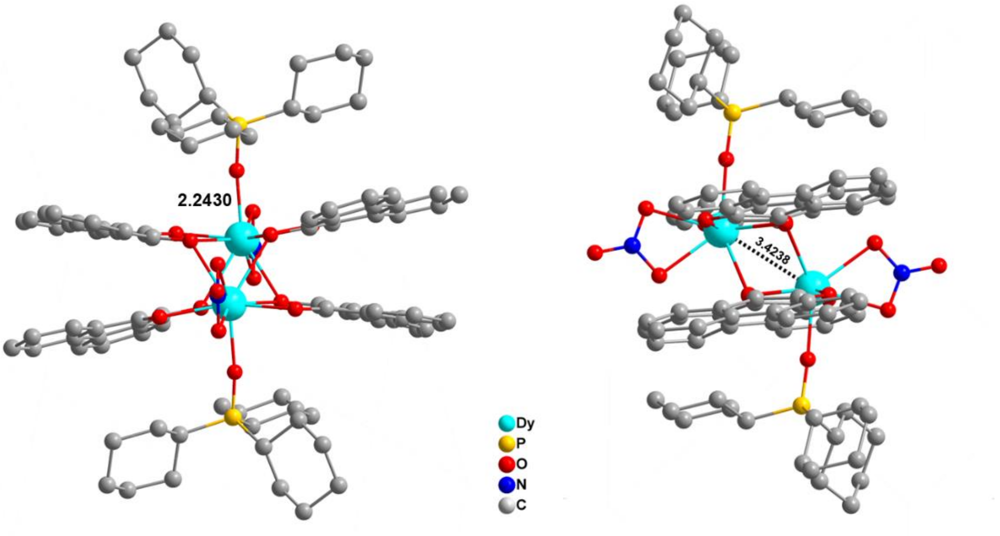

Figure 2.32. Side views and coordination environment of Dy atoms of the molecular structure of $[Dy_2(phsq)_4(NO_3)_2(tcypo)_2]$; organic H-atoms omitted for clarity.

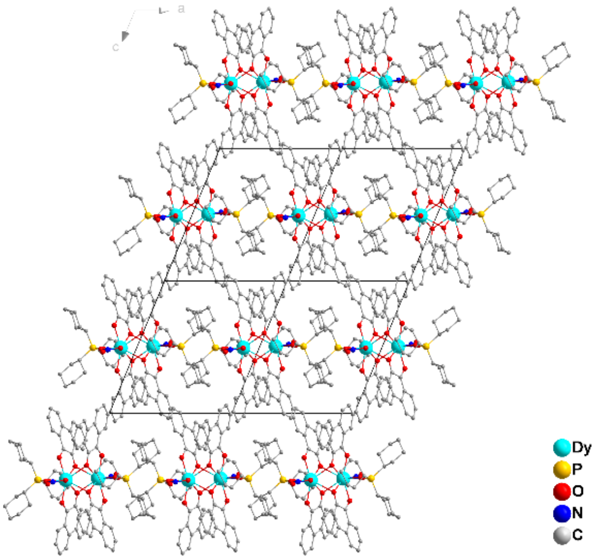

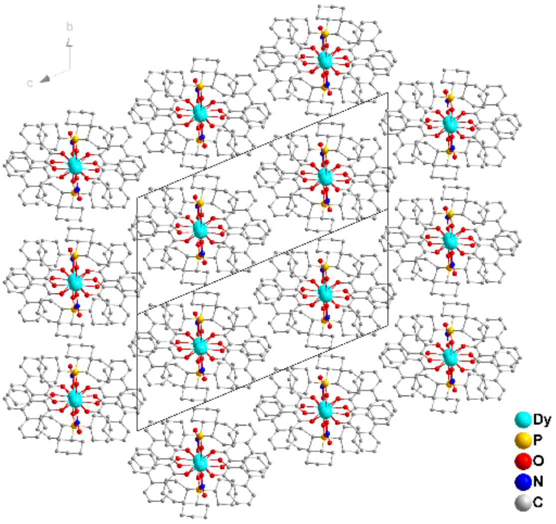

Figure 3.33. Packing views of the molecular structure of [Dy(phsq)$_4$(tcypo)$_2$(NO$_3$)$_2$]; organic H-atoms omitted for clarity.

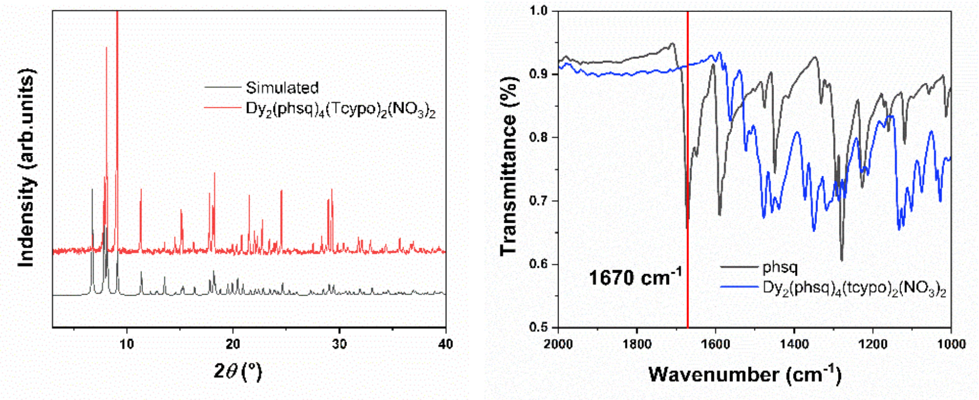

Figure 2.34. Powder-XRD (left) and ATR-IR spectra (right) of the compound [Dy(phsq)$_4$(tcypo)$_2$(NO$_3$)$_2$]

The PXRD results closely match the simulated pattern, validating the structural model (Figure 2.34 left). The infrared spectra show a characteristic C=O peak at 1670 cm^{-1}. In some compounds, the peak at 1670 cm^{-1}, compared to the characteristic peak of the ligand phsq, has disappeared, suggesting that the carbonyl has been hydrated. This also indicates that the sample is without unreacted phsq ligand precursor (Figure 2.34 right).

2.5.3 Magnetic properties of $[Dy_2(phsq)_4(tcypo)_2(NO_3)_2]$

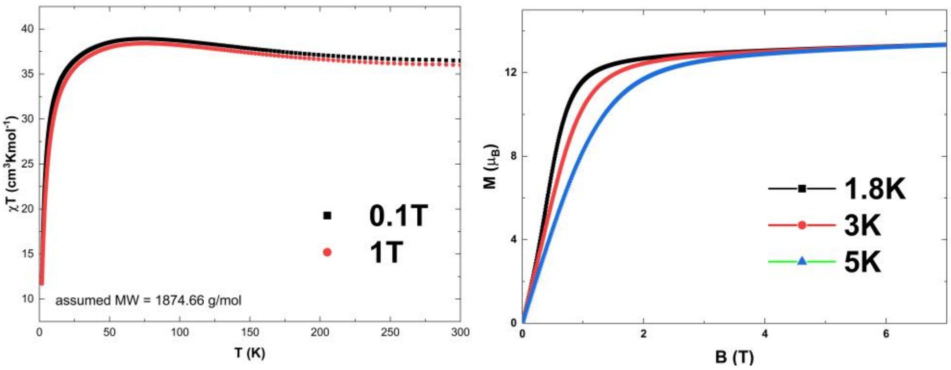

Figure 2.35. $\chi_M T$ vs. T plot of $[Dy_2(phsq)_4(tcypo)_2(NO_3)_2]$ measured between 1.8 and 300 K under applied dc magnetic fields of 0.1 T and 1 T (left). Magnetization (M) vs. applied field (H) plots at different temperatures (right).

Direct current (dc) magnetic susceptibility measurements were performed on microcrystalline samples of $[Dy_2(phsq)_4(tcypo)_2(NO_3)_2]$ in the range 2−300 K under applied magnetic fields of 0.1 T and 1 T. The room temperature $\chi_M T$ value of 27.43 cm^3 K mol^{-1} is close to the theoretical value of 28.34 cm^3 K mol^{-1} for two noninteracting free Dy^{III} ions (ground state $^6H_{15/2}$, S = 5/2, L = 5, and g = 4/3). The $\chi_M T$ product increases slightly until ~50 K, then it decreases sharply upon further cooling until ~2 K under an applied DC field 0.1 T and 1 T, and reaching a value of 13 cm^3 K mol^{-1} at 2 K for 1 T and 13.5 cm^3 K mol^{-1} at 2 K for 0.1 T (Figure 2.35 left) . The rapid decline of the $\chi_M T$ product upon lowering the temperature is likely due to the depopulation of the crystal field m_J sub-levels and intramolecular antiferromagnetic interactions between the two Dy^{III} ions.

In the reduced magnetization plots the curves do not overlap suggesting significant anisotropy and/or the presence and involvement of low-lying excited states. The magnetizations of $[Dy_2(phsq)_4(tcypo)_2(NO_3)_2]$ complex measured using applied magnetic fields at 1.8, 3 and 5 K reveal a rapid increase at low magnetic fields up to 2.5 T (Figure 2.35 right). At high magnetic fields, magnetization increases gradually and finally reaches ca. 12.15 μ_B at 7 T (Figure 2.35 right), which almost achieved the expected saturation value of 5 μ_B for an Ising-like Dy^{III}[183].

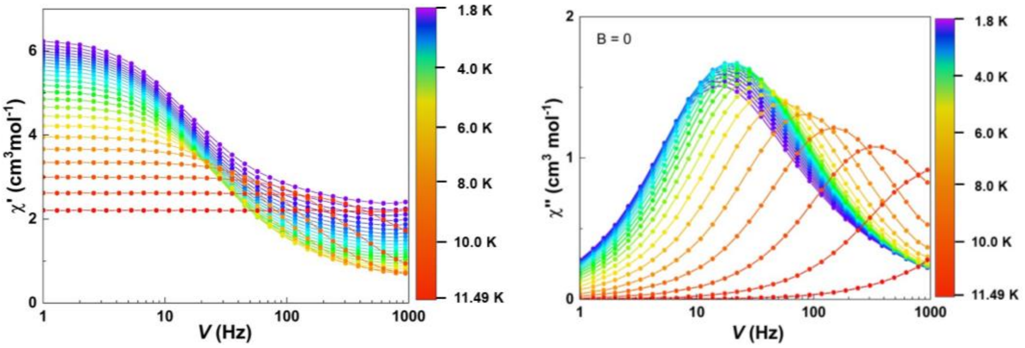

Figure 2.36. In- and out-of-phase susceptibility at ac field frequencies between 1 and 1000 Hz and temperatures between 1.8 and 11.5 K of $\mathrm{[Dy(phsq)_4(tcypo)_2(NO_3)_2]}$ (left and right, respectively).

Alternating Current (AC) susceptibility experiments were conducted at zero applied DC field in the temperature range 1.8 K to 11.49 K (Figure 2.36). Slow relaxation of magnetization can be observed with maxima in the out-of-phase susceptibility in measurements with ac fields switching direction at frequencies between 1 and 1000 Hz, which indicates the existence of a slow magnetization relaxation phenomenon to SMM. A double generalized Debye model (sum of two Debye models) was used to analyze the relaxation processes.

The Cole-Cole plot approximates a semicircle (Figure 2.37 left), consistent with the generalized Debye model. It plots the relaxation time of complex $\mathrm{[Dy_2(phsq)_4(tcypo)_2(NO_3)_2]}$ at different temperatures in the Figure 2.37 right. The plot of $\ln(\tau)$ versus 1/T deviates from a straight line and exhibits a bend at high temperatures, indicating the presence of Raman processes and Orbach process and a plateau at low temperature for QTM.

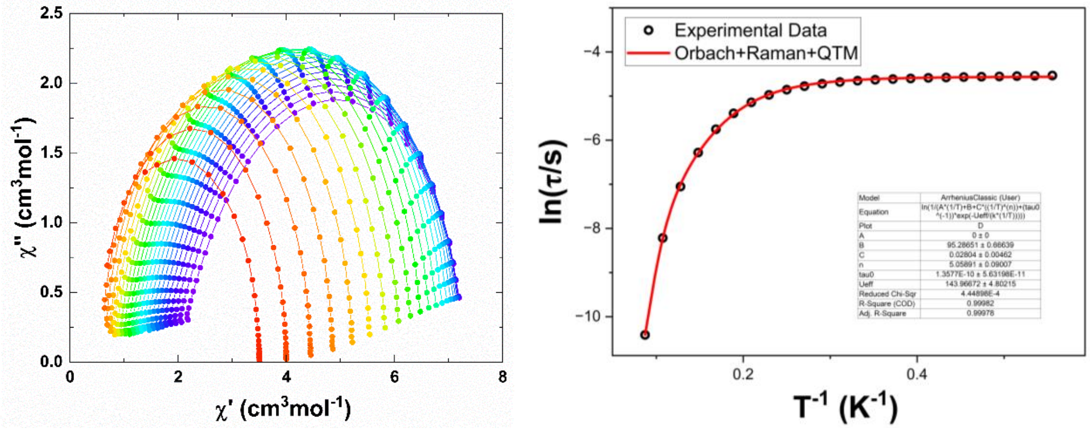

Figure 2.37. Cole-Cole plot at different temperatures (left). ln(τ) versus T^{-1} for $[Dy_2(phsq)_4(tcypo)_2(NO_3)_2]$, solid red line represents the best-fit for magnetization relaxation (right).

Equation	$\tau^{-1} = AT + B + CT^{n} + \tau_0^{-1}\, exp^{-\frac{U_{eff}}{K_B T}}$
A	0
B	95.28651 ± 0.66639
C	0.02804 ± 0.00462
n	5.05891 ± 0.09007
$\boldsymbol{\tau_0}$	1.3577E-10 ± 5.63198E-11
$\mathbf{U_{eff}}$	143.96672 ± 4.80215
Reduced Chi-Sqr	4.44898E-4
R-Square (COD)	0.99982
Adj. R-Square	0.99978

Table 2.5. Fitting parameters for the relaxation process of figure 2.37 right

A plot of ln(τ) versus 1/T was shown in the figure 2.37 right. According to equation (1), a best fitting was obtained for $[Dy_2(phsq)_4(tcypo)_2(NO_3)_2]$ yielding the parameters τ_0 = 1.36 x 10^{-10} s, U_{eff} = 143.97 K, C = 2.80 x 10^{-2} $s^{-1}K^{-n}$, n = 5.06 K and B = 95.29 s^{-1} (τ_{QTM} = 1.05 x 10^{-2} s) (Table 2.5), which means that the Orbach, Raman and QTM relaxation process were taken into account.

Therefore, compared to previous $[Dy_2(phsq)_4(tppo)_2(NO_3)_2]$ compounds, when tcypo replaces the tppo ligand (acquires the ligand), the equatorial crystal field energy of the Dy ion increases, prompting the occurrence of QTM under zero field conditions.

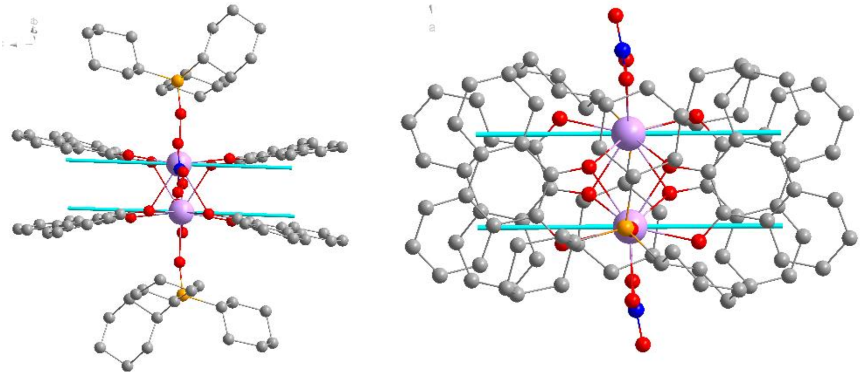

Figure 2.38. The side view (left) and top view (right) of anisotropy axes calculated using MAGELLAN on the crystal structure of $[Dy(phsq)_4(tcypo)_2(NO_3)_2]$

The anisotropy axes of $[Dy(phsq)_4(tcypo)_2(NO_3)_2]$ were calculated using MAGELLAN and are oriented the same way as in the $[Dy(phsq)_4(tcypo)_2(NO_3)_2]$ compound (Figure 2.38). The axes are essentially orthogonal to the Dy-Dy vector which, means the dipolar interaction will be antiferromagnetic.

2.6 Conclusion

This chapter describes the use of the $phsq^-$ radical and tppo ligands to synthesize 12 air-stable compounds, $[Dy(phsq)_4(tppo)_2(NO_3)_2]$ (Ln = Ce, Nd, Sm, Eu, Gd, Tb, Dy, Ho, Er, Tm, Yb, Lu). Among these, the compounds from Sm to Lu are isomorphous in the space group P-1 whereas Ce and Nd crystalize isomorphously in the space group Iba2. The structures of these two were described above. Tb, Dy, and Nd compounds exhibit slow relaxation behavior. It is worth noting that the distance between Dy ions in the dimer of $[Dy_2(phsq)_4(tppo)_2(NO_3)_2]$ is 3.42 Å, which is shorter than the 3.7 Å reported in the literature. In particular, the Dy compound exhibits single-molecule magnetic behavior in the absence of an external magnetic field, showing a maximum AC magnetic susceptibility at 14.07 K (1000 Hz). Its QTM is effectively suppressed at zero field, as confirmed by Zeeman plots obtained using CASSCF caculations. The QTM is also observed at zero field upon Y doping which deletes the dipolar coupling between the two metal centers.

In addition the exchange of tppo with the less rigid analogue tcypo group was successful, using the same synthetic method, leading to the isolation of $[Dy_2(phsq)_4(tcypo)_2(NO_3)_2]$. The single-crystal structure and magnetic properties were analyzed and reveal slow relaxation of magnetization. In AC magnetic susceptibility measurements maxima are observed up to 11.49 K (1000 Hz benchmark) in the absence of an external magnetic dc field.

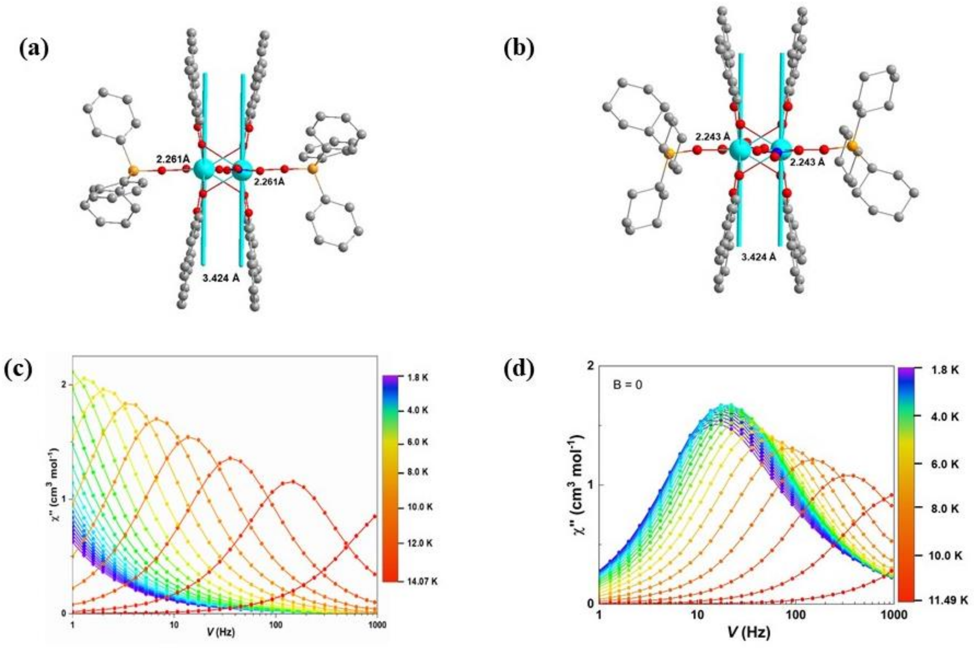

Figure 2.39. Anisotropy axes of $Dy(phsq)_4(tppo)_2(NO_3)_2$ **(a)** and $Dy(phsq)_4(tcypo)_2(NO_3)_2$ **(b);** AC susceptibility curve of $Dy(phsq)_4(tppo)_2(NO_3)_2$ **(c)** and $Dy(phsq)_4(tcypo)_2(NO_3)_2$ **(d).**

Notably, in both Dy complexes, the anisotropy axis is oriented perpendicular to the Dy---Dy direction as well as the tppo/tcypo ligands (figures 2.39a, b). Thus, the coordination of the tppo or tcypo ligands can be regarded as being along the equatorial ligand direction. The Dy-O bond distance in the equatorial coordination direction for $[Dy_2(phsq)_4(tppo)_2(NO_3)_2]$ and $[Dy_2(phsq)_4(tcypo)_2(NO_3)_2]$ are 2.261 Å and 2.243 Å, respectively. This implies that the equatorial crystal field binding energy of $[Dy_2(phsq)_4(tcypo)_2(NO_3)_2]$ is greater than that of $[Dy_2(phsq)_4(tppo)_2(NO_3)_2]$, indicating that anisotropy of $[Dy_2(phsq)_4(tppo)_2(NO_3)_2]$ is stronger, which in turn implies superior magnetic properties. This is further confirmed by magnetic data (Figures 2.39c, d). A second explanation as to why the tppo-analogue outperforms its tcypo counterpart is the flexibility of the tcypo ligands which can result in additional phonon modes which in turn can couple to the Dy spins and lead to enhanced Raman relaxation.

Chapter 3. Single-Molecule Magnet Behavior in Lanthanide–Pyrene-4,5-Semiquinate Radical Complexes

3.1 Introduction

In the lanthanide-semiquinone radical compound described earlier in this thesis, which is based on 9,10-phenanthrenequinone, the anisotropy axes align along the radical ligand. To enhance the π–π interactions between the radical ligands, we selected pyrene-4,5-dione as the new ligand. This modification also enables us to further investigate how increased aromatic overlap and stronger π–π interactions influence the properties and magnetic behavior of lanthanide–radical complexes. This is likely to shorten the spacing between lanthanide metals while also increasing the radical-metal interactions along the direction of the free-body ligands, thereby enhancing the crystal field energy and potentially improving its magnetic properties. With this motivation in mind, pyrene-4,5-dione was synthesized [194] (Figure 3.1). Using pyrene-4,5-dione (pyq) as a source of radical ligands and simultaneously introducing tppo or tcypo, six air-stable compounds: [$Ln_2(pysq)_4(tppo)_2(NO_3)_2$] (Ln = Nd, Gd, Dy, Ho, Er) and [$Dy_2(pysq)_4(tppo)_2(NO_3)_2$] were obtained successfully.

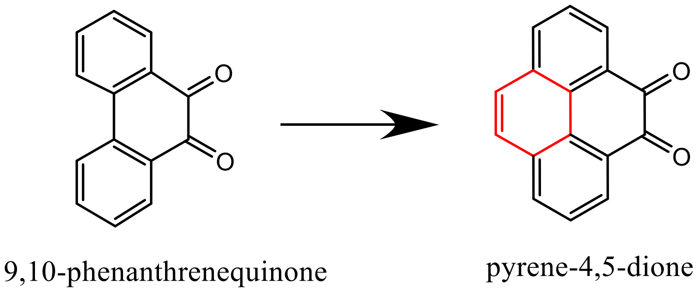

Figure 3.1. Reaction scheme for the synthesis of the Pyrene- 4,5 -dione ligand

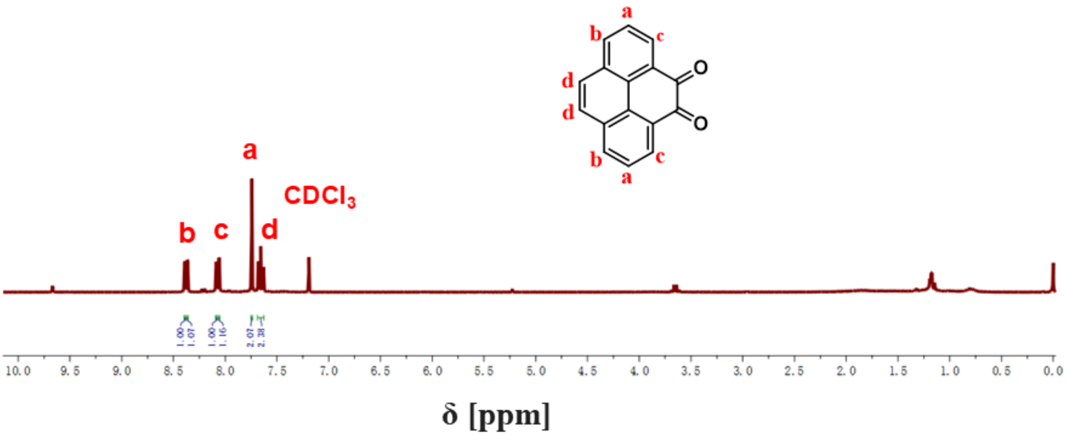

Figure 3.2. NMR of pyrene-4,5-dione

3.2 Structure and Characterization of [$Dy_2(pysq)_4(tppo)_2(NO_3)_2$]

3.2.1 Crystal Structure of [$Dy_2(pysq)_4(tppo)_2(NO_3)_2$]

The synthetic procedure and reaction conditions for [$Dy_2(pysq)_4(tppo)_2(NO_3)_2$] are the same as those employed for [$Dy_2(phsq)_4(tppo)_2(NO_3)_2$]. Single crystal X-ray diffraction analyses of all compounds show that they are isomorphous, crystallizing in space group P-1. The centrosymmetric molecule consists of a dinuclear lanthanide unit bridged by four pysq$^-$ ligands (Figure 3.3). The lanthanides are nine coordinate in a capped square-antiprismatic O9 geometry. Among them, 6 oxygen atoms come from four radical pysq$^-$ ligands, another oxygen atom comes from the tppo ligand, and the other two oxygen atoms come from the nitrate ion. It can be seen from Figure 3.3 that the four radical ligands tightly bind the two Dy ions together, wrapping them together so that the Dy-Dy distance is only 3.418 Å, which is much shorter than the 3.700 Å reported in the literature. The left of Figure 3.3 shows the coordination environment of Dy, where the axial Dy-O bond length is 2.26 Å, which is shorter than most Dy-O bond lengths. This is due to the introduction of the tppo ligand to produce such a short axial Dy-O bond length.

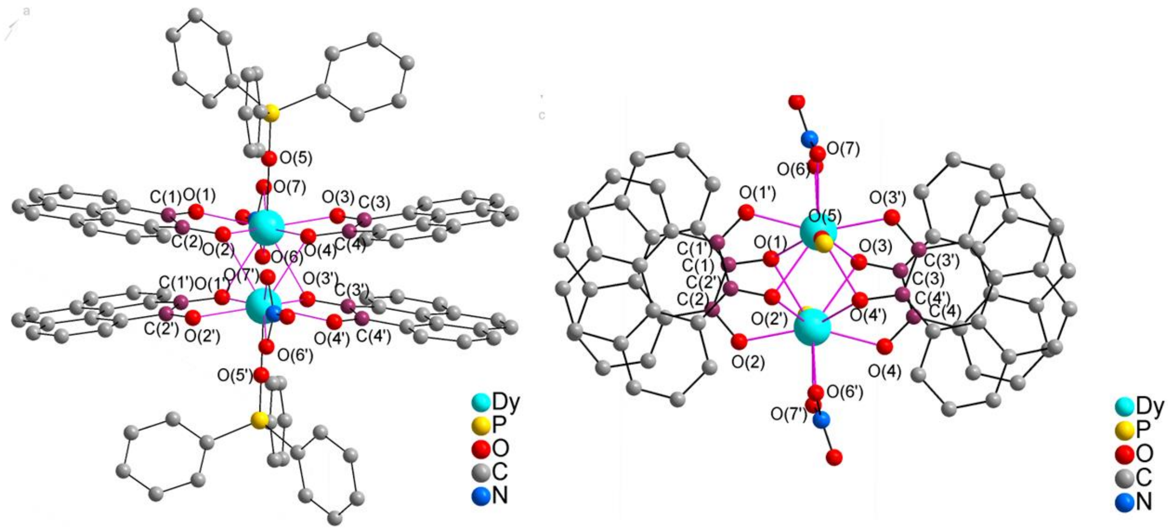

Figure 3.3. Two views of the molecular structure of [Dy_2(pysq)$_4$ (tppo)$_2$(NO_3)$_2$]; organic H-atoms omitted for clarity.

Based on the packing arrangement shown in Figure 3.4, we observed that each unit cell contains four dimer units located at the corners, all arranged in a consistent pattern (indicated by the pink lines in the right panel of Figure 3.4). Additionally, a dimer occupies the center of the unit cell, and the arrangement of the central dimers in adjacent unit cells is also consistent (shown by the green lines in the right panel of Figure 3.4). In addition, there is a 61.11° angle between the dimer at the corner of the unit cell and the dimer at the center of the unit cell. Powder XRD measurements were performed on the [Dy_2(pysq)$_4$(tppo)$_2$(NO_3)$_2$] sample, and the experimental PXRD pattern shows good agreement with the simulated data (Figure 3.5).

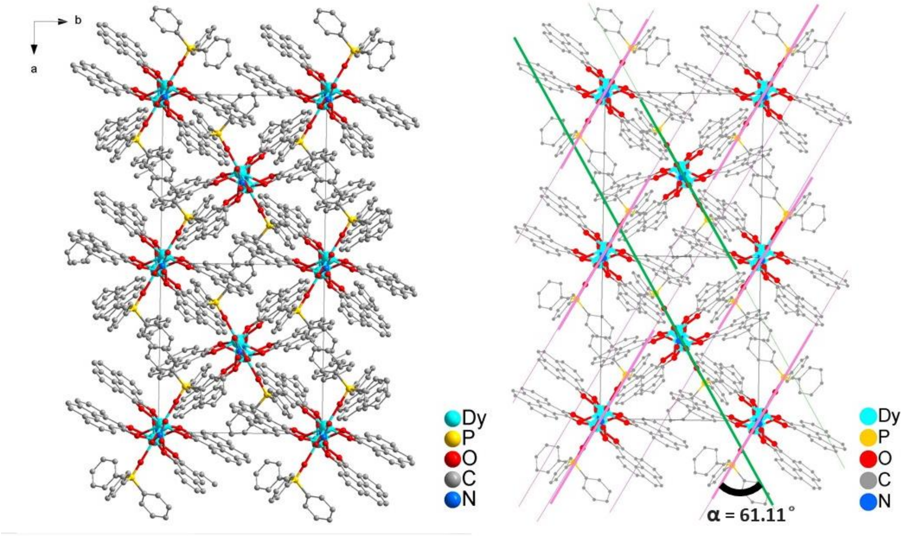

Figure 3.4. Packing structure of [Dy_2(pysq)$_4$(tppo)$_2$(NO_3)$_2$]; hydrogen atoms of the organic ligands are omitted for clarity

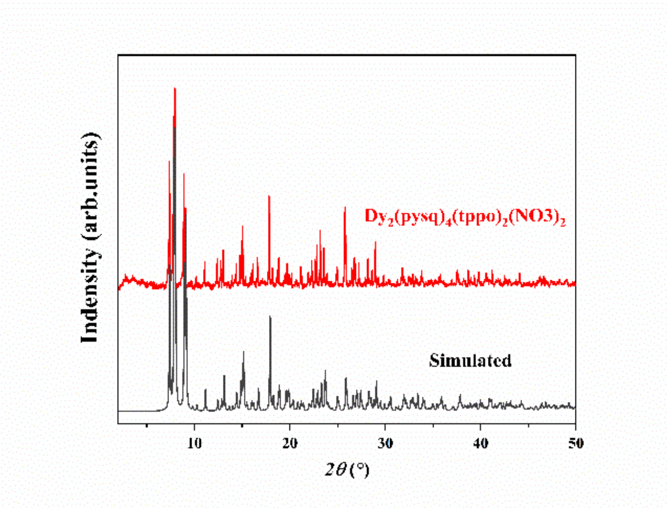

Figure 3.5. Powder-XRD of [Dy_2(pysq)$_4$(tppo)$_2$(NO_3)$_2$] compared with the simulated patter

3.2.2 Magnetic properties of $[Dy_2(pysq)_4(tppo)_2(NO_3)_2]$

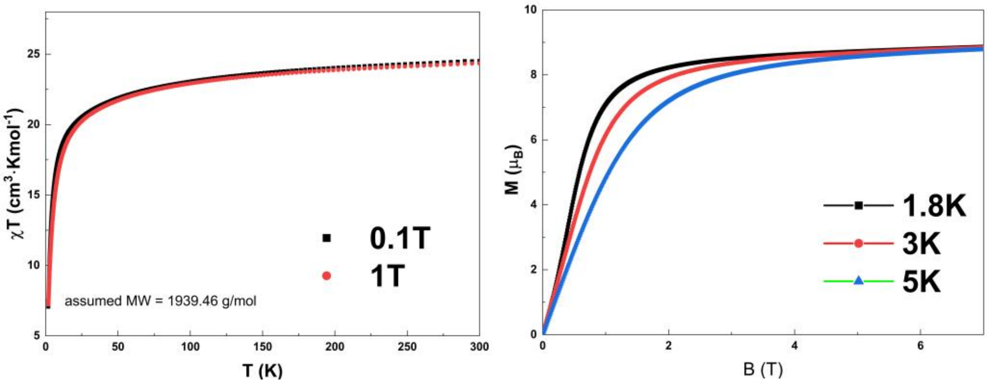

Figure 3.6. $\chi_M T$ vs T plot of $[Dy_2(pysq)_4(tppo)_2(NO_3)_2]$ measured between 1.8 and 300 K under applied dc magnetic fields of 0.1 T and 1 T (left). Magnetization (M) vs. applied field (H) plots at different temperatures (right).

Direct current (dc) magnetic susceptibility measurements were performed on microcrystalline samples of $[Dy_2(pysq)_4(tppo)_2(NO_3)_2]$ in the range 2−300 K under applied magnetic fields of 0.1 T and 1 T. The room temperature $\chi_M T$ value of 26.13 cm^3 K mol^{-1} is close to the theoretical value of 28.34 cm^3 K mol^{-1} for two noninteracting free Dy^{III} ions (ground state $^6H_{15/2}$, S = 5/2, L = 5, and g = 4/3). The $\chi_M T$ product remains almost constant until ~100 K, then it decreases smoothly upon further cooling until ~30 K, and more sharply at the end, reaching a value of 5.6 cm^3 K mol^{-1} at 2 K for 0.1 T, and reaching a value of 6 cm^3 K mol^{-1} at 2 K for 1 T. The rapid decline of the $\chi_M T$ product upon lowering the temperature is likely due to the depopulation of the crystal field m_J sub-levels and intramolecular antiferromagnetic interactions between the two Dy^{III} ions[193].

In the reduced magnetization plots the curves do not overlap suggesting significant anisotropy and/or the presence and involvement of low-lying excited states. The magnetizations of $[Dy_2(pysq)_4(tppo)_2(NO_3)_2]$ complex measured using applied magnetic fields at 1.8, 3 and 5 K reveal a rapid increase at low magnetic fields (Fig 3.6 right). At high magnetic fields, magnetization increases gradually and finally reaches ca. 9.12 μ_B at 7 T (Fig 3.6b), which almost meets the saturation value of 5 μ_B for an Ising-like Dy^{III}[183].

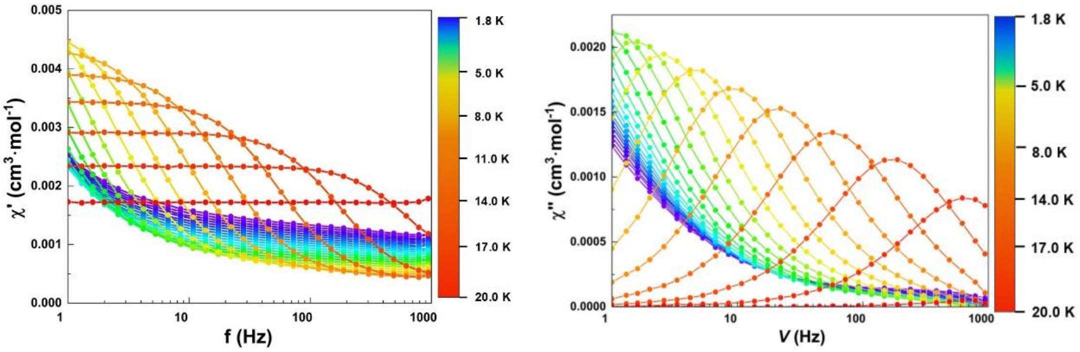

Figure 3.7. In- and out-of-phase susceptibility at ac field frequencies between 1 and 1000 Hz and temperatures between 1.8 and 20 K of $[Dy_2(pysq)_4(tppo)_2(NO_3)_2]$ (left and right, respectively).

AC susceptibility experiments were conducted at zero applied DC field in the temperature range 1.8 K to 20.0 K (Figure 3.7). Slow relaxation of magnetization can be observed with maxima in the out-of-phase susceptibility in measurements with ac fields switching direction at frequencies between 1 and 1000 Hz, which indicates the existence of a slow magnetization relaxation phenomenon to SMM. A double generalized Debye model (sum of two Debye models) was used to analyze the relaxation processes.

The Cole-Cole plot approximates a semicircle (Figure 3.8 left), consistent with the generalized Debye model. It plots the relaxation time of complex $[Dy_2(pysq)_4(tppo)_2(NO_3)_2]$ at different temperatures in the Figure 2.10 right. The plot of $\ln(\tau)$ versus 1/T deviates from a straight line and exhibits a bend at high temperatures, indicating the presence of Raman and Orbach processes.

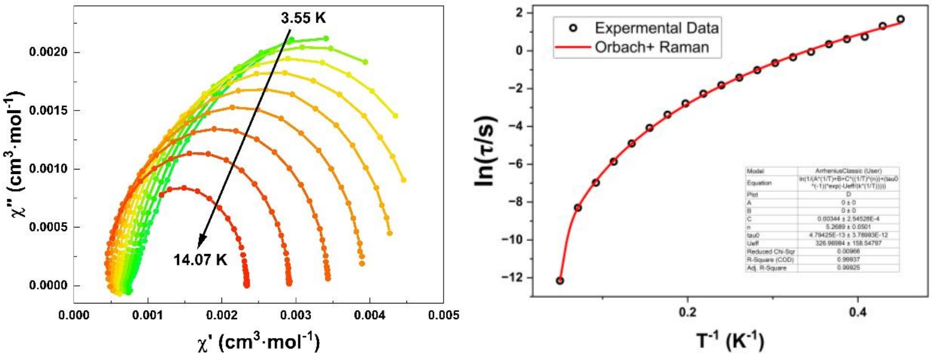

Figure 3.8. Cole-Cole plot at different temperatures (left). ln(τ) versus T^{-1} for [$Dy_2(pysq)_4(tppo)_2(NO_3)_2$], solid red line represents the best-fit for magnetization relaxation (right).

Equation	$\tau^{-1} = AT + B + CT^n + {\tau_0}^{-1} \, exp^{-\frac{U_{eff}}{K_B T}}$
A	0
B	0
C	0.00344 ± 2.54528E-4
n	5.2689 ± 0.0501
τ_0	4.79425E-13 ± 3.78993E-12
U_{eff}	326.96984 ± 158.54797
Reduced Chi-Sqr	0.00966
R-Square (COD)	0.99937
Adj. R-Square	0.99925

Table 3.1. Fitting parameters for the relaxation process of figure 3.8 right

A plot of the natural logarithm of ln(τ) versus 1/T was shown in the figure 3.13 right. According to equation (1) of Chapter 2, a best fitting was obtained for [$Dy_2(pysq)_4(tppo)_2(NO_3)_2$] yielding the parameters τ_0 = 4.79 x 10^{-13} s, U_{eff} = 326.97 K, C = 3.44 x 10^{-3} s^{-1} K^{-n}, n = 5.27 (Table 3.1), which means that the orbach and Raman relaxation process were taken into account. Compared to previous [$Dy_2(phsq)_4(tppo)_2(NO_3)_2$] compounds, the magnetic properties of [$Dy_2(pysq)_4(tppo)_2(NO_3)_2$] were significantly improved by replacing the $phsq^-$ radical ligand with the $pysq^-$ ligand.

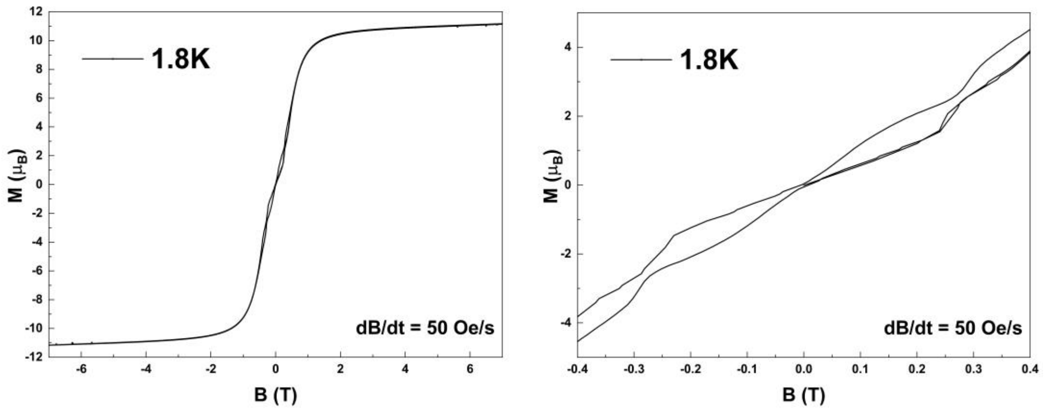

Figure 3.9. Hysteresis loop (left) and narrow hysteresis shown by [Dy_2(pysq)$_4$(tppo)$_2$(NO_3)$_2$] at 1.8 K between -0.4 T and 0.4 T indicating SMM behavior at this temperature.

We measured the hysteresis loop at 1.8 k and found that the center of the plots a hysteresis opens at temperatures 1.8 k (Figure 3.9).

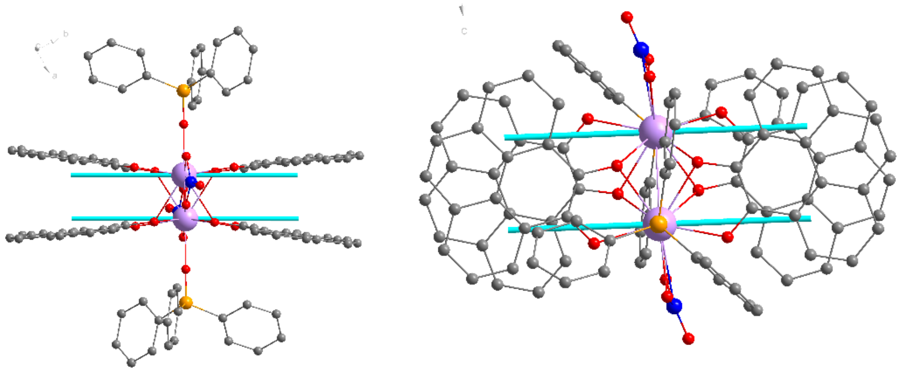

Figure 3-10. The side view (left) and top view (right) of anisotropy axes calculated using MAGELLAN on the crystal structure of [Dy_2(pysq)$_4$(tppo)$_2$(NO_3)$_2$]

The anisotropy axes of [Dy(pysq)$_4$(tppo)$_2$(NO_3)$_2$] were calculated using MAGELLAN and are oriented the same way as in the [Dy(phsq)$_4$(tppo)$_2$(NO_3)$_2$] compound (Figure 3.10). The axes are essentially orthogonal to the Dy-Dy vector which means the dipolar interaction will be antiferromagnetic.

3.2.3 Magnetic Properties of Y-doped $[Dy_xY_{(1-x)}(pysq)_4(tppo)_2(NO_3)_2]$

To further confirm that quantum tunneling in the Dy dimer is caused by the internal magnetic field between the dipoles, we replaced majority of the Dy with diamagnetic Y^{III}, transforming the Dy^{III} in the dimer into a single ion paramagnetic Dy structure (that is, directly eliminating the internal antiferromagnetic magnetic field of the dimer). Therefore, we successfully obtained the Y-doped compound $[Dy_xY_{(1-x)}(phsq)_4(tppo)_2(NO_3)_2]$ by using 90% diamagnetic Y^{III} and 10% paramagnetic Dy^{III} as raw materials.

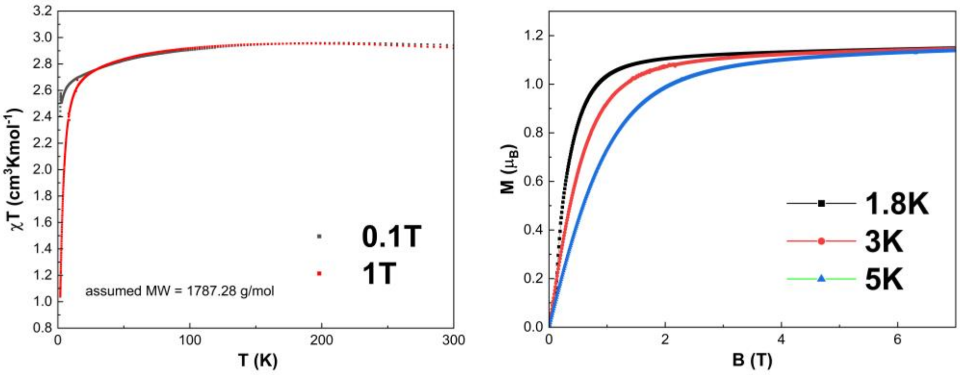

Figure 3.11. $\chi_M T$ vs T (left) and magnetization plot of $[Dy_xY_{(1-x)}(phsq)_4(tppo)_2(NO_3)_2]$ measured between 1.8 and 300 K under applied dc magnetic fields of 0.1 T and 1 T (left). Magnetization (M) vs. applied field plots at different temperatures (right).

Direct current (dc) magnetic susceptibility measurements were performed on microcrystalline samples of $[Dy_xY_{(1-x)}(phsq)_4(tppo)_2(NO_3)_2]$ in the range 2−300 K under applied magnetic fields of 0.1 T and 1 T. The $\chi_M T$ product decreases smoothly upon further cooling until ~30 K (Figure 3.11). There is an antiferromagnetic interaction between Dy^{III}.

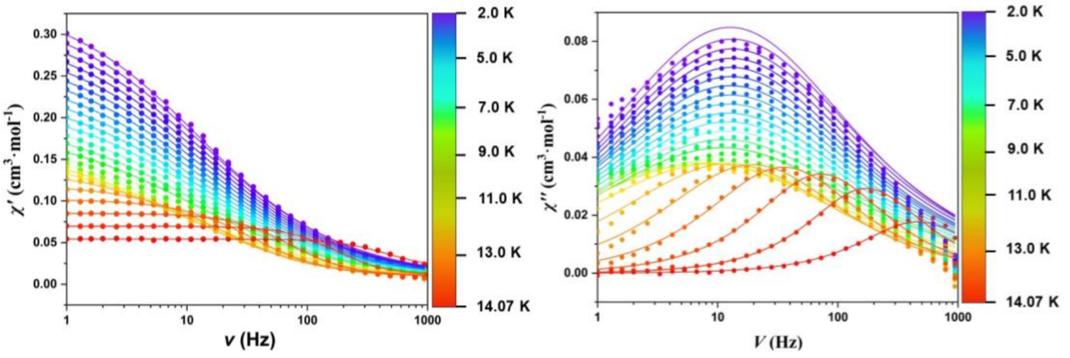

Figure 3.12. In- and out-of-phase susceptibility at ac field frequencies between 1 and 1000 Hz and temperatures between 1.8 and 14.1 K of [$Dy_XY_{(1-x)}(phsq)_4(tppo)_2(NO_3)_2$] (left and right, respectively).

AC susceptibility experiments were conducted at zero applied dc field in the temperature range 1.8 K to 14.07 K (Figure 3.12). Slow relaxation of magnetization can be observed with maxima in the out-of-phase susceptibility in measurements with ac fields switching direction at frequencies between 1 and 1000 Hz, which indicates the existence of slow relaxation behavior.

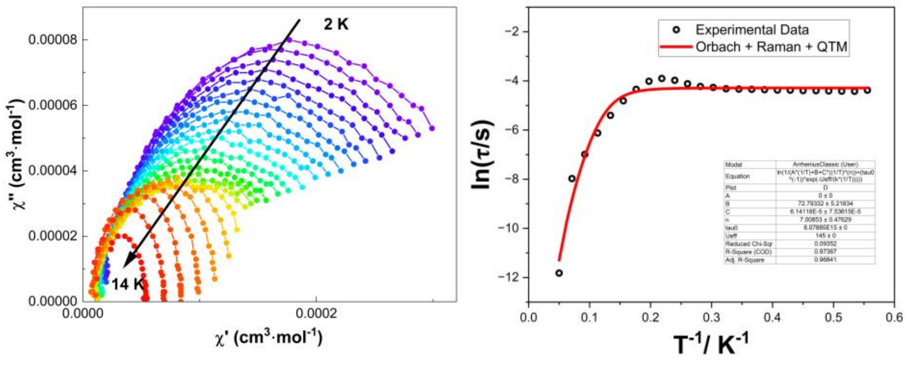

Model	ArrheniusClassic (User)
Equation	ln(1/(A*(1/T)+B+C*((1/T)^(n))+(tau0^(-1))*exp(-Ueff/(k*(1/T)))))
Plot	D
A	0 ± 0
B	72.79332 ± 5.21834
C	6.14118E-5 ± 7.53615E-5
n	7.00853 ± 0.47629
tau0	8.07886E15 ± 0
Ueff	145 ± 0
Reduced Chi-Sqr	0.09352
R-Square (COD)	0.97367
Adj. R-Square	0.96841

Figure 3.13. Cole-Cole plot at different temperatures (left). ln(τ) versus T^{-1} for [$Dy_XY_{(1-x)}(phsq)_4(tppo)_2(NO_3)_2$], solid red line represents the best-fit for magnetization relaxation (right).

Equation	$\tau^{-1} = AT + B + CT^{n} + {\tau_0}^{-1}\, exp^{-\frac{U_{eff}}{K_B T}}$
A	0
B	72.79332 ± 5.21834
C	6.14118E-5 ± 7.53615E-5
n	7.00853 ± 0.47629
τ_0	8.07885E15 ± 0
U_{eff}	145
Reduced Chi-Sqr	0.09352
R-Square (COD)	0.97367
Adj. R-Square	0.96841

Table 3.2. Fitting parameters for the relaxation process of figure 3.13 right

A plot of the natural logarithm of ln(τ) versus 1/T was shown in the figure 3.13 right. According to equation (1) of Chapter 2, a best fitting was obtained for [$Dy_XY_{(1-x)}(phsq)_4(tppo)_2(NO_3)_2$] yielding the parameters τ_0 = 8.08 x 10^{-15} s, U_{eff} = 145.00 K, C = 6.14 x 10^{-5} s^{-1} K^{-n}, n = 7.00 and B = 72.79 s^{-1} ($\tau_{QTM} =$ 1.37 x 10^{-2} s) (Table 3.2) which means that the direct, Orbach and QTM relaxation process were taken into account. We were able to observe a platform at low temperatures, which clearly indicates that the QTM process is occurring. Therefore, when most of Dy is replaced by diamagnetic Y, the relaxation process of QTM under zero field is observed again.

3.3 Further Analysis of the Archetype Complexes [$Ln_2(pysq)_4(tppo)_2(NO_3)_2$]

3.3.1 Bulk purity (PXRD) and ATR-IR spectroscopic analysis

Using the same experimental procedure, a series of isostructural pysq compounds, [$Ln_2(pysq)_4(tppo)_2(NO_3)_2$] (Ln = Nd, Gd, Ho, Er), were synthesized. Powder-XRD measurements confirmed the phase purity, showing excellent agreement between the experimental and simulated patterns, while ATR-IR spectroscopy was used to verify the coordination of the ligands (Figure 3.14). The IR spectrum (Figure 3.14) shows that the characteristic C=O stretching peak appears at 1665 cm⁻¹, slightly red-shifted from 1670 cm⁻¹ observed in the free phsq ligand, indicating coordination of the ligand to the metal center. This is mainly due to the conjugation effect of the pyrene ring system, the absorption peak of C=O stretching vibration may be slightly red-shifted (reduced wave number)[195]. The peaks of some compounds at 1665 cm^{-1} disappeared compared with the characteristic peaks of the ligand pysq, indicating that the ligand has opened the bond at C=O and coordinated with the lanthanide atom. It also indicates that the sample does not contain pysq ligands. Here, the magnetic behaviors of $[Ln_2(pysq)_4(NO_3)_2(tppo)_2]$ (Ln=Nd, Gd, Ho, Er) were explored.

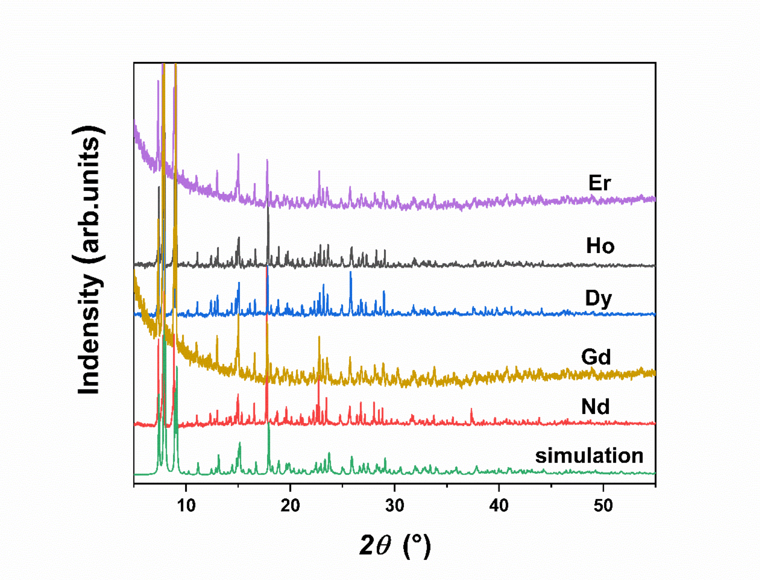

Figure 3.14. Powder-XRD patterns of a series of $[Ln_2(pysq)_4(NO_3)_2(tppo)_2]$ compounds compared with the simulated patterns.

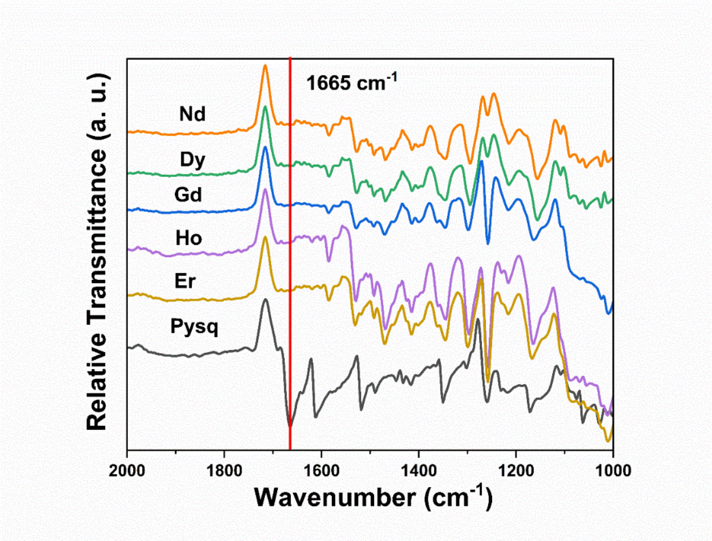

Figure 3.15. ATR-IR spectra of a series of [$Ln_2(pysq)_4(tppo)_2(NO_3)_2$] compounds compared with the free ligand.

3.3.2 Magnetic properties of [$Gd_2(pysq)_4(tppo)_2(NO_3)_2$]

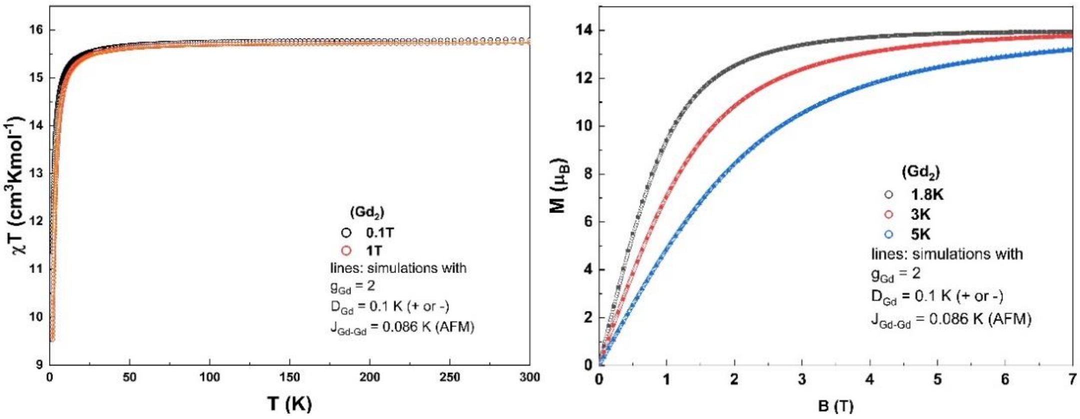

Figure 3.16. χ_MT vs T (left) plot of [$Gd_2(pysq)_4(NO_3)_2(tppo)_2$] (right) obtained at temperatures between 1.8 and 300 K with an applied magnetic dc field of 0.1 T and 1 T. Plots of M vs. H (right) at different temperatures.

Direct current (dc) susceptibility measurements of [$Gd_2(pysq)_4(NO_3)_2(tppo)_2$] were performed under a 0.1T and 1 T dc field in the range of 2−300 K. As shown in Figure 3.16 left, the χ_MT value at room temperature is 15.82 cm^3 K mol^{-1}, which is close to the expected value of 15.76 cm^3 K mol^{-1} for two uncoupled Gd(III) ions (4f^7, $^8S_{7/2}$, L=0, J=7/2, g = 2, $\chi_M T_{calc}$=7.88 cm^3 K mol^{-1}). This χ_MT value remains relatively stable in the temperature range 300 – 25 K and then drops sharply and reached a minimum value of 9.5 cm^3 K mol^{-1} at 2 K. There is an antiferromagnetic interaction between Gd^{III} ions. Moreover, after scaling the magnetization data to g = 2, the fitting was performed, and the results showed that the antiferromagnetic coupling is weak and the single ion anisotropy is small. For the Gd^{III} ion, both seem to have reasonable values, and have corresponding dipolar coupling, with an exchange coupling value J_{Gd-Gd}=0.086 K.

The field dependence of magnetization of complex [$Gd_2(pysq)_4(tppo)_2(NO_3)_2$] was evaluated at different temperatures 1.8, 3 and 5 K in the magnetic field range of 0 – 7 T (Fig 3.16 right). The sharp increase of magnetization at low field at low temperatures reveals a significant energy difference between the ground and excited states. Additionally, as the external field is increased, the magnetization value increases and reaches saturation at 13.98 μ_B for complex [$Gd_2(pysq)_4(NO_3)_2(tppo)_2$] at 7 T.

3.3.3 Magnetic properties of [$Ho_2(pysq)_4(tppo)_2(NO_3)_2$]

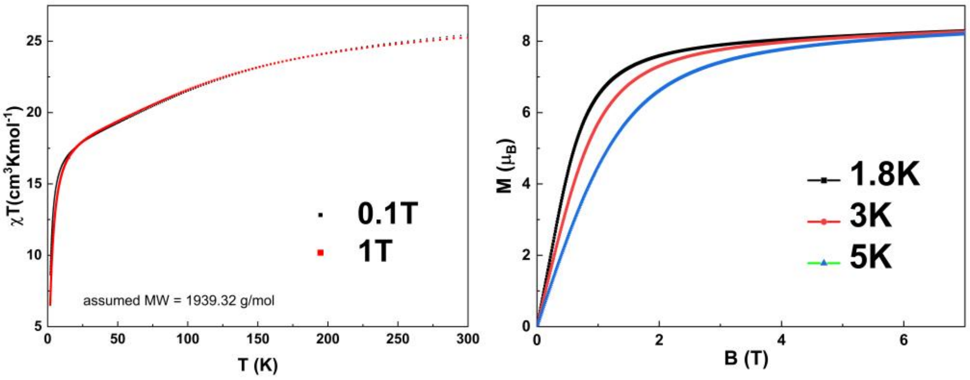

Figure 3.17. χ_MT vs T plot of [$Ho_2(pysq)_4(NO_3)_2(tppo)_2$] measured between 1.8 and

300 K under applied dc magnetic fields of 0.1 T and 1 T (left), and magnetization (M) vs. applied field (B) plots at different temperatures (right).

Direct current (dc) susceptibility measurements of $[Ho_2(pysq)_4(NO_3)_2(tppo)_2]$ were performed under a 0.1T and 1 T dc field in the range 2−300 K. As shown in Figure 3.17 left, the $\chi_M T$ value at room temperature is 25.32 cm^3 K mol^{-1}, which is close to the expected value of 28.14 cm^3 K mol^{-1} for two uncoupled Ho^{III} ions ($4f^7$, $^8S_{7/2}$, L=0, J=7/2, g = 2, $\chi_M T_{calc}$=14.07 cm^3 K mol^{-1}). This $\chi_M T$ value remains relatively stable in the temperature range of 300 – 125 K, and reduce gradually between 125 K to 25 K, then drops sharply and reached a minimum value of 6.2 cm^3 K mol^{-1} at 2 K. There is a ferromagnetic interaction between Ho^{III} ions. The trend of the $\chi_M T$ value at low temperatures can be attributed to the thermal death of low-level excited states or the existence of weak ferromagnetic interactions between Ho^{III} ions in the complex[193].

The field dependence of magnetization of complex $[Ho_2(pysq)_4(tppo)_2(NO_3)_2]$ was evaluated at different temperatures 1.8, 3 and 5 K in the magnetic field range of 0 – 7 T (Figure 3.17 right). The sharp increase of magnetization at low field at low temperatures reveals a significant energy difference between the ground and excited states. Additionally, as the external field is increased, the magnetization value increases and reaches saturation at 8.23 μ_B for complex $[Ho_2(pysq)_4(tppo)_2(NO_3)_2]$ at 7 T, which is consistent with the expected 9 μ_B for two Ho^{III} ions with a well-defined J = 8 ground doublet.

3.3.4 Magnetic properties of $[Er_2(pysq)_4(tppo)_2(NO_3)_2]$

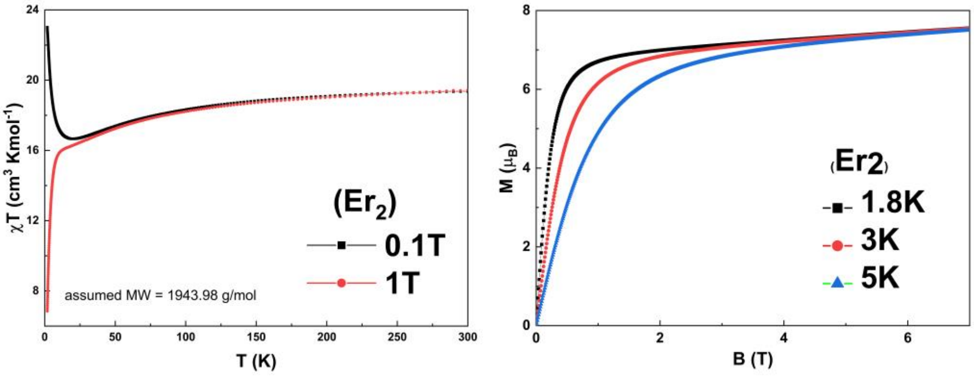

Figure 3.18. $\chi_M T$ vs T (left) plot of $[Er_2(pysq)_4(NO_3)_2(tppo)_2]$ (right) obtained at temperatures between 1.8 and 300 K with an applied magnetic dc field of 0.1 T and 1 T. Plots of M vs. H (right) at different temperatures.

Direct current (dc) susceptibility measurements of $[Er_2(pysq)_4(NO_3)_2(tppo)_2]$ were performed under a 0.1T and 1 T dc field in the range of 2−300 K. As shown in Figure 3.18 left, the $\chi_M T$ value at room temperature is 18.42 $cm^3\ K\ mol^{-1}$, which is close to the expected value of 18.34 $cm^3\ K\ mol^{-1}$ for two uncoupled Er^{III} ions ($4f^{11}$, $^4I_{15/2}$, $\chi_M T_{calc}$=11.48 $cm^3\ K\ mol^{-1}$). This $\chi_M T$ value reduce gradually in the temperature range of 300 – 25 K and then drops sharply and reached a minimum value of 6.2 $cm^3\ K\ mol^{-1}$ at 2 K under applied field 1 T. There is a slight upward trend at 3.5K. Moreover, this $\chi_M T$ value reduce gradually in the temperature range of 300 – 12 K and then increase sharply and reached a maximum value of 23.05 $cm^3\ K\ mol^{-1}$ at 2 K under applied field 0.1 T. there is an ferromagnetic interaction between Er^{III} ions.

The field dependence of magnetization of complex $[Er\ _2(pysq)_4(NO_3)_2(tppo)_2]$ was evaluated at different temperatures 1.8, 3 and 5 K in the magnetic field range of 0 – 7 T (Fig 3.18 right). The sharp increase of magnetization at low field at low temperatures reveals a significant energy difference between the ground and excited states. Additionally, as the external field is increased, the magnetization value increases and reaches saturation at 8.23 μB for complex [$Er_2(pysq)_4(NO_3)_2(tppo)_2$] at 7 T, which is consistent with the expected 9 μB for two Er^{III} ions with a well-defined J = 15/2 ground doublet.

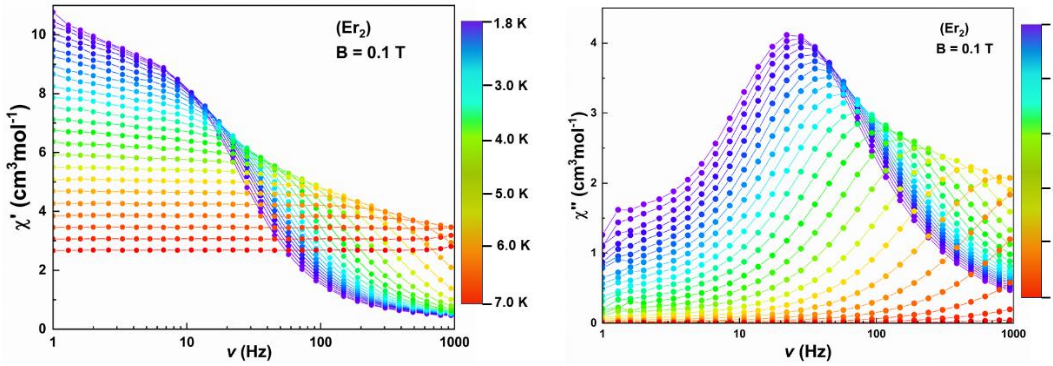

Figure 3.19. In-phase (top) and out-of-phase (bottom) ac susceptibility vs frequency measured on [$Er_2(pysq)_4(NO_3)_2(tppo)_2$] at temperatures between 1.8 K and 7.0 K with an applied dc field of 0.28 T. Lines are the best fit to the Debye model accounting for two sets of maxima.

AC susceptibility experiments were conducted at zero applied DC field in the temperature range 1.8 K to 7.0 K (Figure 3.19 left). Slow relaxation of magnetization can be observed with maxima in the out-of-phase susceptibility in measurements with ac fields switching direction at frequencies between 1 and 1000 Hz, which indicates the existence of a slow magnetization relaxation phenomenon to SMM. A double generalized Debye model (sum of two Debye models) was used to analyze the relaxation processes.

The Cole-Cole plot approximates a semicircle (Figure 3.19 right), consistent with the generalized Debye model. It plots the relaxation time of complex [$Er_2(pysq)_4(tppo)_2(NO_3)_2$] at different temperatures in the Figure 3.20 right. The plot of ln(τ) versus 1/T deviates from a straight line and exhibits a bend at high temperatures, indicating the presence of Raman, Orbach.

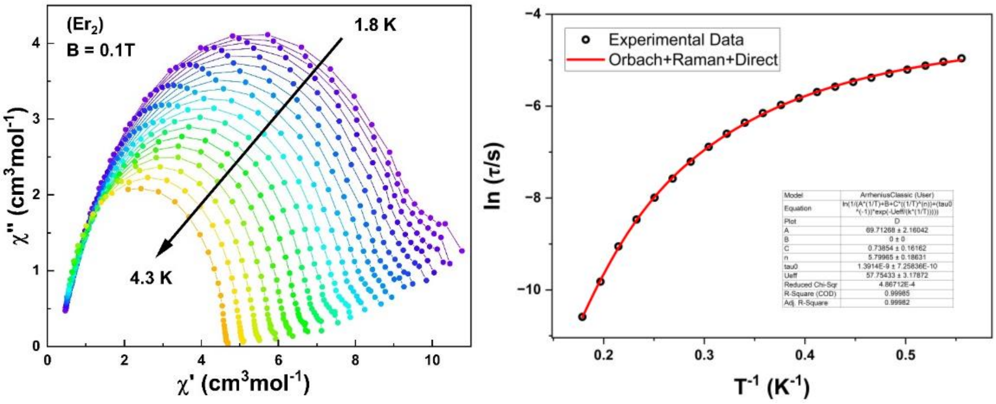

Model	ArrheniusClassic (User)
Equation	ln(1/(A*(1/T)+B+C*((1/T)^(n))+(tau0^(-1))*exp(-Ueff/(k*(1/T)))))
Plot	D
A	69.71268 ± 2.16042
B	0 ± 0
C	0.73854 ± 0.16162
n	5.79965 ± 0.18631
tau0	1.3914E-9 ± 7.25836E-10
Ueff	57.75433 ± 3.17872
Reduced Chi-Sqr	4.86712E-4
R-Square (COD)	0.99985
Adj. R-Square	0.99982

Figure 3.20. Cole-Cole plot at different temperatures (left). ln(τ) versus T^{-1} for [Er$_2$(pysq)$_4$(tppo)$_2$(NO$_3$)$_2$], solid red line represents the best-fit for magnetization relaxation (right).

Equation	$\tau^{-1} = AT + B + CT^{n} + \tau_0{}^{-1}\, exp^{-\frac{U_{eff}}{K_B T}}$
A	69.71268 ± 2.16042
B	0
C	0.73854 ± 0.16162
n	5.79965 ± 0.18631
τ_0	1.3914E-9 ± 7.25836E-10
U$_{eff}$	57.75433 ± 3.17872
Reduced Chi-Sqr	4.86712E-4
R-Square (COD)	0.99985
Adj. R-Square	0.99982

Table 3.3. Fitting parameters for the relaxation process of figure 3.20 right

A plot of the natural logarithm of ln(τ) versus 1/T was shown in the figure 3.20 right. According to equation (1) of Chapter 2, a best fitting was obtained for [Er$_2$(phsq)$_4$(tppo)$_2$(NO$_3$)$_2$] yielding the parameters τ_0 = 1.39 x 10^{-9} s, U$_{eff}$ = 57.75 K, C = 0.74 s^{-1}K^{-n}, n = 5.80 and A = 69.71 s^{-1} K^{-1} (Table 3.3), which means that the direct, Orbach and Raman relaxation process were taken into account.

3.3.5 The characterization of $[Nd_2(pysq)_4(tppo)_2(NO_3)_2]$

Direct current (dc) magnetic susceptibility measurements were performed on microcrystalline samples of $[Nd_2(pysq)_4(tppo)_2(NO_3)_2]$ in the range 2−300 K under applied magnetic field of 0.1 T and 1 T. The room temperature χ_MT value of 2.62 cm^3 K mol^{-1} is close to the theoretical value of 3.28 cm^3 K mol^{-1} for two noninteracting free Nd^{III} ions (ground state S = 3/2, *L* = 6, $^4I_{9/2}$, *J* = 9/2, *g* = 8/11, $\chi_M T_{Cacl}$ =1.64 cm^3 K mol^{-1}). The χ_MT product reduce gradually until ~4.2 K, then it increases sharply until 2 K, reaching a value of 2.57cm^3 K mol^{-1} at 2 K under an applied 0.1 T DC field. In addition, the χ_MT product increases gradually until ~2.7 K, then it reduces sharply until 2 K under an applied 1 T dc field, reaching a value of 1.82 cm^3 K mol^{-1} at 2 K. With decreasing temperature, the χ_MT value decreases gradually, probably due to the progressive depopulation of the excited Stark sublevels, which means the depopulation of the crystal field m_J sub-levels and the intramolecular ferromagnetic interactions between the two Nd^{III} ions.

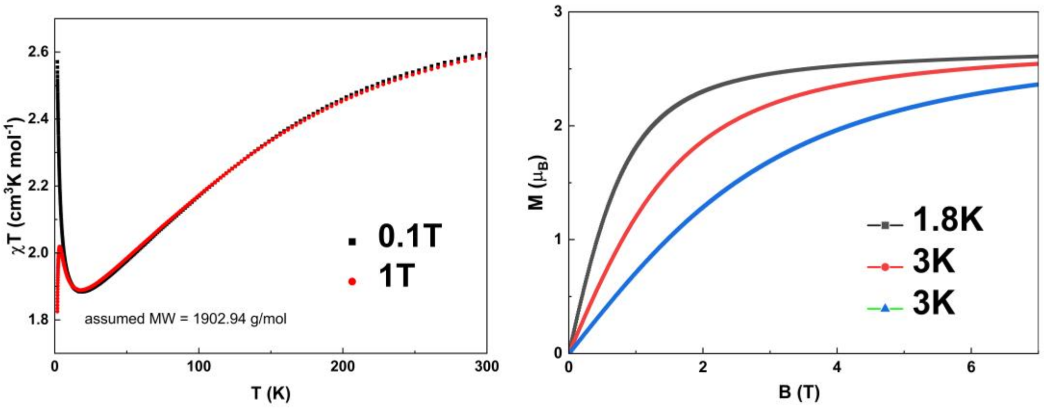

Figure 3.21. χ_MT vs T (left) plot of $[Nd_2(pysq)_4(NO_3)_2(tppo)_2]$ measured between 1.8 and 300 K under applied dc magnetic fields of 0.1 T and 1 T (left), and magnetization (M) vs. applied field (H) plots at different temperatures (right).

The field dependence of magnetization for [Nd_2(pysq)$_4$(tppo)$_2$(NO_3)$_2$] was measured in the 0-7 T field range and at different temperatures. The magnetizations of [Nd_2(pysq)$_4$(TPPO)$_2$(NO_3)$_2$] complex measured against applied magnetic fields at 1.8, 3 and 5 K reveal a rapid increase at low magnetic fields (Figure 3.21 right). The maximum value of 2.61 μ_B was observed at 2 K and 7 T, lower than the theoretical saturated value of 3 μ_B (S = 7/2) anticipated for two independent Nd(III) ions, which can be attributed to the ligand-field-induced splitting of the Stark level as well as the magnetic anisotropy.

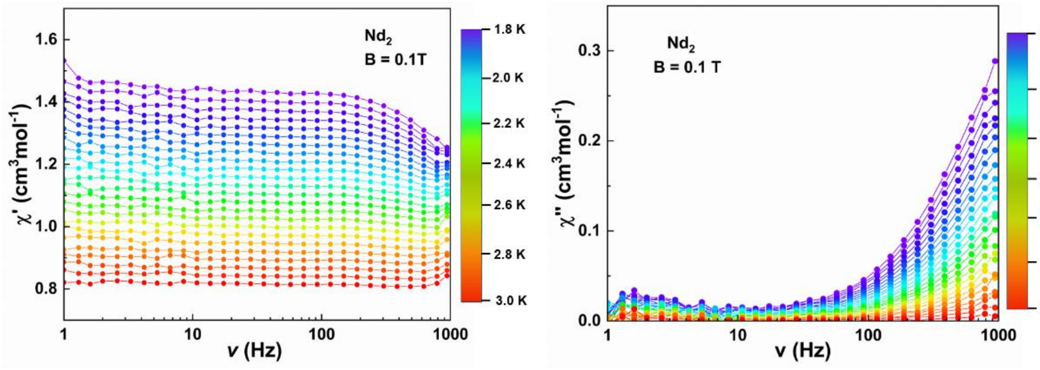

Figure 3.22. In-phase (top) and out-of-phase (bottom) ac susceptibility vs frequency measured on [Nd_2(pysq)$_4$(NO_3)$_2$(tppo)$_2$] at temperatures between 1.8 K and 3.0 K with an applied dc field of 0.28 T. Lines are the best fit to the Debye model accounting for two sets of maxima.

Alternating Current (ac) susceptibility experiments were conducted at zero applied DC field in the temperature range 1.8 K to 3.0 K (Figure 3.22 left). Slow relaxation of magnetization can be observed with maxima in the out-of-phase susceptibility in measurements with ac fields switching direction at frequencies between 1 and 1000 Hz under 0.1 T applied dc field, which indicates the existence of a slow magnetization relaxation phenomenon to SMM. A double generalized Debye model (sum of two Debye models) was used to analyze the relaxation processes.

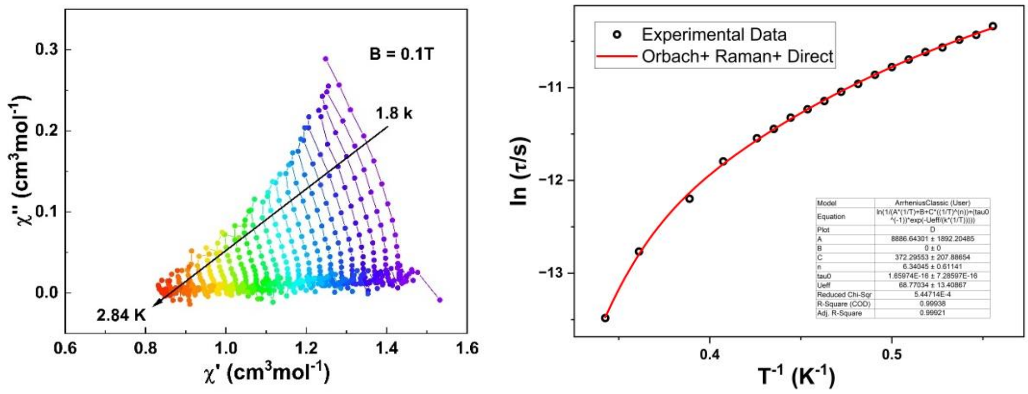

Model	ArrheniusClassic (User)
Equation	ln(1/(A*(1/T)+B+C*((1/T)^(n))+(tau0 ^(-1))*exp(-Ueff/(k*(1/T)))))
Plot	D
A	8886.64301 ± 1892.20485
B	0 ± 0
C	372.29553 ± 207.88654
n	6.34045 ± 0.61141
tau0	1.65974E-16 ± 7.28597E-16
Ueff	68.77034 ± 13.40867
Reduced Chi-Sqr	5.44714E-4
R-Square (COD)	0.99938
Adj. R-Square	0.99921

Figure 3.23. Cole-Cole plot at different temperatures (left). ln(τ) versus T^{-1} for [$Nd_2(pysq)_4(tppo)_2(NO_3)_2$], solid red line represents the best-fit for magnetization relaxation (right).

Equation	$\tau^{-1} = AT + B + CT^n + \tau_0{}^{-1}\, exp^{-\frac{U_{eff}}{K_BT}}$
A	8886.64301 ± 1892.20485
B	0
C	372.29553 ± 207.88654
n	6.34045 ± 0.61141
τ_0	1.65974E-16 ± 7.28597E-16
U$_{eff}$	68.77034 ± 13.40867
Reduced Chi-Sqr	5.44714E-4
R-Square (COD)	0.99938
Adj. R-Square	0.99921

Table 3.4. Fitting parameters for the relaxation process of figure 3.23 right

A plot of the natural logarithm of ln(τ) versus 1/T was shown in the figure 3.23 right. According to equation (1) of Chapter 2, a best fitting was obtained for [$Nd_2(pysq)_4(tppo)_2(NO_3)_2$] yielding the parameters τ_0 = 1.66 x 10^{-16} s, U$_{eff}$ = 68.77 K, C = 372.30 s^{-1}K^{-n}, n = 6.34 and A = 8886.64 s^{-1} K^{-1} (Table 3.4), which means that the direct, orbach and raman relaxation process were taken into account.

3.4 Structure and Characterization of $[Dy_2(pysq)_4(tcypo)_2(NO_3)_2]$

3.4.1 Crystal structure of $[Dy_2(pysq)_4(tcypo)_2(NO_3)_2]$

In addition to the tppo ligand, the more flexible trihexylphosphine oxide (tcypo) was employed to replace the axial tppo ligand and, leading to the successful synthesis of $[Dy_2(pysq)_4(NO_3)_2(tcypo)_2]$, using the same method as for $[Dy_2(pysq)_4(NO_3)_2(tppo)_2]$. Single crystal X-ray diffraction analyses analysis shows that the compound crystallizes in the triclinic space group $P\overline{1}$. The main structure of this compound and the coordination environment of Dy ions are basically the same as $[Dy_2(pysq)_4(NO_3)_2(tppo)_2]$ structure. The distance between Dy in the dimer is 3.4203 Å (Figure 3.24), which is the same with $[Dy_2(phsq)_4(NO_3)_2(tppo)_2]$ structure. At the same time, the Dy-O bond distance in the axial direction is 2.220 Å, which is 0.04 Å shorter than $[Dy_2(phsq)_4(NO_3)_2(tppo)_2]$ axial distance. This is likely due to the fact that tcypo is less rigid than tppo, resulting in less steric hindrance for tcypo. The PXRD data show a perfect match between the experimental data and the structural simulation data (Figure 3.25).

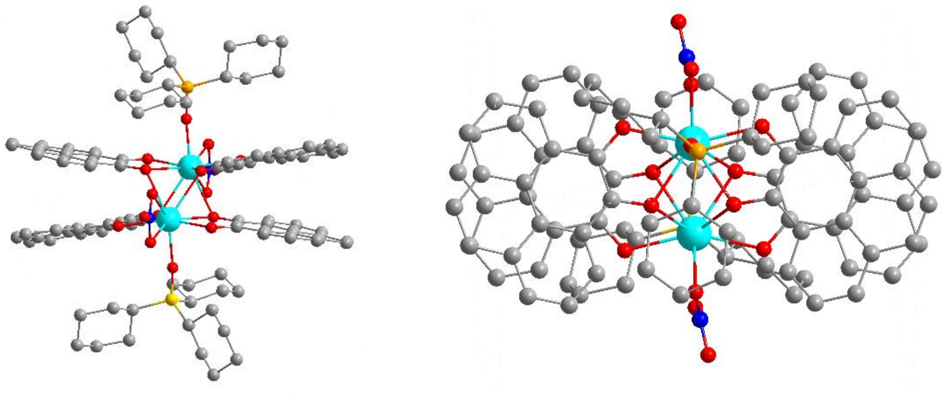

Figure 3.24. Two views of the molecular structure of $[Dy_2(pysq)_4(tcypo)_2(NO_3)_2]$; organic H-atoms omitted for clarity.

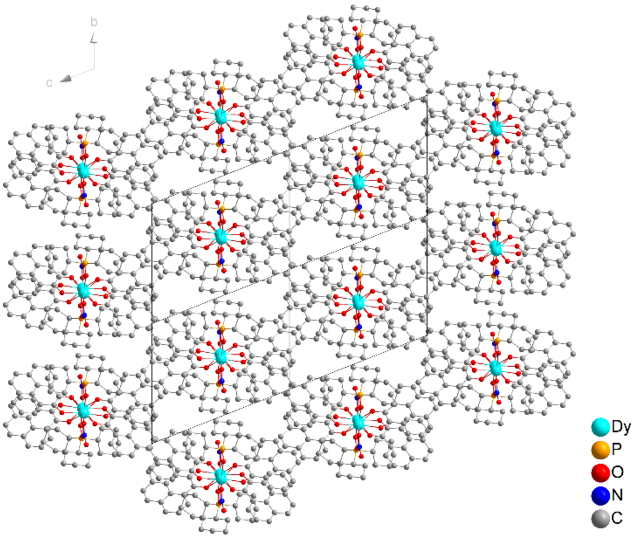

Figure 3.25. Packing views of the molecular structure of [$Dy_2(pysq)_4(tcypo)_2(NO_3)_2$]; organic H-atoms omitted for clarity.

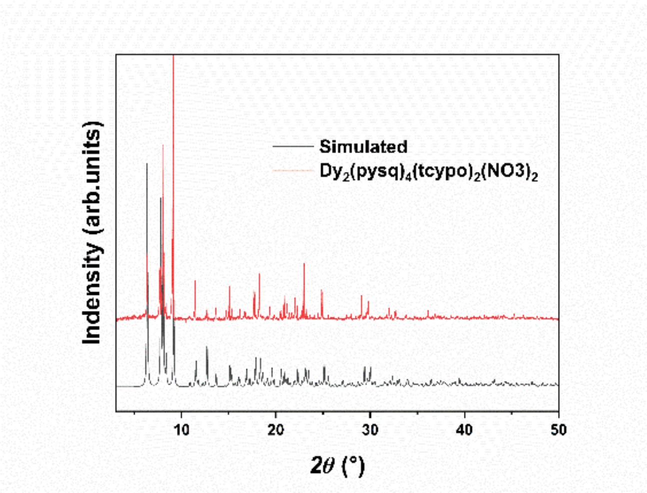

Figure 3.26. Powder-XRD of the [$Dy_2(pysq)_4(tcypo)_2(NO_3)_2$] compound

3.4.2 Magnetic properties of [$Dy_2(pysq)_4(tcypo)_2(NO_3)_2$]

Direct current (dc) magnetic susceptibility measurements were performed on microcrystalline samples of $[Dy_2(pysq)_4(tcypo)_2(NO_3)_2]$ in the range 2−300 K under applied magnetic field of 0.1 T and 1 T. The room temperature $\chi_M T$ value of 27.43 $cm^3\ K\ mol^{-1}$ is close to the theoretical value of 28.34 $cm^3\ K\ mol^{-1}$ for two noninteracting free Dy^{III} ions (ground state $^6H_{15/2}$, $S = 5/2$, $L = 5$, and $g = 4/3$). The $\chi_M T$ product remain unchanged until ~100 K, then it decreases smoothly upon further cooling until ~30 K and the reduce sharply under an applied DC field 1 T, and reaching a value of 8.7 $cm^3\ K\ mol^{-1}$ at 2 K for 1 T (Figure 3.27). The rapid decline of the $\chi_M T$ product upon lowering the temperature is mostly due to the depopulation of the crystal field m_J sub-levels and the intramolecular antiferromagnetic interactions between the two Dy^{III} ions.

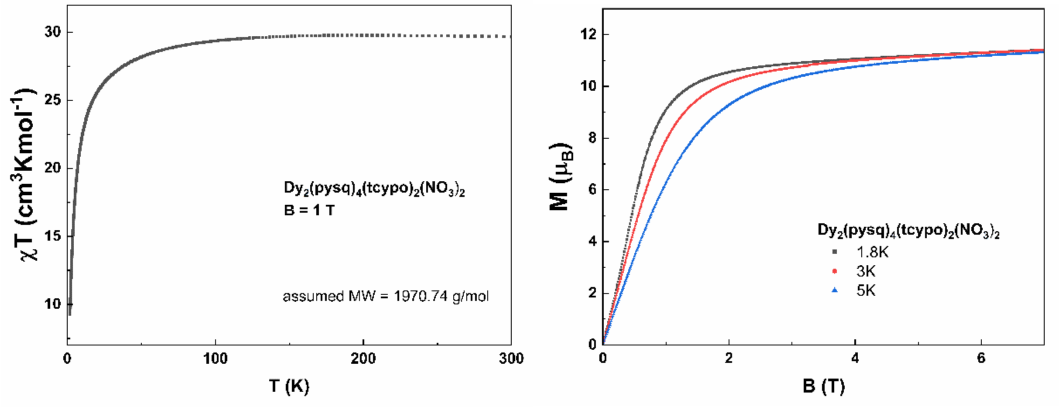

Figure 3.27. $\chi_M T$ vs T plot of $[Dy_2(pysq)_4(tcypo)_2(NO_3)_2]$ measured between 1.8 and 300 K under applied dc magnetic fields of 0.1 T and 1 T (left), and magnetization (M) vs. applied field (B) plots at different temperatures (right).

In the reduced magnetization plots the curves do not overlap suggesting significant anisotropy and/or the presence and involvement of low-lying excited states. The magnetizations of $[Dy_2(pysq)_4(tcypo)_2(NO_3)_2]$ complex measured against applied magnetic fields at 1.8, 3 and 5 K reveal a rapid increase at low magnetic fields (Figure 3.27 right). At high magnetic fields, magnetization increases gradually and finally reaches ca. 11.24 μ_B at 7 T (Figure 3.27 right), which almost meets the saturation value of 5 μ_B for an Ising-like Dy^{III}[183].

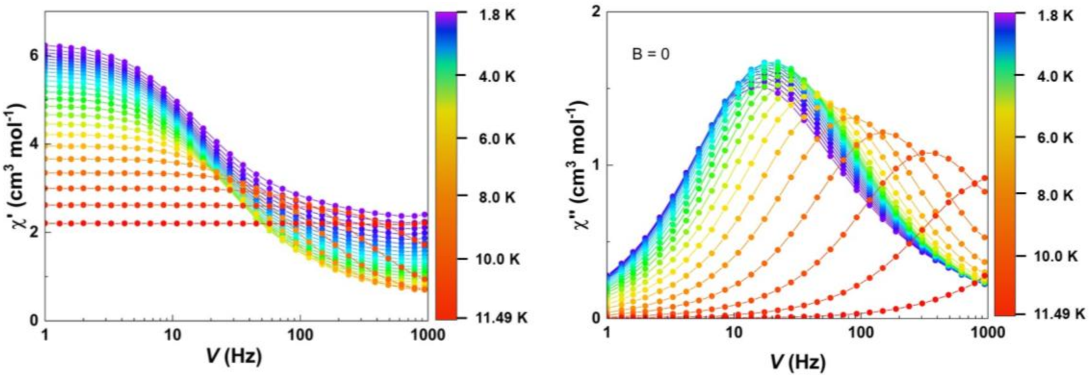

Figure 3.28. In-phase (left) and out-of-phase (right) ac susceptibility vs frequency measured on [Dy$_2$(pysq)$_4$(tcypo)$_2$(NO$_3$)$_2$] at temperatures between 1.8 K and 11.5 K with zero field.

Alternating Current (ac) susceptibility experiments were conducted at zero applied dc field in the temperature range 1.8 K to 11.49 K (Figure 3.28 left). Slow relaxation of magnetization can be observed with maxima in the out-of-phase susceptibility in measurements with ac fields switching direction at frequencies between 1 and 1000 Hz, which indicates the existence of a slow magnetization relaxation phenomenon characteristic of SMMs. A double generalized Debye model was used to analyze the relaxation processes.

The Cole-Cole plot approximates a semicircle (Figure 3.29 left), consistent with the generalized Debye model. It plots the relaxation time of complex [Dy$_2$(pysq)$_4$(tcypo)$_2$(NO$_3$)$_2$] at different temperatures in the Figure 3-28 right. The plot of ln(τ) versus 1/T deviates from a straight line and exhibits a bend at high temperatures, indicating the presence of Raman and Orbach processes and a plateau at low temperature for QTM.

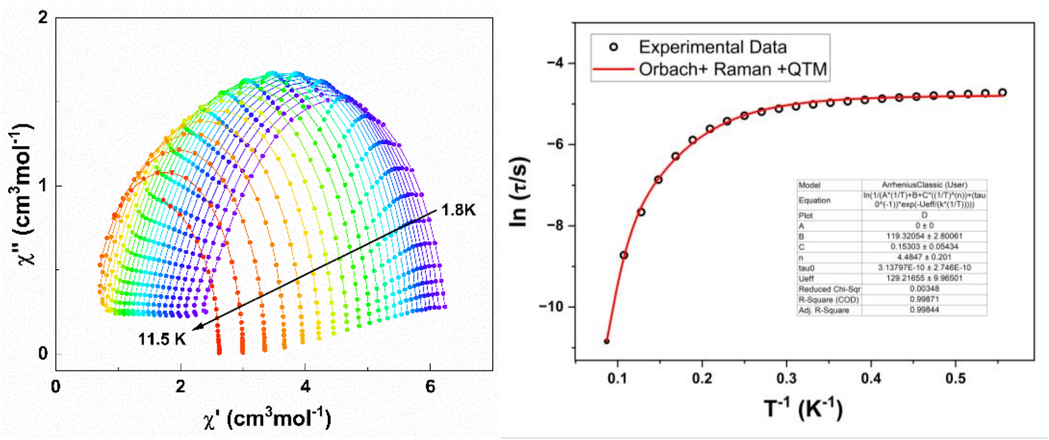

Model	ArrheniusClassic (User)
Equation	ln(1/(A*(1/T)+B+C*((1/T)^(n))+(tau0^(-1))*exp(-Ueff/(k*(1/T)))))
Plot	D
A	0 ± 0
B	119.32054 ± 2.80061
C	0.15303 ± 0.05434
n	4.4847 ± 0.201
tau0	3.13797E-10 ± 2.746E-10
Ueff	129.21655 ± 9.96501
Reduced Chi-Sqr	0.00348
R-Square (COD)	0.99871
Adj. R-Square	0.99844

Figure 3.29. Cole-Cole plot at different temperatures (left). ln(τ) versus T^{-1} for $[Dy_2(pysq)_4(tcypo)_2(NO_3)_2]$, solid red line represents the best-fit for magnetization relaxation (right).

Equation	$\tau^{-1} = AT + B + CT^n + \tau_0^{-1}\, exp^{-\frac{U_{eff}}{K_B T}}$
A	0
B	119.32054 ± 2.80061
C	0.15303 ± 0.05434
n	4.4847 ± 0.201
τ_0	3.13797E-10 ± 2.746E-10
U_{eff}	129.21655 ± 9.96501
Reduced Chi-Sqr	0.00348
R-Square (COD)	0.99871
Adj. R-Square	0.99844

Table 3.5. Fitting parameters for the relaxation process of Figure 3.29 right

A plot of the natural logarithm of ln(τ) versus 1/T was shown in the figure 3.20 right. According to equation (1) of Chapter 2, a best fitting was obtained for $[Dy_2(pysq)_4(tcypo)_2(NO_3)_2]$ yielding the parameters τ_0 = 3.14 x 10^{-10} s, U_{eff} = 129.22 K, C = 0.15 s^{-1} K^{-n}, n = 4.48 and B = 119.32 s^{-1} (τ_{QTM} = 8.38 x 10^{-3} s) (Table 3.5) which means that the direct, Orbach and QTM relaxation process were taken into account. We were able to observe a platform at low temperatures, which clearly indicates that the QTM process is occurring.

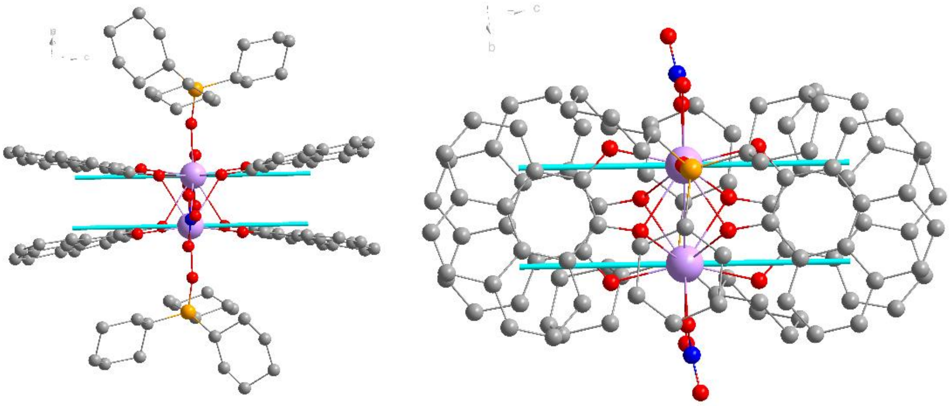

Figure 3.30. The side view (left) and top view (right) of anisotropy axes calculated using MAGELLAN on the crystal structure of $[Dy_2(pysq)_4(tcypo)_2(NO_3)_2]$

The anisotropy axes of $[Dy(pysq)_4(tcypo)_2(NO_3)_2]$ were calculated using MAGELLAN and are oriented the same way as in the $[Dy(phsq)_4(tppo)_2(NO_3)_2]$ compound (Figure 3.30). The axes are essentially orthogonal to the Dy-Dy vector, which means the dipolar interaction will be antiferromagnetic.

3.5 Conclusion and Outlook

This chapter described the modification of the radical ligand to pyrene-4,5-dione (pysq) which enhances the π-π interactions. Furthermore, by introducing tppo or tcypo and pysq-radicals in addition to the pysq-radicals into Ln_2 systems, six compounds were successfully synthesized $[Ln_2(pysq)_4(tppo)_2(NO_3)_2]$ (Ln = Nd, Gd, Dy, Ho, Er) as well as the $[Dy_2(pysq)_4(tcypo)_2(NO_3)_2]$ compounds. In the $[Ln_2(pysq)_4(tppo)_2(NO_3)_2]$ system (Ln = Nd, Gd, Dy, Ho, Er), Nd_2, Dy_2, and Er_2 complexes exhibit slow relaxation of the magnetization. Notably, the Dy compound features a Dy···Dy distance of 3.418 Å, slightly shorter than that in $[Dy_2(phsq)_4(tppo)_2(NO_3)_2]$. Furthermore, the molecule exhibits a maximum ac magnetic susceptibility at 20 K (1000 Hz) in the absence of an external magnetic field. In contrast, the maximum ac magnetic susceptibility of $[Dy_2(pysq)_4(tcypo)_2(NO_3)_2]$, is 11.47 K (1000 Hz) without an external magnetic field.

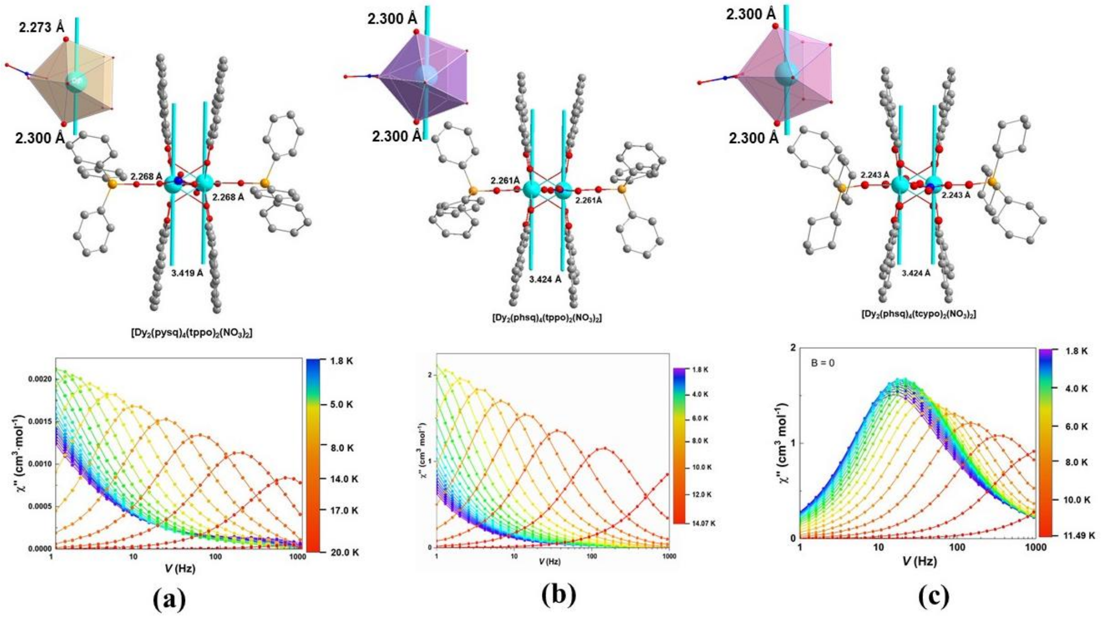

Figure 3.31. Anisotropy axes (top) and corresponding AC magnetic susceptibility curve (bottom) of $[Dy(pysq)_4(tppo)_2(NO_3)_2]$ **(a)**, $[Dy(phsq)_4(tppo)_2(NO_3)_2]$ **(b)** and $[Dy_2(phsq)_4(tcypo)_2(NO_3)_2]$ **(c);.**

For the Dy compounds, and in comparison, with the analysis presented in Chapter 2, we found that the anisotropy axes are all oriented perpendicular to the Dy-Dy vector. Modifying the phsq ligand to a pysq ligand shortens the Dy-O bond length along the axial direction from 2.30 Å to 2.27 Å (Figure 3.31), which enhances the axial crystal field energy, thereby increasing the maximum AC magnetic susceptibility from 14.07 K to 20 K. Furthermore, replacing tppo with tcypo reduces the equatorial Dy-O bond distance from 2.26 Å to 2.24 Å, indicating an improvement in the equatorial crystal field, weakening the axiality and reducing the maximum AC magnetic susceptibility from 14.07 K to 11.49 K.

Combining the findings from Chapters 2 and 3, it could be established that in this semiquinone radical system, the radical ligands do not play a classic bridging role like the N-based radicals present in the literature. Instead, the four semiquinone radicals tightly bind the lanthanide ions, which results in a short Dy---Dy distance. In addition, the anisotropic axis is aligned along the direction of the semiquinone radicals, perpendicular to the Ln-Ln vector. Based on the principles established in the existing system, strategies can be designed to enhance performance. Three approaches are available to improve its magnetic properties for the semiquinone radical system. Firstly, alternative semiquinone radicals can be designed in order to force the lanthanide ions closer together, thereby enhancing the dipolar coupling which quenches QTM and increasing the anisotropy along the radical direction. Secondly, in order to weaken the equatorial crystal field energy along the Ln-Ln direction, the suitable ligands that bind more weakly to the lanthanide than tppo and tcypo ligand, will increase the axial crystal field energy of the entire system. Furthermore, the nitrate group is also located in the equatorial plane, suggesting the possibility of finding alternative anionic ligands with weaker binding energies than nitrate. These three approaches represent our efforts to improve the magnetic properties of this semiquinone radical system.

Chapter 4. Structure、Magnetic and Luminescent Properties of Lanthanide-DOTA Complexes and Its Derivatives

4.1 Introduction

H_4DOTA is a well-established and classic ligand, and numerous studies on it have been reported in the literature since 1986[196-198]. In particular, there are a lot of reports in medical imaging, especially [NaGd(DOTA)(H_2O)]·4H_2O is a reliable and excellent Magnetic Resonance Imaging (MRI). Since 2003, numerous studies have reported on DOTA ligands in paramagnetic chemical exchange saturation transfer. Furthermore, in 2011, professor Robert[199] conducted the first study of the single-molecule magnetism in the classic [NaDy(DOTA)(H_2O)]·4H_2O structure (Figure 4.1).

The presence of unique symmetry and axial water molecules enable the structure to exhibit single-molecule magnetic behavior[200]. In addition, its luminescence properties are also reported[201]. At the same time, many DOTA derivative compounds[202-203] have been reported (Figure 4.2). As for the structure of DOTA ligand itself, it contains pockets of nitrogen atoms that can accept 3d ions and pockets of oxygen atoms that can accept 4f ions, which creates the possibility for 3d-4f.

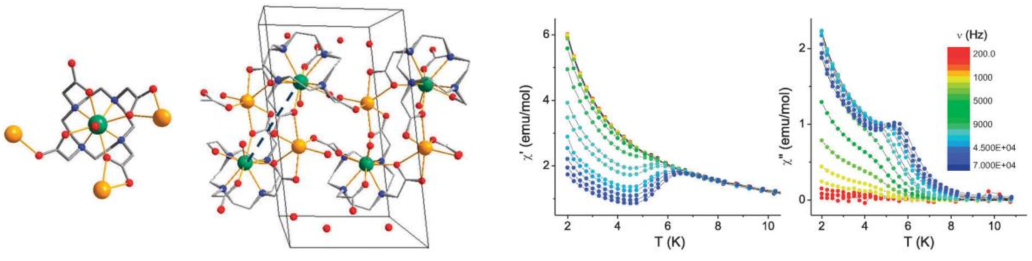

Figure 4.1. Crystal structure（left）and magnetic properities (right) of

Na[Dy(DOTA)(H_2O)]·4H_2O; Copyright © 2011, Royal Chemistry Society.

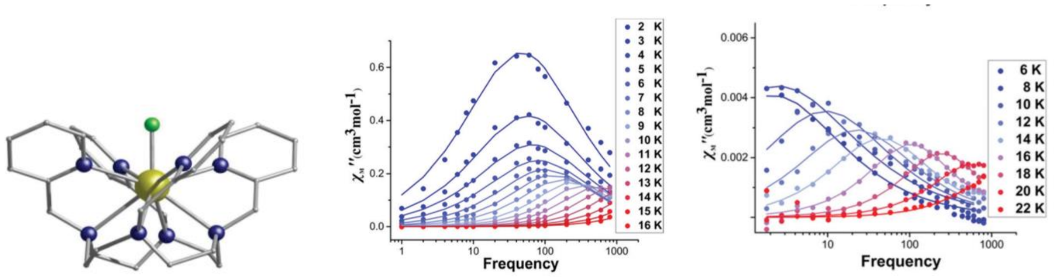

Figure 4.2. Crystal structure （left） and magnetic properities （right） of [Dy^{III}LF](CF_3SO_3)·2H_2O (L = 1,4,7,10-tetrakis(2-pyridylmethyl)- 1,4,7,10-tetraaza-cyclododecane); Copyright © 2019, Royal Chemistry Society.

Based on the above considerations, we simultaneously introduced the transition metal Zn (II) and lanthanide metals into the DOTA framework.

4.2 Structure and Characterization of [$Dy_2Zn_2(DOTA)_2(H_2O)_{10}$•($ZnCl_4$)]

This compound was obtained by acetone vapor after stirring the aqueous solution at 80 °C for several days, yielding stable, colorless block-shaped crystals (Figure 4.3, right).

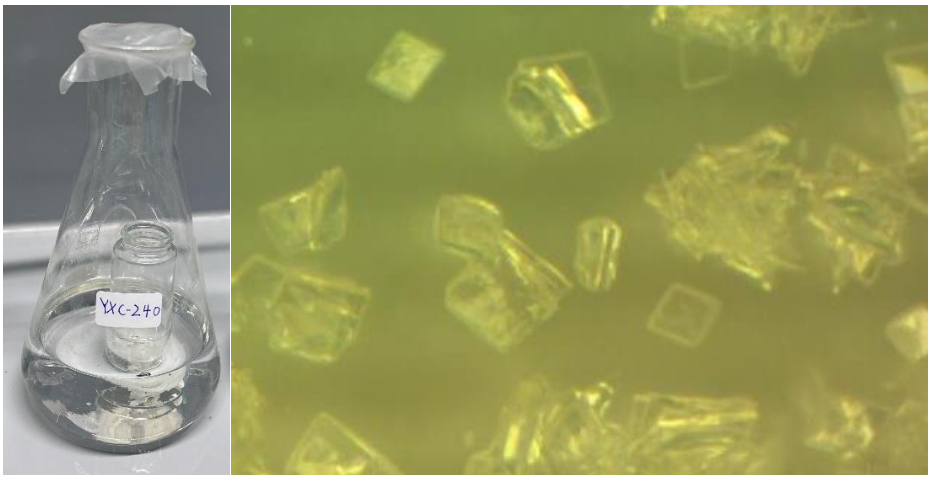

Figure 4.3. Crystal growth by vapor diffusion method (left); Crystal morphology under

a microscope (right).

First, we synthesized [Zn(H_2DOTA)]. In this structure, Zn (II) is coordinated by six atoms, with four nitrogen atoms and two oxygen atoms coordinated (Figure 4.4). The two oxygen atoms come from the carboxyl arm of the DOTA ligand. The oxygen atoms of the remaining two carboxyl arms are uncoordinated and positioned at the free ends. After obtaining Zn(H_2DOTA), we further mixed this compound with $DyCl_3$, refluxed it at 80 °C for a few days, and then carried out vapor diffusion in acetone to obtain bulk crystals (Figure 4.3). Single crystal X-ray diffraction analyses of the compounds show that it crystallizes in $P2_1/c$. The centrosymmetric molecule consists of a dinuclear lanthanide unit bridged by two DOTA ligands (Figure 4.4). Each Dy ion is coordinated by nine oxygen atoms in a capped square-antiprismatic O9 geometry. Of these oxygen atoms, five originate from water molecules, and four come from the carboxyl groups of the DOTA ligand.

In addition, the center of each DOTA ligand is occupied by Zn (II), meaning that the four nitrogen atoms of the DOTA ligand and the two oxygen atoms from its carboxyl arms coordinate with the Zn ion. As a result, Zn(II) is six-coordinate, forming a regular octahedral structure influenced by the Jahn-Teller effect. A ring structure is formed in which two Dy ions are each coordinated to two Zn(DOTA) units, creating a cyclic assembly.

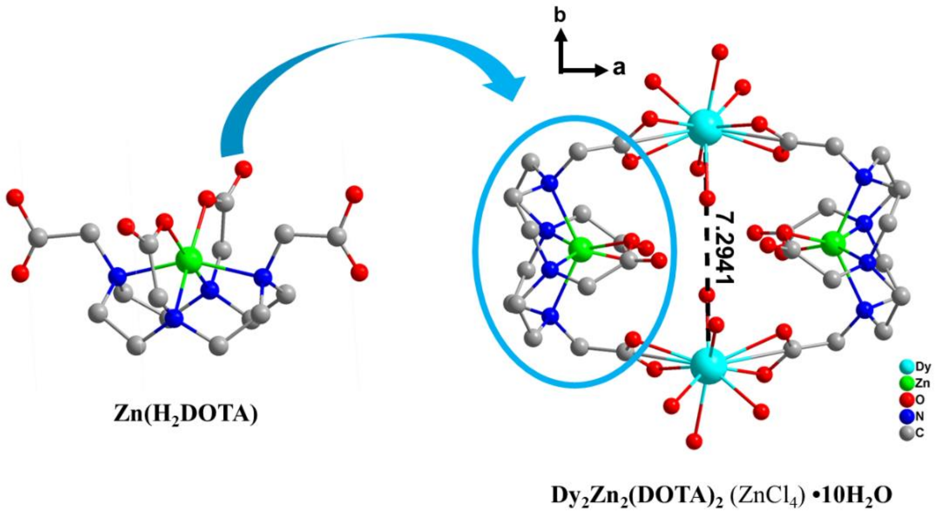

Figure 4.4. Top view (left) and coordination environment of Dy atoms (right) in the molecular structure of [$Dy_2Zn_2(DOTA)_2(H_2O)_{10}$•($ZnCl_4$)]; organic H-atoms omitted for clarity.

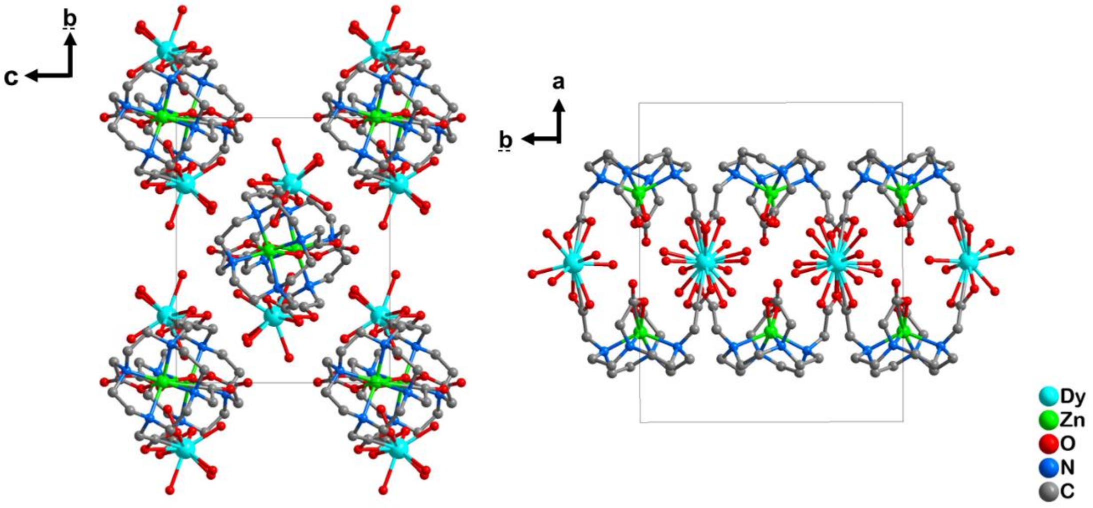

Figure 4.5. The packing arrangement in [$Dy_2Zn_2(DOTA)_2(H_2O)_{10}$•($ZnCl_4$)] structure viewed along the a-axis (left) and c-axis (right); hydrogen atoms omitted for clarity.

Phase purity of the bulk sample was confirmed by powder X-ray diffraction (PXRD) which matches the simulated diffraction pattern (Figure 4.6, left) and elemental analysis was consistent with the expected composition. In the IR spectrum (Figure 4.6, right) the antisymmetric CO stretch band at 1430 cm^{-1} can be identified consistent with IR spectra of multidentate CO_3^{2-} anions in metal complexes in the literature.

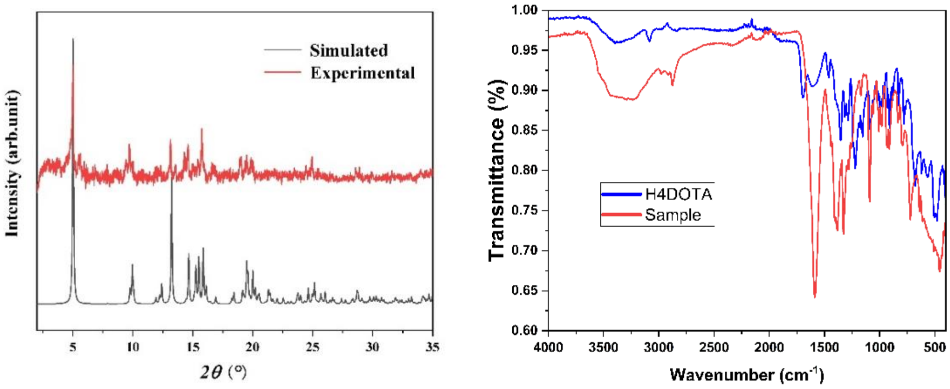

Figure 4.6. PXRD confirming the phase purity (left) and the IR spectrum of between 4000 and 400 cm^{-1} highlighting the asymmetric CO stretch vibration of the multidentate CO_3^{2-} ligand at 1430 cm^{-1} (right) of $[Dy_2Zn_2(DOTA)_2(H_2O)_{10}•(ZnCl_4)]$.

Direct current (dc) magnetic susceptibility measurements were performed at temperatures between 1.8 and 300 K with an applied field of 0.1 T. The χ_MT value of 27.96 cm^3 K mol^{-1} of $[Dy_2Zn_2(DOTA)_2(ZnCl_4)•10H_2O]$ at 300 K is in very good agreement with the theoretical value of 28.34 cm^3 K mol^{-1}. On decreasing the temperature, the χ_MT values stay essentially constant to 50 K below which a steep decrease can be observed leading to a minimum value of 5.48 cm^3 K mol^{-1} at 1.8 K (Figure 4.7, left). There is a weak antiferromagnetic interaction between the two Dy^{III} ions.

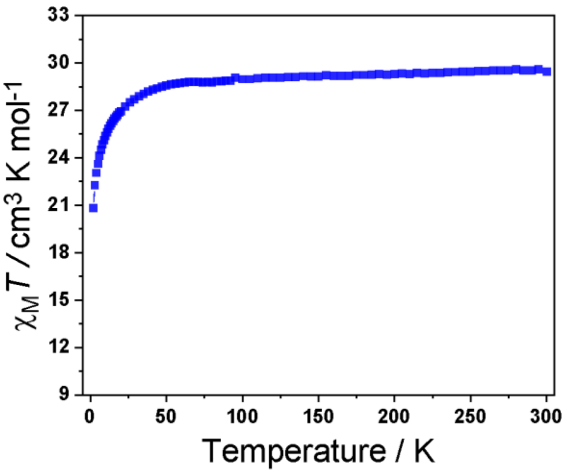

Figure 4.7. χ_MT vs T plot of [$Dy_2Zn_2(DOTA)_2(H_2O)_{10}$•($ZnCl_4$)] obtained from susceptibility measurements at temperatures between 1.8 and 300 K and an applied magnetic dc field of 0.1 T

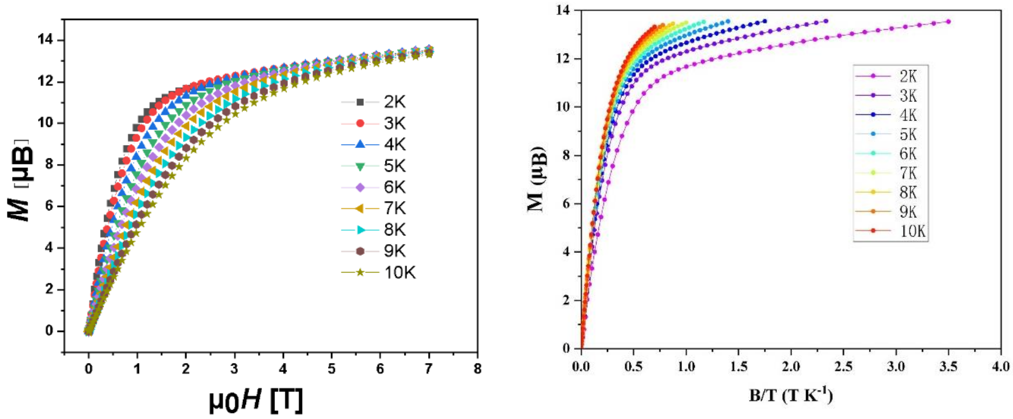

Figure 4.8. Magnetisation measurements at dc fields between 0 and 7 T (left) and reduced magnetisation plot (right) for [$Dy_2Zn_2(DOTA)_2(H_2O)_{10}$•($ZnCl_4$)] showing the anisotropy of the system.

Magnetization measurements were performed at 2, 3, 4, 5, 6, 7, 8, 9 and 10 K under magnetic fields ranging from 0 and 7 T. The magnetization intensity has not reached saturation and there is still a slope at the external dc magnetic field 7 T (Figure 4.8, left). The reduced magnetisation is plotted in Figure 4.8 (right). The non-superposition of the plots as well as not reaching the expected saturation value hints at significant anisotropy and crystal field effects lifting the degeneracy of the 8 sub states of the $^6H_{15/2}$ ground state[204-205].

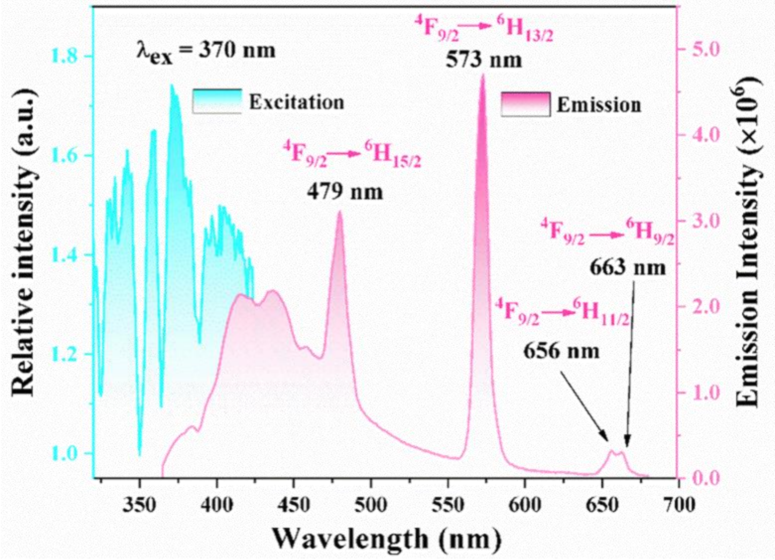

Figure 4.9. Excitation (blue part) and emission (pink part) spectra of $[Dy_2Zn_2(DOTA)_2(H_2O)_{10}•(ZnCl_4)]$

Solid-state photoluminescence studies at room temperature were performed. The excitation and emission spectra are displayed in Figure 4.9. The excitation spectra show broad bands with a maximum at around 370 nm, indicating the ligand-centered transitions of DOTA. The emission spectrum of Dy DOTA is assigned to $^4F_{9/2} \rightarrow {}^6F_J$ (J= 9/2−15/2) transitions under excitation at 350 nm. As shown in the Figure 4.9, the emission peak at 479 nm is indicated a transition at $^4F_{9/2} \rightarrow {}^6F_{15/2}$, the emission peak at 573 nm is indicated a transition at $^4F_{9/2} \rightarrow {}^6F_{13/2}$, the emission peak at 656 nm is indicated a transition at $^4F_{9/2} \rightarrow {}^6F_{11/2}$, the emission peak at 663 nm is indicated a transition at $^4F_{9/2} \rightarrow {}^6F_{9/2}$.

4.3 Structure of $[\mathrm{Dy_4Zn_4(DOTA)_4(H_2O)_{16}{\bullet}Cl_4}]$

By varying the reaction pH under conditions identical to those for $[\mathrm{Dy_2Zn_2(DOTA)_2(H_2O)_{10}{\bullet}(ZnCl_4)}]$, the new compound $[\mathrm{Dy_4Zn_4(DOTA)_4(H_2O)_{16}{\bullet}Cl_4}]$ was synthesized. This structure can be regarded as a dimer of the previously mentioned structure $[\mathrm{Dy_2Zn_2(DOTA)_2(H_2O)_{10}{\bullet}(ZnCl_4)}]$ unit. As shown in Figure 4.10, the structure contains two rings, labeled as left and right in the figure, which are connected via carboxylate oxygen atoms that bridge between Dy ions of the two rings. In other words, the oxygen atoms of the carboxyl groups coordinate to Dy ions in both rings, forming a Dy–O–Dy linkage that holds the dimer together. The Dy---Dy distance between the two rings is 4.2564 Å, while the Dy---Dy distances within the left and right rings are 6.9444 Å and 6.9547 Å, respectively. The two outermost Dy ions are both nine-coordinated, each binding to five water molecules and four oxygen atoms from the carboxyl arms of the DOTA ligand. Moreover, the side view of the dimer ring (Figure 4.11) shows that the two rings are not coplanar but are connected at a specific angle. The packing arrangement of this structure is shown in Figure 4.12.

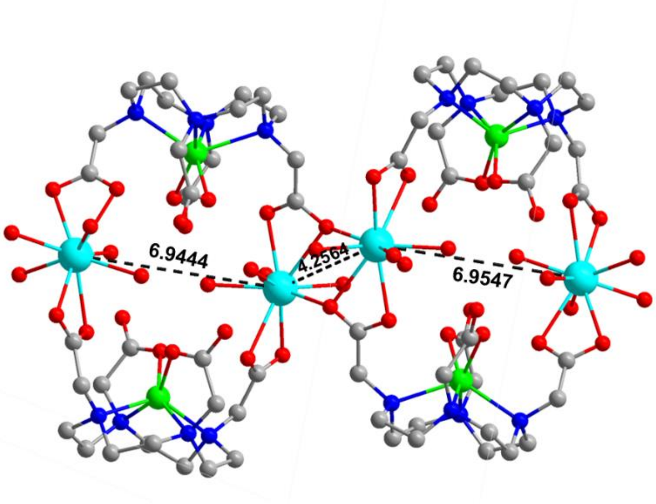

Figure 4.10. Top views and coordination environment of Dy atoms of the molecular

structure of [$Dy_4Zn_4(DOTA)_4$ $(H_2O)_{16}$•Cl_4]; organic H-atoms omitted for clarity.

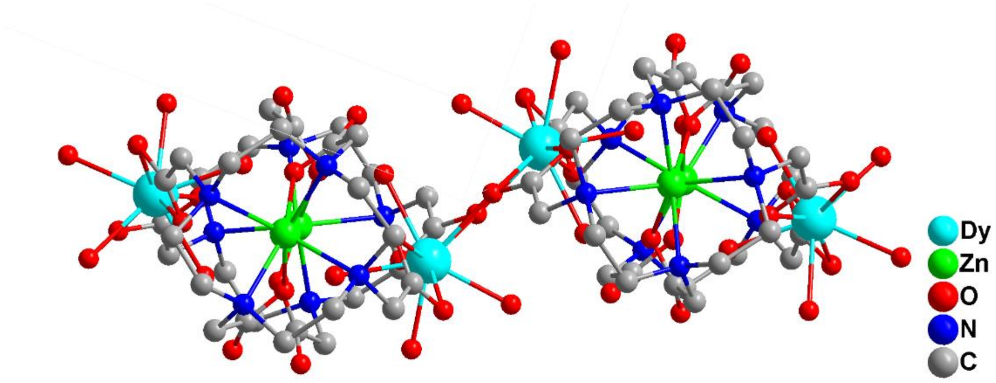

Figure 4.11. Side view and coordination environment of Dy atoms of the molecular structure of [$Dy_4Zn_4(DOTA)_4$ $(H_2O)_{16}$•Cl_4]; organic H-atoms omitted for clarity.

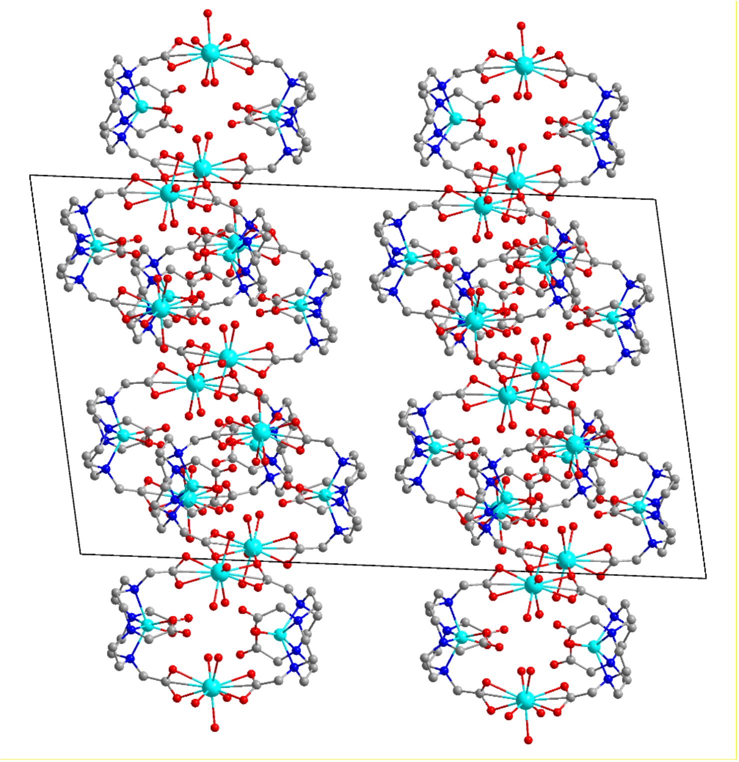

Figure 4.12. The packing arrangement of the [$Dy_4Zn_4(DOTA)_4$ $(H_2O)_{16}$•Cl_4] structure. H-atoms omitted for clarity.

Based on the structural features of the ZnDy-DOTA compounds, the DOTA ligand has a limited number of coordination sites. In the complex, the Zn ion occupies six of these sites, which restricts the available coordination positions for Dy. As a result, when Dy is incorporated, it cannot fully coordinate with the DOTA ligand and instead binds to a large number of water molecules, at least five in this case. Such extensive coordination with water molecules is highly unfavorable for the photoluminescence properties of Dy, as the O-H vibrations of water can efficiently quench the excited states of the Dy(III) ions. It is well known that Dy(III) ions exhibit optimal single-molecule magnetic behavior when situated in a highly symmetric coordination environment, which explains the good magnetic properties observed in [Dy(DOTA)] complexes. Taking this into account, we designed a new ligand, H_4tapen, which offers a greater number of coordination sites. The expanded coordination capacity of H_4tapen allows for the formation of 3d-4f heterometallic complexes. Importantly, even when the transition metal occupies six coordination sites, the ligand still provides enough remaining sites for Dy to achieve a high-symmetry environment. This design enhances the probability of achieving single-molecule magnet behavior in Dy(III) complexes.

4.4 The structure of [Dy(H_2tapen)]

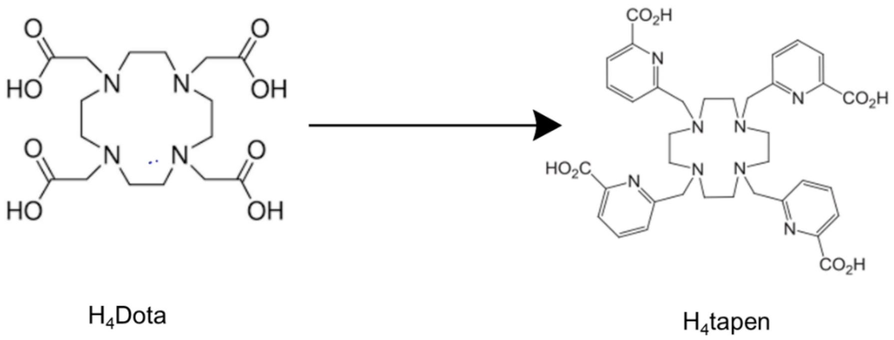

Figure 4.13. Structure of H_4tapen ligand

First, $ZnCl_2$ was reacted with H_4tapen to synthesize the Zn(II)(H_2tapen) complex. In this compound, the Zn^{2+} ion adopts a six-coordinate geometry, similar to that observed in Zn(II)(H_2DOTA). The coordination sphere of Zn(II) consists of five nitrogen atoms and one oxygen atom: four of the nitrogen atoms originate from the central nitrogen donors of H_4tapen, while the fifth nitrogen comes from the pyridine group attached to one of the carboxyl arms. The oxygen atom from the same carboxyl arm also coordinates to Zn(II) (Figure 4.14). As a result, three of the carboxyl arms remain uncoordinated, terminating as free ends that are available for binding additional metal ions.

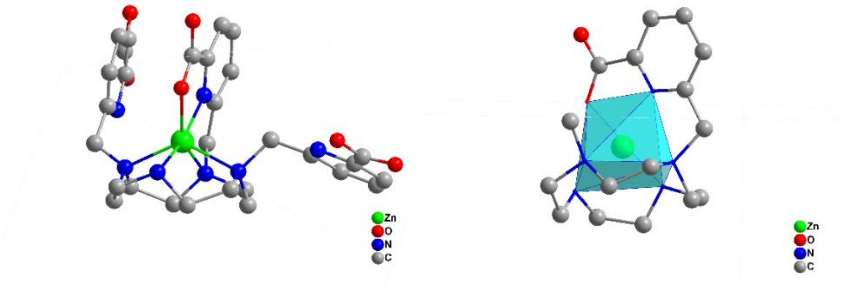

Figure 4.14. the structure of [Zn(H_2tapen)]

In addition, we also synthesized [Dy(H_2tapen)] complex. As shown in Figure 4.15, the Dy(III) ion adopts an eight-coordinate geometry. Its coordination sphere comprises six nitrogen atoms and two oxygen atoms: four nitrogen atoms come from the central nitrogen donors of the H_4tapen ligand, while the remaining two nitrogen atoms are from the pyridine groups on two of the carboxyl arms. Each of these two carboxyl arms also contributes one oxygen atom, completing the Dy^{III} coordination environment (Figure 4.16).

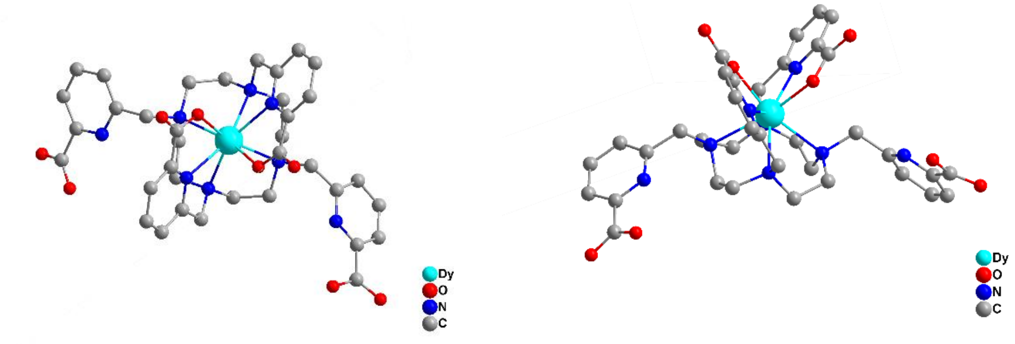

Figure 4.15. Top view (left) and side view (right) of the Dy(H_2tapen) structure

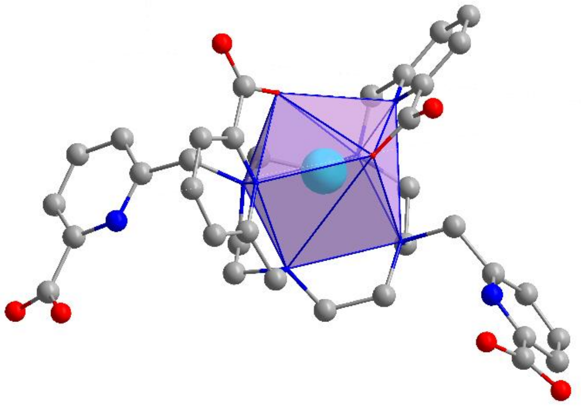

Figure 4.16. Coordination environment of Dy atom in the Dy(H_2tapen)

Powder X-ray diffraction (PXRD) analysis confirmed the phase purity of the sample, with the experimental pattern matching the simulated data, demonstrating that no impurities were present. Photoluminescence measurements showed that the emission spectrum lacked the characteristic peaks of Dy(III) ions.

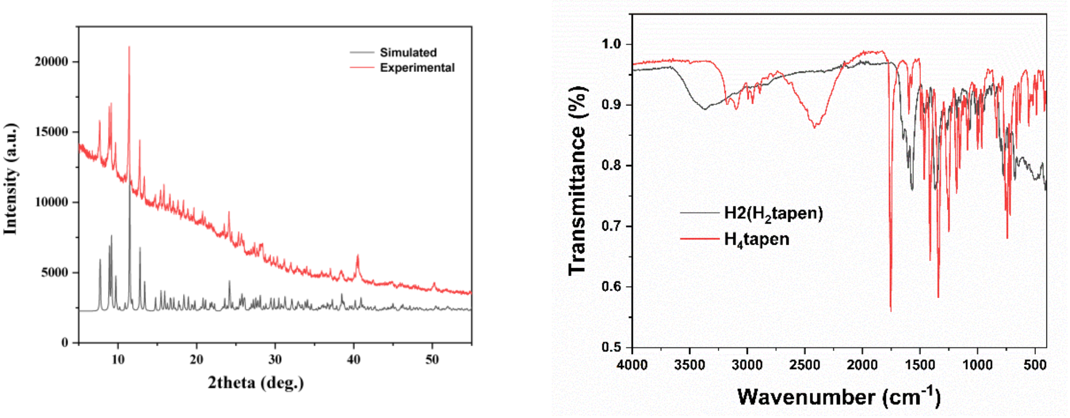

Figure 4.17. Powder-XRD confirming the phase purity of Dy(H_2tapen) (left) and the IR spectrum of [Dy(H_2tapen)] between 4000 and 400 cm^{-1} (right).

Although we have successfully synthesized Zn(II) and Dy(III) complexes with the H_4tapen ligand individually, our ultimate goal is to obtain 3d-4f heterometallic complexes, such as ZnDy-H_4tapen. From the perspective of ligand coordination, the available binding sites theoretically allow the formation of such compounds. However, to date, we have not yet obtained suitable single crystals for X-ray diffraction analysis.

4.5 Conclusion and Outlook

In chapter 3, three Dy(III) compounds were reported, two of which were compounds of Dy and transition metal Zn(II) coordinated with DOTA, which is the first DOTA compound with 3d-4f synthesized so far. Among them, [$Dy_4Zn_4(DOTA)_4 16H_2O•Cl_2$] is a dimer of this, connected to it through the oxygen atoms of the two carboxyl arms, and the distance between the connected Dy---Dy is 4.26 Å. The magnetic properties and luminescence properties of [$Dy_2Zn_2(DOTA)_2(H_2O)_{10}•(ZnCl_4)$] were characterized. From the DC magnetic data, it can be seen that there is an antiferromagnetic interaction between Dy in this compound. But the compound does not show slow relaxation behavior. At the same time, we studied its photoluminescence behavior. The emission spectrum shows the characteristic emission peak of Dy(III), which showed that the DOTA ligand was a good antenna ligand for the luminescence of lanthanide ions. In addition, we used DOTA as a template, although we have successfully synthesized transition metal and lanthanide complexes with DOTA, the Dy ions are coordinated with multiple water molecules, resulting in a low-symmetry coordination environment.

Based on these considerations, we modified the carboxyl arms of DOTA by introducing pyridine groups, thereby increasing the number of available coordination sites. This design aims, on one hand, to prevent Dy ions from coordinating with solvent water molecules and, on the other hand, to ensure that sufficient sites remain for coordination with lanthanide metals even after the transition metal has bound. Using this strategy, we successfully synthesized the [Dy(Htapen)] complex. Although we also obtained [Zn(H_2tapen)] compounds, we were unable to identify a suitable method to introduce both metals simultaneously and obtain a new 3d-4f DOTA-derivative complex.

5. Experimental Section

5.1 Materials and Instruments

General Procedure

Commercially available chemicals were used as received without further purification. Lanthanide salts are prepared by reacting the corresponding oxides with acids. All procedures were performed at ambient conditions in air.

Instruments

The single-crystal X-ray diffraction (SC-XRD) data of the complexes were collected using STOE StadiVari 25 diffractometer with a Pilatus300K detector using GeniX 3D HF micro focus with Mo-K_α radiation (λ= 0.71073 Å), on a STADIVARI by STOE with Ga-Jet X-ray source by Excilium using Ga-K_α radiation with a wavelength of 1.3143 Å and on an IPDS II by STOE with Mo-K_α radiation. The structures were solved using direct methods and were refined by full-matrix least square methods and using SHELX 2014[206] inbuilt in Olex[207].

Powder X-ray diffraction (PXRD) patterns were obtained using a Rigaku MiniFlex 600-C diffractometer with a Rigaku D/teX Ultra2 detector at 298 K, and the measurement underwent voltage and intensity were 45 kV and 40 mA with a Cu Kα irradiation source (λ=1.54056 Å). The 2θ range was 5-60° with a scan step width of 0.02° and a fixed counting time of 0.40 s/step.

IR spectroscopy was performed on a Bruker Platinum Alpha ATR IR.

^{1}H NMR spectra were recorded on a Bruker Avance III 300MHz spectrometer. Chemical shifts are reported in parts per million relative to the residual proton signal of the solvent $CDCl_3$ (7.26 ppm).

The emission and excitation spectra were recorded at 300 K using a spectrofluorometer Edinburgh FLS-920. The excitation source was a 450 W Xe arc lamp. The emission spectra were corrected for detection and optical spectral response of the spectrofluorometer.

Magnetic susceptibility measurements were performed by Dr. Jan Arneth from the research group of Prof. Dr. Rüdiger Klingeler using a Quantum Design MPMS-3 SQUID magnetometers on polycrystalline material in the temperature range of 2-300 K under an applied DC magnetic field (H_{DC}) of 0.1 T and 1 T. Variable-temperature magnetic susceptibility ware collected with an external magnetic field of 1000 Oe in the temperature range of 2-300 K. Magnetic hysteresis loops were collected using a Quantum Design MPMS3 magnetometer in warming mode. Alternating current (AC) magnetic susceptibility measurements were performed using a Quantum Design MPMS3 magnetometer using an oscillating field of 3 Oe. The experimental magnetic susceptibility data were corrected for diamagnetic contribution estimated from Pascal’s constant and sample holder calibration.

Low temperature (0.03–5 K) magnetic measurements were performed on single crystals using a Micro-SQUID apparatus at different sweep rates between 1 and 128 $mT{\cdot}s^{-1}$. The time resolution is approximately 1 ms. The measurements were performed by Appu Sunil from the group of Prof. Dr. Wolfgang Wernsdorfer

5.2 Synthesis

5.2.1 $[Ln_2(phsq)_4(tppo)_2(NO_3)_2]$ (Ln = Y^{III}, Ce^{III}, Nd^{III}, Sm^{III}, Eu^{III}, Gd^{III}, Tb^{III}, Dy^{III}, Ho^{III}, Er^{III}, Tm^{III}, Yb^{III}, Lu^{III})

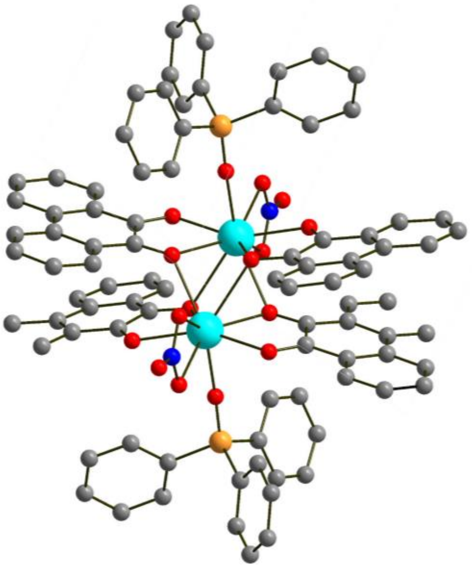

A Teflon insert was loaded with 9,10-phenanthrenequinone (70.0 mg, 0.35 mmol, 1.0 eq.), $Ln(NO_3)_3 \cdot xH2O$ (0.35 mmol, 1.0 eq.), Triphenylphosphine oxide (0.35 mmol 1.0 eq.) and 10 ml MeOH. The vessel was closed with a lid and put into a steel autoclave that was sealed tightly and put in an oven at 90°C for 1 week. The autoclave was cooled down to room temperature slowly by turning off the oven but leaving the oven door shut. After 24 h the autoclave was removed from the oven, opened and the contents were filtered. The product was obtained as dark crystals, after washing with methanol several times, the product was dried in air.

$[Ce_2(phsq)_4(tppo)_2(NO_3)_2]$ (1-Ce)

Amount of $Ce(NO_3)_3 \cdot 6H_2O$ used = 151.98 mg. IR (4000-400 cm^{-1}): 3062 (w), 2097 (b,w), 1620 (m), 1580 (w), 1565 (s), 1518 (m), 1477 (m), 1457 (m), 1436 (m), 1384 (w), 1369 (w), 1349 (m,b), 1330 (w), 1310 (m), 1280 (w), 1270 (w), 1226 (m), 1185 (w), 1159 (m,b), 950 (w), 1103 (m), 1090 (m), 1075 (m), 1039 (m), 1024 (s), 995 (w), 972 (w), 931 (s), 848 (m), 816 (m), 782 (w), 755 (s), 718 (s), 695 (m), 682 (m), 666 (w), 628 (w,b), 576 (s),536 (s), 492 (s), 431 (s).

$[Nd_2(phsq)_4(tppo)_2(NO_3)_2]$ (2-Nd)

Amount of $Nd(NO_3)_3·6H_2O$ used = 153.43 mg. IR (4000-400 cm-1): 3066 (w), 2097 (b,w), 1620 (m), 1580 (w), 1565 (s), 1518 (m), 1477 (m), 1457 (m), 1436 (m), 1384 (w), 1369 (w), 1349 (m,b), 1330 (w), 1310 (m), 1280 (w), 1270 (w), 1226 (m), 1185 (w), 1159 (m,b), 950 (w), 1103 (m), 1090 (m), 1075 (m), 1039 (m), 1024 (s), 995 (w), 972 (w), 931 (s), 848 (m), 816 (m), 782 (w), 755 (s), 718 (s), 695 (m), 682 (m), 666 (w), 628 (w,b), 576 (s),536 (s), 492 (s), 431 (s).

$[Sm_2(phsq)_4(tppo)_2(NO_3)_2]$ (3-Sm)

Amount of $Sm(NO_3)_3·6H_2O$ used = 155.57 mg. IR (4000-400 cm-1): 3062 (w), 2090 (b,w), 1601 (m), 1578 (w), 1564 (s), 1520 (s), 1472 (m), 1457 (m), 1438 (m), 1370 (w), 1369 (w), 1348 (m), 1332 (w), 1311 (m), 1282 (w), 1270 (w), 1225 (m), 1165 (w), 1116 (m,b), 1104(m), 1094(m), 1077(m), 1040(m), 1025(s), 996(m), 975(m), 950 (w), 931 (s), 863(w), 848 (m), 814 (m), 778 (w), 768 (w), 755 (s), 741(w), 717(w), 692 (m), 682 (m), 668 (w), 628 (w,b), 574 (s), 494 (s), 432 (s), 414 (w).

$[Eu_2(phsq)_4(tppo)_2(NO_3)_2]$ (4-Eu)

Amount of $Eu(NO_3)_3·6H_2O$ used = 156.13 mg. IR (4000-400 cm-1): 3061 (w), 2092 (b,w), 1601 (m), 1577 (w), 1565 (s), 1520 (s), 1472 (m), 1457 (m), 1438 (m), 1370 (w), 1369 (w), 1348 (m), 1331 (w), 1311 (m), 1282 (w), 1272 (w), 1225 (m), 1165 (w), 1116 (m,b), 1104(m), 1094(m), 1077(m), 1040(m), 1025(s), 996(m), 975(m), 950 (w), 931 (s), 863(w), 849 (m), 814 (m), 778 (w), 768 (w), 755 (s), 741(w), 717(w), 692 (m), 682 (m), 668 (w), 628 (w,b), 574 (s), 494 (s), 432 (s), 414 (w).

$[Gd_2(phsq)_4(tppo)_2(NO_3)_2]$ (5-Gd)

Amount of $Gd(NO_3)_3 \cdot 6H_2O$ used = 158.0 mg. IR (4000-400 cm^{-1}): 3061 (w), 2092 (b,w), 1601 (m), 1577 (w), 1565 (s), 1520 (s), 1472 (m), 1457 (m), 1438 (m), 1370 (w), 1369 (w), 1348 (m), 1331 (w), 1311 (m), 1282 (w), 1272 (w), 1225 (m), 1165 (w), 1116 (m,b), 1104(m), 1094(m), 1077(m), 1040(m), 1025(s), 996(m), 975(m), 950 (w), 931 (s), 863(w), 849 (m), 814 (m), 778 (w), 768 (w), 755 (s), 741(w), 717(w), 692 (m), 682 (m), 668 (w), 628 (w,b), 574 (s), 494 (s), 432 (s), 414 (w).

$[Tb_2(phsq)_4(tppo)_2(NO_3)_2]$ (6-Tb)

Amount of $Tb(NO_3)_3 \cdot 6H_2O$ used = 158.57 mg. IR (4000-400 cm^{-1}): 3062 (w), 2094 (b,w), 1601 (m), 1577 (w), 1566 (s), 1520 (s), 1472 (m), 1457 (m), 1438 (m), 1370 (w), 1369 (w), 1349 (m), 1331 (w), 1312 (m), 1282 (w), 1272 (w), 1225 (m), 1165 (w), 1116 (m,b), 1104(m), 1094(m), 1078(m), 1040(m), 1025(s), 997 (m), 975(m), 951 (w), 931 (s), 863(w), 849 (m), 814 (m), 777 (w), 769 (w), 755 (s), 741(w), 717(w), 692 (m), 682 (m), 668 (w), 628 (w,b), 574 (s), 494 (s), 433 (s), 416 (w).

$[Dy_2(phsq)_4(tppo)_2(NO_3)_2]$ (7-Dy)

Amount of $Dy(NO_3)_3 \cdot 6H_2O$ used = 159.82 mg. IR (4000-400 cm^{-1}): 3065 (w), 2091 (b,w), 1603 (m), 1577 (w), 1565 (s), 1521 (s), 1472 (m), 1459 (m), 1438 (m), 1372 (w), 1369 (w), 1347 (m), 1331 (w), 1313 (m), 1282 (w), 1273 (w), 1225 (m), 1165 (w), 1116 (m,b), 1104(m), 1094 (m), 1077(m), 1040(m), 1025(s), 996(m), 976 (m), 953 (w), 932 (s), 864 (w), 851 (m), 814 (m), 779 (w), 768 (w), 755 (s), 745 (w), 717(w), 692 (m), 682 (m), 668 (w), 628 (w,b), 574 (s), 494 (s), 432 (s), 415 (w).

$[Ho_2(phsq)_4(tppo)_2(NO_3)_2]$ (8-Ho)

Amount of $Ho(NO_3)_3{\cdot}6H_2O$ used = 160.67 mg. IR (4000-400 cm^{-1}): 3064 (w), 2091 (b,w), 1601 (m), 1577 (w), 1566 (s), 1520 (s), 1472 (m), 1457 (m), 1438 (m), 1370 (w), 1369 (w), 1348 (m), 1333 (w), 1311 (m), 1280 (w), 1274 (w), 1225 (m), 1166 (w), 1118 (m,b), 1106(m), 1095(m), 1077(m), 1040(m), 1025(s), 996(m), 977(m), 950 (w), 933 (s), 863(w), 849 (m), 816 (m), 778 (w), 768 (w), 755 (s), 741(w), 714(w), 692 (m), 682 (m), 668 (w), 628 (w,b), 574 (s), 494 (s), 435 (s), 414 (w).

$[Er_2(phsq)_4(tppo)_2(NO_3)_2]$ (9-Er)

Amount of $Er(NO_3)_3{\cdot}6H_2O$ used = 161.49 mg. IR (4000-400 cm^{-1}): 3063 (w), 2094 (b,w), 1603 (m), 1577 (w), 1566 (s), 1522 (s), 1473 (m), 1457 (m), 1438 (m), 1370 (w), 1369 (w), 1348 (m), 1331 (w), 1311 (m), 1282 (w), 1272 (w), 1225 (m), 1164 (w), 1116 (m,b), 1104(m), 1097 (m), 1077(m), 1040(m), 1025(s), 996(m), 975(m), 953 (w), 931 (s), 865(w), 847 (m), 814 (m), 778 (w), 768 (w), 755 (s), 741(w), 716(w), 692 (m), 682 (m), 668 (w), 628 (w,b), 574 (s), 490 (s), 434 (s), 413 (w).

$[Tm_2(phsq)_4(tppo)_2(NO_3)_2]$ (10-Tm)

Amount of $Tm(NO_3)_3{\cdot}6H_2O$ used = 162.07 mg. IR (4000-400 cm^{-1}): 3063 (w), 2092 (b,w), 1601 (m), 1577 (w), 1565 (s), 1521 (s), 1472 (m), 1457 (m), 1438 (m), 1370 (w), 1363 (w), 1348 (m), 1331 (w), 1311 (m), 1282 (w), 1274 (w), 1225 (m), 1165 (w), 1116 (m,b), 1104(m), 1095(m), 1077(m), 1040(m), 1025(s), 996(m), 975(m), 950 (w), 931 (s), 863(w), 849 (m), 814 (m), 770 (w), 755 (s), 741(w), 717(w), 692 (m), 682 (m), 668 (w), 628 (w,b), 574 (s), 494 (s), 432 (s), 414 (w).

$[Yb_2(phsq)_4(tppo)_2(NO_3)_2]$ (11-Yb)

Amount of $Yb(NO_3)_3{\cdot}6H_2O$ used = 163.51 mg. IR (4000-400 cm^{-1}): 3064 (w), 2090 (b,w), 1601 (m), 1577 (w), 1565 (s), 1520 (s), 1473 (m), 1457 (m), 1438 (m), 1370 (w), 1369 (w), 1351 (m), 1334 (w), 1311 (m), 1282 (w), 1272 (w), 1230 (m), 1166 (w), 1116 (m,b), 1104(m), 1094(m), 1079 (m), 1043(m), 1021(s), 996(m), 976(m), 952 (w), 931 (s), 863(w), 849 (m), 816 (m), 778 (w), 768 (w), 755 (s), 741(w), 717(w), 692 (m), 682 (m), 669 (w), 626 (w,b), 574 (s), 494 (s), 432 (s), 414 (w).

$[Lu_2(phsq)_4(tppo)_2(NO_3)_2]$ (12-Lu)

Amount of $Lu(NO_3)_3{\cdot}6H_2O$ used = 164.19 mg. IR (4000-400 cm^{-1}): 3059 (w), 2089 (b,w), 1603 (m), 1577 (w), 1565 (s), 1520 (s), 1469 (m), 1457 (m), 1438 (m), 1370 (w), 1369 (w), 1348 (m), 1329 (w), 1311 (m), 1282 (w), 1268 (w), 1230 (m), 1165 (w), 1116 (m,b), 1103(m), 1094(m), 1077(m), 1040(m), 1025(s), 996(m), 975(m), 950 (w), 931 (s), 863(w), 853 (m), 817 (m), 778 (w), 763 (w), 755 (s), 741(w), 720 (w), 692 (m), 682 (m), 669 (w), 628 (w,b), 574 (s), 494 (s), 432 (s), 413 (w).

$[Dy_xY_{(1-x)}(phsq)_4(tppo)_2(NO_3)_2]$ (13-YDy)

Amount of $Dy(NO_3)_3{\cdot}6H_2O$ used = 15.98 mg (0.035 mmol;10 %) and $Dy(NO_3)_3{\cdot}6H_2O$ used = 15.98 mg (0.035 mmol;90 %); $Y(NO_3)_3{\cdot}6H_2O$ (0.315

mmol) used = 82.30 mg.); $Y(NO_3)_3\cdot 6H_2O$ (0.315 mmol) used = 82.30 mg. IR (4000-400 cm^{-1}): 3061 (w), 2092 (b,w), 1601 (m), 1577 (w), 1565 (s), 1520 (s), 1472 (m), 1457 (m), 1438 (m), 1365 (w), 1348 (m), 1329 (w), 1311 (m), 1282 (w), 1275 (w), 1227 (m), 1166 (w), 1116 (m,b), 1103(m), 1094(m), 1077(m), 1040(m), 1025(s), 996(m), 975(m), 952 (w), 932 (s), 863(w), 849 (m), 815 (m), 778 (w), 768 (w), 755 (s), 744 (w), 718(w), 692 (m), 685 (m), 665 (w), 628 (w,b), 573 (s), 491 (s), 432 (s), 412 (w).

5.2.2 $[Dy_2(phsq)_4(tcypo)_2(NO_3)_2]$ (14-Dy)

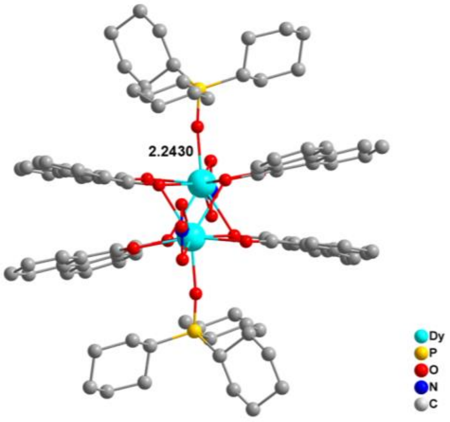

A Teflon insert was loaded with 9,10-phenanthrenequinone (70.0 mg, 0.35 mmol, 1.0 eq.), $Dy(NO_3)_3\cdot 6H2O$ (0.35 mmol, 159.82 g/mol, 1.0 eq.), Tricyclohexylphosphine oxide (0.35 mmol 1.0 eq.) and 10 ml MeOH. The vessel was closed with a lid and put into a steel autoclave that was sealed tightly and put in an oven at 90 °C for 1 week. The autoclave was cooled down to room temperature slowly by turning off the oven but leaving the oven door shut. After 24 h the autoclave was removed from the oven, opened and the contents were filtered. The product was obtained as dark crystals, after washing with methanol several times, the product was dried in air.

5.2.3 The synthesis of pyrene-4,5-dione

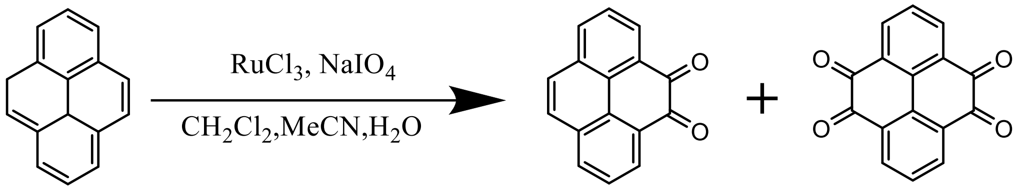

pyrene **pyrene-4,5-dione** pyrene-4,5,9,10-tetraone

In a round bottom flask pyrene (10.0 g, 49.4 mmol, 1.00 equiv) and $RuCl_3 \cdot xH_2O$ (987 mg, 4.74 mmol,0.096 equiv) were dissolved in 200 mL of MeCN. $NaIO_4$ (42.3 g,198 mmol, 4.00 equiv) was dissolved in 250 mL of hot water and carefully added to the pyrene solution. Another 200 mL of CH_2Cl_2 were added and the reaction mixture was vigorously stirred for 18 h at room temperature. After filtration of the suspensionthrough Celite, the filtrate was extracted with CH_2Cl_2 (100mL) and the combined organic phases were washed with saturatedaqueous $Na_2S_2O_3$ and H_2O and then dried over Na_2SO_4. After removing the solvent under reduced pressure, the product was obtained as a dark brown crude residue, the obtained crude residue was purified by column chromatography (n-hexane/ethyl acetate = 4:1) to give the final product (1.4 g, 82%) as a brown powder. (7.56 g, 66 %). ^{1}H NMR (200 MHz, $CDCl_3$):d = 8.51 (dd, J = 7 Hz, J = 1 Hz, 2 H), 8.19 (dd, J = 8 Hz, J = 1 Hz, 2 H),7.87 (s, 2 H), 7.77 (t, J = 8 Hz, 2 H) ppm.

5.2.4 $[Ln_2(pysq)_4(tppo)_2(NO_3)_2]$ (Ln = Nd^{III}, Gd^{III}, Dy^{III}, Ho^{III}, Er^{III})

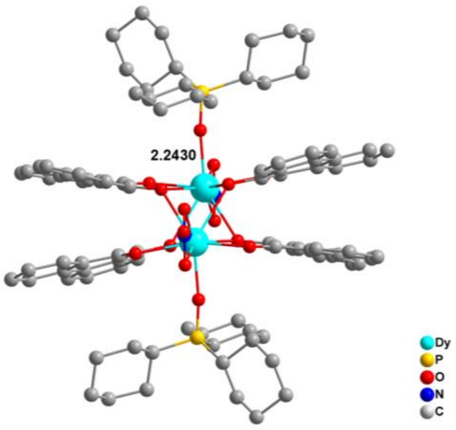

A Teflon insert was loaded with 9,10-phenanthrenequinone (70.0 mg, 0.35 mmol, 1.0 eq.), Ln(NO_3)$_3$·xH2O (0.35 mmol, 1.0 eq.), Triphenylphosphine oxide (0.35 mmol 1.0 eq.) and 10 ml MeOH. The vessel was closed with a lid and put into a steel autoclave that was sealed tightly and put in an oven at 90°C for 1 week. The autoclave was cooled down to room temperature slowly by turning off the oven but leaving the oven door shut. After 24 h the autoclave was removed from the oven, opened and the contents were filtered. The product was obtained as dark crystals, after washing with methanol several times, the product was dried in air.

[Nd_2(pysq)$_4$(tppo)$_2$(NO_3)$_2$] (15-Nd)

Amount of Nd(NO_3)$_3$·6H_2O used = 153.43 mg. IR (4000-400 cm^{-1}): 2947 (w), 2884 (w), 2173 (w), 2085 (w, b), 1718 (s), 1584 (m), 1551 (w), 1526 (s), 1491 (s), 1466 (m), 1435 (s), 1413 (s), 1376 (s), 1344 (s), 1258 (s), 1212 (m), 1156 (s), 1109 (w), 1088 (m), 1064 (m), 1025 (w), 1018 (s), 885 (s), 867 (w, b), 827 (m), 790 (w), 761 (m), 733 (s), 716 (w), 687 (m), 619 (m), 581 (m), 566 (m), 535 (m), 517 (s), 506 (s), 438 (s), 412(m).

[Gd_2(pysq)$_4$(tppo)$_2$(NO_3)$_2$] (16-Ho)

Amount of Gd(NO_3)$_3$·6H_2O used = 158.0 mg. IR (4000-400 cm^{-1}): 2945 (w), 2883 (w), 2177 (w), 2088 (w, b), 1715 (s), 1586 (m), 1526 (s), 1489 (s), 1467 (m), 1435 (s), 1413 (s), 1377 (s), 1344 (s), 1260 (s), 1214 (m), 1156 (s), 1109 (w), 1088 (m), 1066 (m), 1057 (w), 1026 (w), 1013 (s), 889 (s), 864 (w, b), 826 (m), 789 (w), 763 (m), 731 (s), 719 (w), 684 (m), 619 (m), 579 (m), 561 (m), 535 (m), 517 (s), 504 (s), 438 (s), 413(m).

[Dy_2(pysq)$_4$(tppo)$_2$(NO_3)$_2$] (17-Dy)

Amount of $Dy(NO_3)_3 \cdot 6H_2O$ used = 159.82 mg. IR (4000-400 cm^{-1}): 2944 (w), 2886 (w), 2171 (w), 2088 (w, b), 1715 (s), 1586 (m), 1551 (w), 1527 (s), 1491 (s), 1466 (m), 1435 (s), 1413 (s), 1376 (s), 1344 (s), 1258 (s), 1212 (m), 1156 (s), 1109 (w), 1088 (m), 1064 (m), 1055 (w), 1026 (w), 1011 (s), 889 (s), 864 (w, b), 826 (m), 789 (w), 760 (m), 731 (s), 717 (w), 687 (m), 619 (m), 582 (m), 561 (m), 535 (m), 517 (s), 506 (s), 438 (s), 411(m).

[Ho_2(pysq)$_4$(tppo)$_2$(NO_3)$_2$] (18-Ho)

Amount of $Ho(NO_3)_3 \cdot 6H_2O$ used = 160.67 mg. IR (4000-400 cm^{-1}): 2941 (w), 2889 (w), 2174 (w), 2086 (w, b), 1715 (s), 1584 (m), 1551 (w), 1527 (s), 1491 (s), 1466 (m), 1435 (s), 1412 (s), 1376 (s), 1346 (s), 1258 (s), 1209 (m), 1156 (s), 1109 (w), 1085 (m), 1064 (m), 1055 (w), 1026 (w), 1011 (s), 889 (s), 864 (w, b), 826 (m), 763 (m), 729 (s), 717 (w), 687 (m), 618 (m), 581 (m), 561 (m), 535 (m), 514 (s), 505 (s), 436 (s), 415(m).

[Er_2(pysq)$_4$(tppo)$_2$(NO_3)$_2$] (19-Yb)

Amount of $Er(NO_3)_3 \cdot 6H_2O$ used = 161.49 mg. IR (4000-400 cm^{-1}): 2944 (w), 2886 (w), 2174 (w), 2088 (w, b), 1719 (s), 1586 (m), 1551 (w), 1527 (s), 1491 (s), 1466 (m), 1435 (s), 1412 (s), 1375 (s), 1344 (s), 1258 (s), 1212 (m), 1156 (s), 1109 (w), 1088 (m), 1063 (m), 1055 (w), 1026 (w), 1010 (s), 891 (s), 864 (w, b), 826 (m), 789 (w), 763 (m), 731 (s), 720 (w), 686 (m), 619 (m), 582 (m), 561 (m), 537 (m), 517 (s), 508 (s), 438 (s), 410(m).

$[Dy_xY_{(1-x)}(pysq)_4(tppo)_2(NO_3)_2]$ (20-YDy)

Amount of $Dy(NO_3)_3·6H_2O$ used = 15.98 mg (0.035 mmol); $Y(NO_3)_3·6H_2O$ (0.315 mmol) used = 82.30 mg. IR (4000-400 cm^{-1}): 2944 (w), 2886 (w), 2174 (w), 2088 (w, b), 1717 (s), 1586 (m), 1548 (w), 1527 (s), 1489 (s), 1466 (m), 1435 (s), 1410 (s), 1376 (s), 1344 (s), 1258 (s), 1212 (m), 1156 (s), 1109 (w), 1088 (m), 1064 (m), 1053 (w), 1028 (w), 1013 (s), 886 (s), 861 (w, b), 830 (m), 789 (w), 760 (m), 731 (s), 717 (w), 687 (m), 619 (m), 582 (m), 561 (m), 535 (m), 517 (s), 506 (s), 438 (s), 413(m).

5.2.5 $[Dy_2(pysq)_4(tcypo)_2(NO_3)_2]$

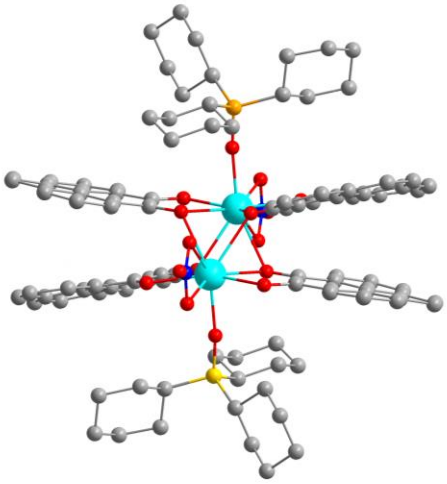

A Teflon insert was loaded with 9,10-phenanthrenequinone (70.0 mg, 0.35 mmol, 1.0 eq.), $Dy(NO_3)_3·6H_2O$ (0.35 mmol, 159.82 mg, 1.0 eq.), Tricyclohexylphosphine oxide (0.35 mmol 1.0 eq.) and 10 ml MeOH. The vessel was closed with a lid and put into a steel autoclave that was sealed tightly and put in an oven at 90°C for 1 week. The autoclave was cooled down to room temperature slowly by turning off the oven but leaving the oven door shut. After 24 h the autoclave was removed from the oven, opened and the contents were filtered. The product was obtained as dark crystals, after washing with methanol several times, the product was dried in air. IR (4000-400 cm^{-1}): 2944 (w), 2889 (w), 2173 (w), 2090 (w, b), 1717(s), 1585 (m), 1529 (s), 1491 (s), 1466 (m), 1435 (s), 1413 (s), 1376 (s), 1344 (s), 1258 (s), 1212 (m), 1153 (s), 1109 (w), 1088 (m), 1064 (m), 1055 (w), 1026 (w), 1011 (s), 889 (s), 864 (w, b), 826 (m), 760 (m), 731 (s), 720 (w), 687 (m), 621 (m), 582 (m), 561 (m), 535 (m), 517 (s), 506 (s), 440 (s), 414(m).

5.2.6 The synthesis of 1,4,7,10-Tetraazacyclododecane-1,4,7,10-tetraacetic acid

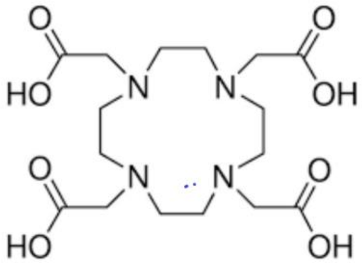

Chloroacetic acid (0.4mmol) was dissolved in 10ml of distilled water and stirred at 0 °C, while adjusting the pH to 4. Then 0.1mmol of cyclen was dissolved in 5 ml of distilled water, and the above solutions were mixed at 0 °C, and then placed at 80 °C for reaction. During the reaction, the pH was adjusted to 8, and the pH was maintained at 8 until the pH did not change (the reaction time was about 4 hours. Then it was cooled to room temperature, and then the pH was adjusted to 2 with hydrochloric acid. The solution changed from clear to turbid, and then filtered and placed in a 60°C oven overnight, and finally a white powder was obtained.

5.2.7 [Zn(H_2DOTA)$_2$] (21-Zn)

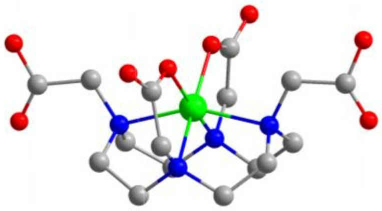

A mixture of ZnCl2 (0.5 mmol), H_4DOTA (0.5 mmol) in 10 mL of distilled water was heated for 6 h at 80°C until obtaining a clear solution. After reaction, the mixture was cooled to room temperature, filtrated to remove the residual suspension. The crystal were obtained by a vapor diffusion method from a water and acetone solution at room temperature.

5.2.8 [$Dy_2Zn_2(DOTA)_2 10H_2O$• ($ZnCl_4$)] (22-Zn_2Dy_2)

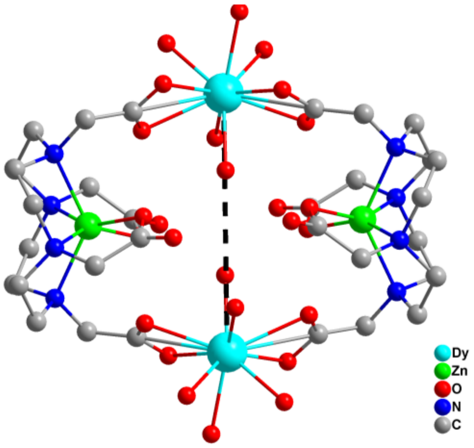

A mixture of $ZnCl_2·6H_2O$ (0.5 mmol), H_4DOTA (0.5 mmol) and NaOH (0.5 mmol) in 10 mL of distilled water was heated for 6h at 80°C until obtaining a clear solution. Then add Dy_2O_3 (0.25 mmol) to the above solution and add 0.5 mmol NaOH at the same time (the pH is controlled at about 4), the mixture was cooled to room temperature, filtrated to remove the residual suspension. The crystal were obtained by a vapor diffusion method from a water and acetone solution at room temperature. After four days, colorless and transparent block crystals were obtained. IR (4000-400 cm^{-1}): 3372 (b,s), 2984 (m), 2921 (w,b), 2877 (m), 1655 (w), 1636 (m), 1591 (s), 1434 (m), 1401 (s), 1315 (s), 1282 (s), 1246 (s), 1166 (m), 1086 (s), 1003 (s), 983 (s), 939 (s), 912 (m), 886 (m), 845 (s), 801 (m), 787 (w), 718 (s), 641 (m), 621 (w), 585 (w), 552 (w), 519 (w), 500 (m), 453 (s), 436 (w), 422 (w), 409 (w). Element analysis : C/H/N (calculated): C: 23.27 %, H: 4.64 %, N: 6.78 %. C/H/N (found): C: 23.65 %, H: 4.57 %, N: 6.81 %.

5.2.9 $Dy_4Zn_4(DOTA)_416H_2O$ • Cl_4 (23-Zn_4Dy_4)

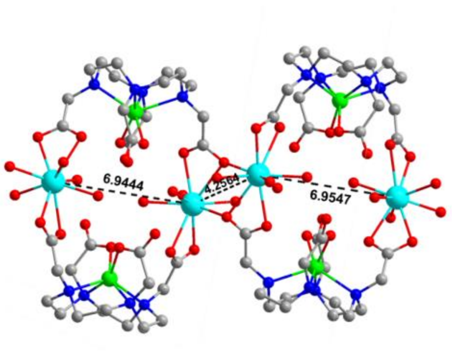

A mixture of $ZnCl_2·6H_2O$ (0.5 mmol), H_4DOTA (0.5 mmol) and NaOH (0.5 mmol) in 10 mL of distilled water was heated for 6h at 80°C, then add Dy_2O_3 (0.25 mmol) to the above solution and add 0.5 mmol NaOH at the same time (the pH is controlled at about 4), and continue to react at 80 degrees Celsius for about three days. After the reaction is completed, the mixture was cooled to room temperature, using NaOH solution to adjust the PH to about 7, and filtrated to remove the residual suspension. The crystal were obtained by a vapor diffusion method from a water and acetone solution at room temperature. After four days, colorless and transparent block crystals were obtained. IR (4000-400 cm^{-1}): 3386 (b,s), 2972 (m), 2945 (w), 2868(m), 1653 (w), 1612 (m), 1587 (s), 1445 (m), 1412 (s), 1386 (s), 1279 (s), 1244 (s), 1187 (m), 1106 (s), 997 (s), 985 (s), 940 (s), 925 (m), 898 (m), 887 (s), 834 (m), 792(w), 756 (s), 654 (m), 631(w), 611 (w), 594 (w), 562 (w), 516 (w), 497 (m), 475 (s), 457 (w), 434 (w), 421 (w).

5.2.10 The synthesis of *N,N,N',N'*-Tetrakis[(6-carboxymethylpyridin-2-yl)methyl]ethyl-ene diamine

5.2.10.1 Dimethyl pyridine-2,6-dicarboxylate

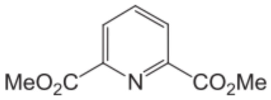

2,6- pyridine dicarboxylic acid (5.2 g, 0.031 mol) and sulfuric acid (0.9 mL) were stirred in refluxing methanol (20 mL) for 16 h. After reaction completion (followed by TLC), methanol was concentrated. The residue was diluted in dichloromethane and then washed with saturated $NaHCO_3$ then water. The combined organic layers were dried over Na2SO4 and then the solvent was removed under re duced pressure to afford the desired ester 1 (5.4 g, 90%) as a white solid.

5.2.10.2 Methyl (6-hydroxymethyl)-pyridine-2-carboxylate

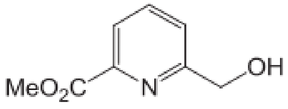

$NaBH_4$ (390 mg,10.3 mmol) was slowly added, at 0 °C, to a solution of dimethyl pyridine-2,6-dicarboxylate (2.00 g, 10.2 mmol) in dry MeOH (100 mL). The red reaction mixture was stirred red for 12 h at room temperature and then neutralized with an aqueous saturated NH_4Cl solution. After extraction with CH_2Cl_2 (350 mL), the combined organic layers were dried with Na_2SO_4 and the solvent was removed under reduced pressure. The resulting crude residue was purified by column chromatography (dichloromethane) giving the mono-alcohol 3 (1.4 g, 82%) as a white solid.

5.2.10.3 Methyl (6-chloromethyl)-pyridine-2-carboxylate

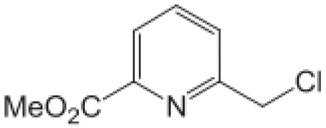

Thionyl chloride (5 mL) is slowly added to methyl 6 hydroxymethyl-2-pyridine carboxylate (2.5 g, 14.9 mmol) at 0 °C, under nitrogen and stirred for 1 h. The reaction mixture is concentrated under vacuum. The obtained residue was diluted in toluene and washed with saturated sodium bicarbonate solution. The aqueous solution was extracted three times by toluene. The combined organic layers were dried on Na_2SO_4, filtered and concentrated by evaporation in a vacuum. The chloride compound was obtained as a yellowish solid (2.48 g, 90%) and used without further purification.

5.2.10.4 *N,N,N',N'*-Tetrakis[(6-carboxymethylpyridin-2-yl)methyl]ethyl-ene diamine

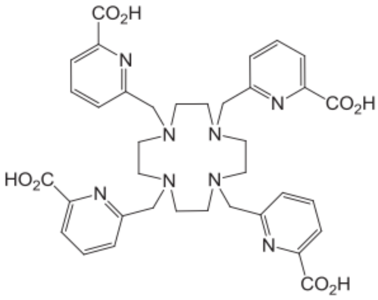

Methyl 6-chloromethyl-2-pyridine carboxylate 3 (500 mg, 2.7 mmol) and K_2CO_3 (391 mg, 2.8 mmol) followed by freshly dis tilled acetonitrile (10 mL) were added to a Schlenk flask under ar gon atmosphere. Ethylene diamine (45 mL, 0.67 mmol) was then added. The mixture was stirred at 80 C for 12 h. Acetonitrile was then removed under vacuum. The obtained residue was diluted with dichloromethane and washed with water. The organic layers were dried on Na_2SO_4, filtered and concentrated under vacuum. The resulting residue was recrystallized in *i*-PrOH to afford a slightly yellow powder (314 mg, 70%). The above product was mixed in HCl 6 M (2 mL) at 100 C for 12 h. The suspension was filtered and washed with cold water. H_4tpaen was obtained as a white powder.

5.2.11 [Zn(H_3tapen)Cl] (24-Zn)

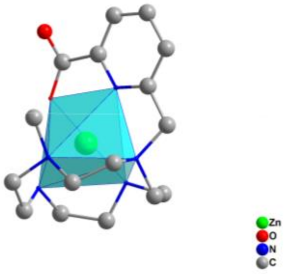

A solution of $ZnCl_2 \cdot 6H2O$ (0.138 mmol) in H_2O (0.5 mL) was added to a solution of H_4tapen (0.138 mmol) in water (6 mL) at pH 5, adjusted by the addition of KOH (0.2m). The resulting solution was then stirred at room temperature for 2 h and its pH value was readjusted to 6 by the addition of further KOH (0.2 M). The water was then evaporated and the resulting solid was suspended in EtOH (5 mL).

The insoluble salts were removed by filtration and the filtrate was evaporated. The resulting solid was suspended in H_2O, and vapor diffusion-grow crystals in acetone. Finally, yellow block crystals were obtained after three days.

5.2.12 [Dy(H_2tapen)Cl] (25-Dy)

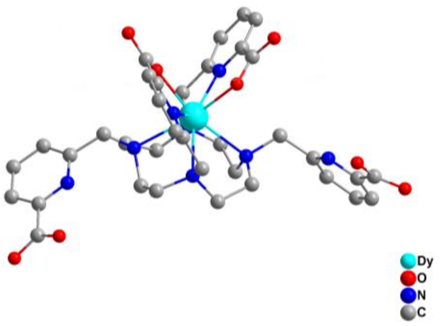

A solution of DyCl3·6H2O (0.138 mmol) in H_2O (0.5 mL) was added to a solution of H_4tapen (0.138 mmol) in water (6 mL) at pH 5, adjusted by the addition of KOH (0.2m). The resulting solution was then stirred at room temperature for 2 h and its pH value was readjusted to 6 by the addition of further KOH (0.2 M). The water was then evaporated and the resulting solid was suspended in EtOH (5 mL). The insoluble salts were removed by filtration and the filtrate was evaporated. The resulting solid was suspended in H_2O, and vapor diffusion-grow crystals in acetone. Finally, yellow block crystals were obtained after three days. IR (4000-400 cm^{-1}): 3352 (b,s), 2945 (m), 2921 (w), 2888(m), 2563 (w), 2003 (m), 1887 (s), 1665 (m), 1542 (s), 1516 (s), 1479 (s), 1424 (s), 1327 (m), 1263 (w), 1221 (s), 1138 (s), 1085 (s), 945 (s), 935 (m), 901 (m), 897 (s), 854(w), 844 (m), 791(w), 746 (s), 683 (m), 645(w), 623 (w), 596 (w), 571 (w), 556 (w), 483 (m), 489 (s), 453 (w), 423 (w), 415 (w).

6. References

[1] N. J. N. Jones, *Nature* **2011**, *472*, 22-24.

[2] K. S. Murray, *Aust. J. Chem.* **2009**, *62*, 1081-1101.

[3] S. Thiele, F. Balestro, R. Ballou, S. Klyatskaya, M. Ruben, W. Wernsdorfer, *Science* **2014**, *344*, 1135-1138.

[4] O. Gutfleisch, M. A. Willard, E. Brück, C. H. Chen, S. Sankar, J. P. Liu, *Adv. Mater.* **2011**, *23*, 821-842.

[5] D. N. Woodruff, R. E. Winpenny, R. Layfield, *Chem. Rev.* **2013**, *113*, 5110-5148.

[6] L. Bogani, W. Wernsdorfer, *Nat. Mater.* **2008**, *7*, 179-186.

[7] M. N. Leuenberger, D. Loss, *Nature* **2001**, *410*, 789-793.

[8] A. R. Rocha, V. M. Garcia-Suarez, S. W. Bailey, C. J. Lambert, J. Ferrer, S. Sanvito, *Nat. Mater.* **2005**, *4*, 335-339.

[9] A. G. Martynov, Y. Horii, K. Katoh, Y. Bian, J. Jiang, M. Yamashita, Y. G. Gorbunova, *Chem. Soc. Rev.* **2022**, *51*, 9262-9339.

[10] S. Sanvito, *Chem. Soc. Rev* **2011**, *40*, 3336-3355.

[11] A. Cornia, P. Seneor, *Nat. Mater.* **2017**, *16*, 505-506.

[12] A. Gaita-Ariño, F. Luis, S. Hill, E. Coronado, *Nat. Chem.* **2019**, *11*, 301-309.

[13] E. Moreno-Pineda, W. Wernsdorfer, *Nat. Rev. Phys.* **2021**, *3*, 645-659.

[14] R. Sessoli, A. K. Powell, *Coord. Chem. Rev* **2009**, *253*, 2328-2341.

[15] L. Thomas, F. Lionti, R. Ballou, D. Gatteschi, R. Sessoli, B. Barbara, *Nature* **1996**, *383*, 145-147.

[16] M. Shiddiq, D. Komijani, Y. Duan, A. Gaita-Ariño, E. Coronado, S. Hill, *Nature* **2016**, *531*, 348-351.

[17] S. T. Liddle, J. van Slageren, *Chem. Soc. Rev.* **2015**, *44*, 6655-6669.

[18] R. Sessoli, *Nature* **2017**, *543*, 189-190.

[19] K. S. Pedersen, J. Bendix, R. Clérac, *Chem. Commun.* **2014**, *50*, 4396-4415.

[20] J. Emerson-King, G. K. Gransbury, B. E. Atkinson, W. J. Blackmore, G. F. Whitehead, N. F. Chilton, D. P. Mills, *Nature* **2025**, *643*, 1-5.

[21] T. G. Ashebr, H. Li, X. Ying, X.-L. Li, C. Zhao, S. Liu, J. Tang, *ACS Materials Lett.* **2022**, *4*, 307-319.

[22] X. Feng, Y. Shang, H. Zhang, R. Li, W. Wang, D. Zhang, L. Wang, Z. Li, *RSC Adv.* **2019**, *9*,

16328-16338.

[23] M. Skwierczyńska, M. Runowski, S. Goderski, J. Szczytko, J. Rybusiński, P. Kulpiński, S. Lis, *ACS Omega* **2018**, *3*, 10383-10390.

[24] G. Rogez, B. Donnio, E. Terazzi, J. L. Gallani, J. P. Kappler, J. P. Bucher, M. Drillon, *Adv. Mat.* **2009**, *21*, 4323-4333.

[25] C. A. Mattei, T. Delouche, B. Lefeuvre, M. Cordier, C. Lalli, O. Cador, L. A. Galán, F. Riobé, O. Maury, P.-A. Bouit, *Chem. Squared* **2022**, *6*, 1.

[26] D. E. Freedman, W. H. Harman, T. D. Harris, G. J. Long, C. J. Chang, J. R. Long, *J. Am. Chem. Soc.* **2010**, *132*, 1224-1225.

[27] R. Sessoli, A. K. Powell, *Coord. Chem. Rev.* **2009**, *253*, 2328-2341.

[28] D. Shao, X. Y. Wang, *Chinese Journal of Chemistry* **2020**, *38*, 1005-1018.

[29] D. N. Woodruff, R. E. Winpenny, R. Layfield, *Chem. Rev.* **2013**, *113*, 5110-5148.

[30] A. Cornia, M. Mannini, P. Sainctavit, R. Sessoli, *Chem. Soc. Rev.* **2011**, *40*, 3076-3091.

[31] T. Han, Y.-S. Ding, Y.-Z. Zheng, *Recent development in clusters of rare earths and actinides: chemistry and materials* **2016**, 209-314.

[32] A. K. Boudalis, Y. Sanakis, J. M. Clemente-Juan, B. Donnadieu, V. Nastopoulos, A. Mari, Y. Coppel, J. P. Tuchagues, S. P. J. C. A. E. J. Perlepes, **2008**, *14*, 2514-2526.

[33] J. Lu, M. Guo, J. Tang, *Chem. Asian J.* **2017**, *12*, 2772-2779.

[34] J. P. Durrant, B. M. Day, J. Tang, A. Mansikkamäki, R. A. Layfield, *Angew. Chem., Int. Ed.* **2022**, *61*, e202200525.

[35] N. F. Chilton, D. Collison, E. J. McInnes, R. E. Winpenny, A. Soncini, *Nat. Commun.* **2013**, *4*, 2551.

[36] S. Demir, I.-R. Jeon, J. R. Long, T. D. Harris, *Coord. Chem. Rev.* **2015**, *289*, 149-176.

[37] N. F. J. I. c. Chilton, *Inorg. Chem.* **2015**, *54*, 2097-2099.

[38] M. Urdampilleta, S. Klyatskaya, J.-P. Cleuziou, M. Ruben, W. Wernsdorfer, *Nat. Mater.* **2011**, *10*, 502-506.

[39] E. Moreno-Pineda, C. Godfrin, F. Balestro, W. Wernsdorfer, M. Ruben, *Chem. Soc. Rev.* **2018**, *47*, 501-513.

[40] G. Aromí, D. Aguilà, P. Gamez, F. Luis, O. Roubeau, *Chem. Soc. Rev.* **2012**, *41*, 537-546.

[41] A. Cornia, M. Mannini, P. Sainctavit, R. Sessoli, *Chem. Soc. Rev.,* **2011**, *40*, 3076-3091.

[42] J.-L. Liu, Y.-C. Chen, M.-L. Tong, *Chem. Soc. Rev.* **2018**, *47*, 2431-2453.

[43] A. Castro-Alvarez, Y. Gil, L. Llanos, D. Aravena, *Inorg. Chem. Front.* **2020**, *7*, 2478-2486.

[44] A. Lunghi, F. Totti, S. Sanvito, R. Sessoli, *Sci. Chem.* **2017**, *8*, 6051-6059.

[45] J. G. Kragskow, A. Mattioni, J. K. Staab, D. Reta, J. M. Skelton, N. F. Chilton, *Chem. Soc. Rev.* **2023**, *52*, 4567-4585.

[46] H.-D. Li, S.-G. Wu, M.-L. Tong, *Chem. Commun.* **2023**, *59*, 6159-6170.

[47] R. Sessoli, H. L. Tsai, A. R. Schake, S. Wang, J. B. Vincent, K. Folting, D. Gatteschi, G. Christou, D. N. Hendrickson, *J. Am. Chem. Soc.* **1993**, *115*, 1804-1816.

[48] T. Lis, *Structural Science* **1980**, *36*, 2042-2046.

[49] H. M. Xiao, L. C. Shi, *Advanced Materials Research,* **2012**, *485*, 522-525.

[50] A. M. Ako, I. J. Hewitt, V. Mereacre, R. Clérac, W. Wernsdorfer, C. E. Anson, A. K. Powell, *Angew. Chem. Int. Ed.* **2006**, *118*, 5048-5051.

[51] M. Murugesu, M. Habrych, W. Wernsdorfer, K. A. Abboud, G. Christou, *J. Am. Chem. Soc.* **2004**, *126*, 4766-4767.

[52] P. Abbasi, K. Quinn, D. I. Alexandropoulos, M. Damjanovic, W. Wernsdorfer, A. Escuer, J. Mayans, M. Pilkington, T. C. Stamatatos, *J. Am. Chem. Soc.* **2017**, *139*, 15644-15647.

[53] A. J. Tasiopoulos, A. Vinslava, W. Wernsdorfer, K. A. Abboud, G. Christou, *Angew. Chem. Int. Ed.* **2004**, *43*.

[54] A. Caneschi, D. Gatteschi, N. Lalioti, C. Sangregorio, R. Sessoli, G. Venturi, A. Vindigni, A. Rettori, M. G. Pini, M. A. Novak, *Angew. Chem. Int. Ed.* **2001**, *40*, 1760-1763.

[55] L. Ungur, L. F. Chibotaru, *Phys. Chem. Chem. Phys.* **2011**, *13*, 20086-20090.

[56] V. Chandrasekhar, S. Das, A. Dey, S. Hossain, J.-P. Sutter, *Inorg. Chem.* **2013**, *52*, 11956-11965.

[57] M. Gregson, N. F. Chilton, A.-M. Ariciu, F. Tuna, I. F. Crowe, W. Lewis, A. J. Blake, D. Collison, E. J. McInnes, R. E. Winpenny, *Chem. Sci.* **2016**, *7*, 155-165.

[58] J. Luzon, R. Sessoli, *Dalton Trans.* **2012**, *41*, 13556-13567.

[59] G. Huang, C. Daiguebonne, G. Calvez, Y. Suffren, O. Guillou, T. Guizouarn, B. Le Guennic, O. Cador, K. Bernot, *Inorg. Chem.* **2018**, *57*, 11044-11057.

[60] C. A. Gould, K. R. McClain, D. Reta, J. G. Kragskow, D. A. Marchiori, E. Lachman, E.-S. Choi, J. G. Analytis, R. D. Britt, N. Chilton, *Science* **2022**, *375*, 198-202.

[61] L. Ungur, L. F. Chibotaru, *Inorg. Chem.* **2016**, *55*, 10043-10056.

[62] A. G. Bispo-Jr, *Coord. Chem. Rev* **2025**, *537*, 216685.

[63] A. Swain, T. Sharma, G. Rajaraman, *Chem. Commun.* **2023**, *59*, 3206-3228.

[64] M. Affronte, F. Troiani, A. Ghirri, A. Candini, M. Evangelisti, V. Corradini, S. Carretta, P. Santini, G. Amoretti, F. Tuna, *J. Phys. D: Appl. Phys.* **2007**, *40*, 2999.

[65] F.-S. Guo, A. K. Bar, R. A. Layfield, *Chem. Rev.* **2019**, *119*, 8479-8505.

[66] Z. Zhu, J. Tang, *Chem. Soc. Rev.* **2022**, *51*, 9469-9481.

[67] M. Briganti, F. Santanni, L. Tesi, F. Totti, R. Sessoli, A. Lunghi, *J. Am. Chem.Soc.* **2021**, *143*, 13633-13645.

[68] F. Liu, L. Spree, D. S. Krylov, G. Velkos, S. M. Avdoshenko, A. A. Popov, *Acc. Chem. Res.* **2019**, *52*, 2981-2993.

[69] P. Evans, D. Reta, G. F. Whitehead, N. F. Chilton, D. P. Mills, *J. Am. Chem. Soc.* **2019**, *141*, 19935-19940.

[70] S. D. Jiang, B. W. Wang, G. Su, Z. M. Wang, S. Gao, *Angew. Chem. Int. Ed.* **2010**, *122*, 7610-7613.

[71] T. Jurca, A. Farghal, P.-H. Lin, I. Korobkov, M. Murugesu, D. S. Richeson, *J. Am. Chem. Soc.* **2011**, *133*, 15814-15817.

[72] Y. S. Ding, N. F. Chilton, R. E. Winpenny, Y. Z. Zheng, *Angew. Chem. Int. Ed.* **2016**, *55*, 16071-16074.

[73] A. Dey, P. Kalita, V. Chandrasekhar, *ACS omega* **2018**, *3*, 9462-9475.

[74] Y.-S. Meng, S.-D. Jiang, B.-W. Wang, S. Gao, *Acc. Chem. Res.* **2016**, *49*, 2381-2389.

[75] P. Zhang, L. Zhang, C. Wang, S. Xue, S.-Y. Lin, J. Tang, *J. Am. Chem. Soc.* **2014**, *136*, 4484-4487.

[76] S. K. Gupta, R. Murugavel, *Chem. Commun.* **2018**, *54*, 3685-3696.

[77] K. R. Meihaus, M. E. Fieser, J. F. Corbey, W. J. Evans, J. R. Long, *J. Am. Chem. Soc.* **2015**, *137*, 9855-9860.

[78] Y. S. Meng, L. Xu, J. Xiong, Q. Yuan, T. Liu, B. W. Wang, S. Gao, *Angew. Chem. Int. Ed.* **2018**, *130*, 4763-4766.

[79] B. M. Day, F.-S. Guo, R. A. Layfield, *Acc. Chem. Res.* **2018**, *51*, 1880-1889.

[80] M. Jeletic, P.-H. Lin, J. J. Le Roy, I. Korobkov, S. I. Gorelsky, M. Murugesu, *J. Am. Chem. Soc.* **2011**, *133*, 19286-19289.

[81] L. Ruan, J. Tong, G. Qin, L. Zhou, X. Jiao, X. Zhang, *Eur. J. Inorg. Chem.* **2020**, *2020*, 2112-2117.

[82] S. Sakaue, A. Fuyuhiro, T. Fukuda, N. Ishikawa, *Chem. Commun.* **2012**, *48*, 5337-5339.

[83] A. L. Wysocki, K. Park, *Inorg. Chem.* **2020**, *59*, 2771-2780.

[84] G. Mattioli, F. Filippone, A. A. Bonapasta, *J. Phys. Chem. Lett.* **2010**, *1*, 2757-2762.

[85] N. Ishikawa, M. Sugita, T. Ishikawa, S.-y. Koshihara, Y. Kaizu, *J. Am. Chem. Soc.* **2003**, *125*, 8694-8695.

[86] R. Layfield, J. McDouall, S. Sulway, F. Tuna, D. Collison, R. Winpenny, *Chemistry* **2010**, *16*, 4442-4446.

[87] Y.-C. Chen, J.-L. Liu, L. Ungur, J. Liu, Q.-W. Li, L.-F. Wang, Z.-P. Ni, L. F. Chibotaru, X.-M. Chen, M.-L. Tong, *J. Am. Chem. Soc.* **2016**, *138*, 2829-2837.

[88] Z. Zhu, C. Zhao, T. Feng, X. Liu, X. Ying, X.-L. Li, Y.-Q. Zhang, J. Tang, *J. Am. Chem. Soc.* **2021**, *143*, 10077-10082.

[89] C. A. Goodwin, F. Ortu, D. Reta, N. F. Chilton, D. P. Mills, *Nature* **2017**, *548*, 439-442.

[90] F.-S. Guo, B. M. Day, Y.-C. Chen, M.-L. Tong, A. Mansikkamäki, R. A. Layfield, *Science* **2018**, *362*, 1400-1403.

[91] M. Guo, Y. Xu, J. Wu, L. Zhao, J. Tang, *Dalton Trans.* **2017**, *46*, 8252-8258.

[92] F. Pointillart, Y. Le Gal, S. Golhen, O. Cador, L. Ouahab, *Chem. - Eur. J.* **2011**, *17*, 10397-10404.

[93] M. Perfetti, M. Gysler, Y. Rechkemmer-Patalen, P. Zhang, H. Taştan, F. Fischer, J. Netz, W. Frey, L. W. Zimmermann, T. Schleid, *Chem. Commun.* **2019**, *10*, 2101-2110.

[94] K. Katoh, Y. Horii, N. Yasuda, W. Wernsdorfer, K. Toriumi, B. K. Breedlove, M. Yamashita, *Dalton Trans.* **2012**, *41*, 13582-13600.

[95] J.-Y. Ge, L. Cui, J. Li, F. Yu, Y. Song, Y.-Q. Zhang, J.-L. Zuo, M. Kurmoo, *Inorg. Chem.* **2017**, *56*, 336-343.

[96] J. Wu, S. Demeshko, S. Dechert, F. Meyer, *Dalton Trans.* **2021**, *50*, 17573-17582.

[97] K. L. Harriman, J. J. Le Roy, L. Ungur, R. J. Holmberg, I. Korobkov, M. Murugesu, *Chem. Sci.* **2017**, *8*, 231-240.

[98] T. Morita, M. Damjanovic, K. Katoh, Y. Kitagawa, N. Yasuda, Y. Lan, W. Wernsdorfer, B. K. Breedlove, M. Enders, M. Yamashita, *J. Am. Chem. Soc.* **2018**, *140*, 2995-3007.

[99] Y.-C. Chen, M.-L. Tong, *Chem. Sci.* **2022**, *13*, 8716-8726.

[100] J. Long, F. Habib, P.-H. Lin, I. Korobkov, G. Enright, L. Ungur, W. Wernsdorfer, L. F. Chibotaru, M. Murugesu, *J. Am. Chem. Soc.* **2011**, *133*, 5319-5328.

[101] Y.-N. Guo, G.-F. Xu, W. Wernsdorfer, L. Ungur, Y. Guo, J. Tang, H.-J. Zhang, L. F. Chibotaru, A. K. Powell, *J. Am. Chem. Soc.* **2011**, *133*, 11948-11951.

[102] J. D. Rinehart, M. Fang, W. J. Evans, J. R. Long, *Nat. Chem.* **2011**, *3*, 538-542.

[103] J. D. Rinehart, M. Fang, W. J. Evans, J. R. Long, *J. Am. Chem. Soc.* **2011**, *133*, 14236-14239.

[104] S. Demir, M. I. Gonzalez, L. E. Darago, W. J. Evans, J. R. Long, *Nat. Commun.* **2017**, *8*, 2144.

[105] S. Demir, J. M. Zadrozny, M. Nippe, J. Long, *J. Am. Chem. Soc.* **2012**, *134*, 18546-18549.

[106] J.-C. G. Bünzli, *Chem. Rev.* **2010**, *110*, 2729-2755.

[107] J.-C. G. Bünzli, *Coord. Chem. Rev.* **2015**, *293*, 19-47.

[108] F. Pointillart, B. Le Guennic, O. Cador, O. Maury, , *Acc. Chem. Res.* **2015**, *48*, 2834-2842.

[109] G. Wang, Q. Peng, Y. Li, *Acc. Chem. Res.* **2011**, *44*, 322-332.

[110] S.-L. Zuo, P. Chen, C.-F. Pan, *Rare Met.* **2020**, *39*, 1113-1126.

[111] O. Mrózek, M. Gernert, A. Belyaev, M. Mitra, L. Janiak, C. M. Marian, A. Steffen, *Chem. Eur. J.* **2022**, *28*, e202201114.

[112] X.-L. Li, C.-L. Chen, H.-P. Xiao, A.-L. Wang, C.-M. Liu, X. Zheng, L.-J. Gao, X.-G. Yang, S.-M. Fang, *Dalton Trans.* **2013**, *42*, 15317-15325.

[113] F. Ferrari, J. Braun, C. E. Anson, B. D. Wilts, D. Moatsou, C. Bizzarri, *Molecules* **2021**, *26*, 2567.

[114] S. Roy, A. Chakraborty, T. K. J. C. C. R. Maji, *Coord. Chem. Rev.* **2014**, *273*, 139-164.

[115] R. Jankowski, M. Wyczesany, S. Chorazy, *Chem. Commun.* **2023**, *59*, 5961-5986.

[116] R. Marin, G. Brunet, M. J. A. C. I. E. Murugesu, *Angew. Chem. Int. Ed.* **2021**, *60*, 1728-1746.

[117] J.-H. Jia, Q.-W. Li, Y.-C. Chen, J.-L. Liu, M.-L. Tong, *Coord. Chem. Rev* **2019**, *378*, 365-381.

[118] H.-Y. Wong, W. T. K. Chan, G.-L. J. I. c. Law, *Inorg. Chem.* **2018**, *57*, 6893-6902.

[119] D. Errulat, R. Marin, D. A. Galico, K. L. Harriman, A. Pialat, B. Gabidullin, F. Iikawa, O. D. Couto Jr, J. O. Moilanen, E. Hemmer, *ACS Cent. Sci.* **2019**, *5*, 1187-1198.

[120] Y.-J. Ma, J.-X. Hu, S.-D. Han, J. Pan, J.-H. Li, G.-M. Wang, *J. Am. Chem. Soc.* **2020**, *142*, 2682-2689.

[121] J. Ruiz, G. Lorusso, M. Evangelisti, E. K. Brechin, S. J. Pope, E. Colacio, *Inorg. Chem.* **2014**, *53*, 3586-3594.

[122] C. Wegeberg, O. S. J. J. A. Wenger, *J. Am. Chem. Soc. Au* **2021**, *1*, 1860-1876.

[123] Y. Kishi, L. Cornet, F. Pointillart, F. Riobé, B. Lefeuvre, O. Cador, B. Le Guennic, O. Maury, H. Fujiwara, L. Ouahab, *Eur. J. Inorg. Chem.* **2018**, *2018*, 458-468.

[124] F. Pointillart, B. Le Guennic, S. Golhen, O. Cador, O. Maury, L. Ouahab, *Chem. Commun.* **2013**, *49*, 615-617.

[125] M. Nie, J. Xiong, C. Zhao, H. Meng, K. Zhang, Y. Han, J. Li, B. Wang, L. Feng, C. Wang, *Nano Res.* **2019**, *12*, 1727-1731.

[126] G. Huang, G. Calvez, Y. Suffren, C. Daiguebonne, S. Freslon, O. Guillou, K. Bernot, *Magnetochemistry* **2018**, *4*, 44.

[127] D. A. Galico, R. Marin, G. Brunet, D. Errulat, E. Hemmer, F. A. Sigoli, J. O. Moilanen, M. Murugesu, *Chem. Eur. J.* **2019**, *25*, 14625-14637.

[128] J. Long, J. Rouquette, J. M. Thibaud, R. A. Ferreira, L. D. Carlos, B. Donnadieu, V. Vieru, L. F. Chibotaru, L. Konczewicz, J. Haines, *Angew. Chem. Int. Ed.* **2015**, *54*, 2236-2240.

[129] Y. Bi, C. Chen, Y.-F. Zhao, Y.-Q. Zhang, S.-D. Jiang, B.-W. Wang, J.-B. Han, J.-L. Sun, Z.-Q. Bian, Z.-M. Wang, *Chem. Sci.* **2016**, *7*, 5020-5031.

[130] J. Long, Y. Guari, R. A. Ferreira, L. D. Carlos, J. Larionova, *Coord. Chem. Rev.* **2018**, *363*, 57-70.

[131] D. Parker, E. A. Suturina, I. Kuprov, N. Chilton, *Acc. Chem. Res.* **2020**, *53*, 1520-1534.

[132] M. Feng, F. Pointillart, B. Le Guennic, B. Lefeuvre, S. Golhen, O. Cador, O. Maury, L. Ouahab, *Chem. - Asian J.* **2014**, *9*, 2814-2825.

[133] F. Pointillart, T. Cauchy, O. Maury, Y. Le Gal, S. Golhen, O. Cador, L. Ouahab, *Chem. - Eur. J.* **2010**, *16*, 11926-11941.

[134] W. Huang, D. Wu, D. Guo, X. Zhu, C. He, Q. Meng, C. Duan, *Dalton Trans.* **2009**, 2081-2084.

[135] R. F. Ziessel, G. Ulrich, L. Charbonnière, D. Imbert, R. Scopelliti, J. C. G. Bünzli, *Chem. - Eur. J.* **2006**, *12*, 5060-5067.

[136] F. Pointillart, A. Bourdolle, T. Cauchy, O. Maury, Y. Le Gal, S. Golhen, O. Cador, L. Ouahab, *Inorg. Chem.* **2012**, *51*, 978-984.

[137] N. S. Baek, Y. H. Kim, Y. K. Eom, J. H. Oh, H. K. Kim, A. Aebischer, F. Gumy, A.-S. Chauvin, J.-C. G. Bünzli, *Dalton Trans.* **2010**, *39*, 1532-1538.

[138] F. Pointillart, B. L. Guennic, O. Maury, S. Golhen, O. Cador, L. Ouahab, *Inorg. Chem.* **2013**, *52*, 1398-1408.

[139] F. Pointillart, O. Maury, Y. Le Gal, S. Golhen, O. Cador, L. Ouahab, *Inorg. Chem.* **2009**, *48*, 7421-7429.

[140] Y.-F. Ran, M. Steinmann, M. Sigrist, S.-X. Liu, J. Hauser, S. Decurtins, *C. R. Chim.* **2012**, *15*, 838-844.

[141] S. Faulkner, B. P. Burton-Pye, T. Khan, L. R. Martin, S. D. Wray, P. J. Skabara, *Chem. Commun.* **2002**, 1668-1669.

[142] D. Pinkowicz, M. Ren, L. M. Zheng, S. Sato, M. Hasegawa, M. Morimoto, M. Irie, B. K. Breedlove, G. Cosquer, K. Katoh, *chem.-Eur. J.* **2014**, *20*, 12502-12513.

[143] H. K. Bisoyi, Q. Li, *Chem. Rev.* **2016**, *116*, 15089-15166.

[144] J. Long, *Front. Chem.* **2019**, *7*, 63.

[145] J. J. Zakrzewski, S. Chorazy, K. Nakabayashi, S. i. Ohkoshi, B. J. C. A. E. J. Sieklucka, *Chem. -Eur. J.* **2019**, *25*, 11820-11825.

[146] J. M. Seco, I. Oyarzabal, S. Perez-Yanez, J. Cepeda, A. Rodriguez-Dieguez, *Inorg. Chem.* **2016**, *55*, 11230-11248.

[147] C. Jia, S. X. Liu, C. Tanner, C. Leiggener, A. Neels, L. Sanguinet, E. Levillain, S. Leutwyler, A. Hauser, S. J. C. A. E. J. Decurtins, *Chem. - Eur. J.* **2007**, *13*, 3804-3812.

[148] O. Cador, B. Le Guennic, F. Pointillart, *Inorg. Chem. Front.* **2019**, *6*, 3398-3417.

[149] R.-f. Li, R.-h. Li, X.-f. Liu, X.-h. Chang, X. Feng, *RSC Adv.* **2020**, *10*, 6192-6199.

[150] C. Train, M. Gruselle, M. Verdaguer, *Chem. Soc. Rev* **2011**, *40*, 3297-3312.

[151] R. Carr, N. H. Evans, D. Parker, *Chem. Soc. Rev.* **2012**, *41*, 7673-7686.

[152] A. Kaczmarek, J. Liu, B. Laforce, L. Vincze, K. Van Hecke, R. Van Deun, *Dalton Trans.* **2017**, *46*, 5781-5785.

[153] Y. Cui, H. Xu, Y. Yue, Z. Guo, J. Yu, Z. Chen, J. Gao, Y. Yang, G. Qian, B. Chen, *J. Am. Chem. Soc.* **2012**, *134*, 3979-3982.

[154] X. Yi, K. Bernot, F. Pointillart, G. Poneti, G. Calvez, C. Daiguebonne, O. Guillou, R. Sessoli, *Chem. - Eur. J.* **2012**, *18*, 11379-11387.

[155] T. P. Latendresse, N. S. Bhuvanesh, M. Nippe, *J. Am. Chem. Soc.* **2017**, *139*, 14877-14880.

[156] G. Peng, Q. Yang, Y. Chen, X.-T. Dong, Z. Zhang, X.-M. Ren, *Dalton Trans.* **2022**, *51*, 12484-12493.

[157] F. Pointillart, B. Le Guennic, T. Cauchy, S. Golhen, O. Cador, O. Maury, L. Ouahab, *Inorg. Chem.* **2013**, *52*, 5978-5990.

[158] M. Nie, J. Liang, C. Zhao, Y. Lu, J. Zhang, W. Li, C. Wang, T. Wang, *ACS Nano* **2021**, *15*, 19080-19088.

[159] J.-T. Chen, T.-D. Zhou, W.-B. Sun, *Dalton Trans.* **2023**, *52*, 4643-4657.

[160] F. Pointillart, B. Le Guennic, O. Cador, *Chem. - Eur. J.* **2024**, *30*, e202400610.

[161] J. R. Jiménez, I. F. Díaz-Ortega, E. Ruiz, D. Aravena, S. J. Pope, E. Colacio, J. M. Herrera, *Chem. - Eur. J.* **2016**, *22*, 14548-14559.

[162] L. Münzfeld, M. Dahlen, A. Hauser, N. Mahieu, S. K. Kuppusamy, J. Moutet, M. Tricoire, R. Köppe, L. La Droitte, O. Cador, *Angew. Chem. Int. Ed.* **2023**, *62*, e202218107.

[163] H.-Y. Shen, W.-M. Wang, Y.-X. Bi, H.-L. Gao, S. Liu, J.-Z. Cui, *Dalton Trans.* **2015**, *44*, 18893-18901.

[164] H. Flichot, A. Sickinger, J. Brom, B. Lefeuvre, V. Dorcet, T. Guizouarn, O. Cador, B. Le Guennic, L. Micouin, O. Maury, *Dalton Trans.* **2024**, *53*, 8191-8201.

[165] E. A. Mikhalyova, M. Zeller, J. P. Jasinski, R. J. Butcher, L. M. Carrella, A. E. Sedykh, K. S. Gavrilenko, S. S. Smola, M. Frasso, S. C. Cazorla, *Dalton Trans.* **2020**, *49*, 7774-7789.

[166] S.-F. Xie, L.-Q. Huang, L. Zhong, B.-L. Lai, M. Yang, W.-B. Chen, Y.-Q. Zhang, W. Dong, *Inorg. Chem.* **2019**, *58*, 5914-5921.

[167] X.-F. Ma, X.-D. Huang, L.-M. J. C. G. Zheng, Design, *Cryst. Growth Des.* **2022**, *23*, 1095-1103.

[168] S. K. Kuppusamy, E. Moreno-Pineda, A. M. Nonat, B. Heinrich, L. Karmazin, L. J. Charbonniere, M. Ruben, *Cryst. Growth Des.* **2023**, *23*, 1084-1094.

[169] S. Saha, K. S. Das, T. Sharma, S. Bala, A. Adhikary, G.-Z. Huang, M.-L. Tong, A. Ghosh, B. Das, G. Rajaraman, *Inorg. Chem.* **2022**, *61*, 2141-2153.

[170] J. Long, R. Vallat, R. A. Ferreira, L. D. Carlos, F. A. A. Paz, Y. Guari, J. Larionova, *Chem. Commun.* **2012**, *48*, 9974-9976.

[171] J. P. Costes, S. Titos-Padilla, I. Oyarzabal, T. Gupta, C. Duhayon, G. Rajaraman, E. Colacio, *Inorg. Chem.* **2016**, *55*, 4428-4440.

[172] I. Oyarzabal, B. Artetxe, A. Rodríguez-Diéguez, J. Á. García, J. M. Seco, E. Colacio, *Dalton Trans.* **2016**, *45*, 9712-9726.

[173] T. Kriese, *Untersuchungen an Eisen- und Lanthanoidhaltigen Koordinati-*

onsclustern mit Triazolat- sowie Semiquinonato-Liganden (KIT), PhD thesis **2016**.

[174] J. Braun., *The Influence of Intra-and Intermolecular Interactions on the Magnetic and Optical Properties of Lanthanide and Transition Metal Complexes, Karlsruhe Institute of Technology (KIT), PhD thesis* **2023**.

[175] Y. Peng, V. Mereacre, A. Baniodeh, Y. Lan, M. Schlageter, G. E. Kostakis, A. K. Powell, *Inorg. Chem.* **2016**, *55*, 68-74.

[176] Q. Zhang, S.-Y. Yang, S.-J. Chen, L. Shi, J. Yang, Z. Tian, Z. Ruan, D. Shao, *Journal of Molecular Structure* **2023**, *1294*, 136349.

[177] M. Feng, F. Pointillart, B. Lefeuvre, V. Dorcet, S. Golhen, O. Cador, L. Ouahab, *Inorg. Chem.* **2015**, *54*, 4021-4028.

[178] J. Xiong, H.-Y. Ding, Y.-S. Meng, C. Gao, X.-J. Zhang, Z.-S. Meng, Y.-Q. Zhang, W. Shi, B.-W. Wang, S. Gao, *Chem. Sci.* **2017**, *8*, 1288-1294.

[179] F. Yang, Q. Zhou, G. Zeng, G. Li, L. Gao, Z. Shi, S. Feng, *Dalton Trans.* **2014**, *43*, 1238-1245.

[180] T. Han, Y.-S. Ding, Z.-H. Li, K.-X. Yu, Y.-Q. Zhai, N. F. Chilton, Y.-Z. Zheng, *Chem. Commun.* **2019**, *55*, 7930-7933.

[181] S. Biswas, S. Das, J. Acharya, V. Kumar, J. van Leusen, P. Kögerler, J. M. Herrera, E. Colacio, V. Chandrasekhar, *Chem. - Eur. J.* **2017**, *23*, 5154-5170.

[182] D. Gatteschi, R. Sessoli, *Angew. Chem. Int. Ed.* **2003**, *42*, 268-297.

[183] J.-L. Liu, Y.-C. Chen, M.-L. Tong, *Chem. Soc. Rev* **2018**, *47*, 2431-2453.

[184] J. Tang, I. Hewitt, N. Madhu, G. Chastanet, W. Wernsdorfer, C. E. Anson, C. Benelli, R. Sessoli, A. K. Powell, *Angew. Chem. Int. Ed.* **2006**, *45*, 1729-1732.

[185] L. Chibotaru, L. Ungur, A. Soncini, *Angew. Chem. Int. Ed.* **2008**, *47*, 4126-4129.

[186] A. B. Carter, J. Braun, T. Bodenstein, R. F. Pfleger, M. Schulze, T. Kriese, S. F. Habermann, D. Liu, A. A. Al-Kahtani, E. Moreno-Pineda, *Inorg. Chem.* **2025**, *10.1021/acs.inorgchem.5c04406*.

[187] J. Olsen, *Chem. - Eur. J.* **2011**, *111*, 3267-3272.

[188] M. Urdampilleta, S. Klayatskaya, M. Ruben, W. Wernsdorfer, *ACS nano* **2015**, *9*, 4458-4464.

[189] W. Wernsdorfer, N. Aliaga-Alcalde, D. N. Hendrickson, G. Christou, *Nature* **2002**, *416*, 406-409.

[190] W. Wernsdorfer, S. Bhaduri, R. Tiron, D. Hendrickson, G. J. P. r. l. Christou, *Phys. Rev. Lett.* **2002**, *89*, 197201.

[191] W. Humphrey, A. Dalke, K. Schulten, *J. Molec. Graphics* **1996**, *14*, 33-38.

[192] P. D'Angelo, A. Zitolo, V. Migliorati, G. Chillemi, M. Duvail, P. Vitorge, S. Abadie, R. J. I. c. Spezia, **2011**, *50*, 4572-4579.

[193] L. M. Toma, R. Lescouëzec, J. Pasán, C. Ruiz-Pérez, J. Vaissermann, J. Cano, R. Carrasco, W. Wernsdorfer, F. Lloret, M. Julve, *J. Am. Chem. Soc.* **2006**, *128*, 4842-4853.

[194] J. Merz, M. Dietz, Y. Vonhausen, F. Wöber, A. Friedrich, D. Sieh, I. Krummenacher, H. Braunschweig, M. Moos, M. Holzapfel, *Chem.- Eur. J.* **2020**, *26*, 438-453.

[195] S.-H. Chen, H.-S. Chin, Y.-R. Kung, *Polymers* **2022**, *14*, 261.

[196] M. Magerstädt, O. A. Gansow, M. W. Brechbiel, D. Colcher, L. Baltzer, R. H. Knop, M. E. Girton, M. J. M. r. i. m. Naegele, *Magnet. Reson. Medi.* **1986**, *3*, 808-812.

[197] A. D. Sherry, R. D. Brown, C. F. Geraldes, S. H. Koenig, K.-T. Kuan, M. Spiller, *Inorg. Chem.* **1989**, *28*, 620-622.

[198] D. Meyer, M. Schaefer, B. J. I. r. Bonnemain, *Investi. Radiology* **1988**, *23*, S232-S235.

[199] P.-E. Car, M. Perfetti, M. Mannini, A. Favre, A. Caneschi, R. Sessoli, *Chem. Commun.* **2011**, *47*, 3751-3753.

[200] M. Briganti, G. F. Garcia, J. Jung, R. Sessoli, B. Le Guennic, F. Totti, *Chem. Sci.* **2019**, *10*, 7233-7245.

[201] M. P. Giuseppe Cucinotta, Javier Luzon, Mael Etienne, Pierre-Emmanuel Car, Andrea Caneschi, Guillaume Calvez, Kevin Bernot, Roberta Sessoli, *Angew. Chem. Int. Ed.* **2012**, *51*, 1606-1610.

[202] A. B. Canaj, M. K. Singh, E. R. Marti, M. Damjanović, C. Wilson, O. Céspedes, W. Wernsdorfer, G. Rajaraman, M. Murrie, *Chem. Commun.* **2019**, *55*, 5950-5953.

[203] R. Stewart, A. B. Canaj, S. Liu, E. Regincós Martí, A. Celmina, G. Nichol, H.-P. Cheng, M. Murrie, S. Hill, *J. Am. Chem. Soc.* **2024**, *146*, 11083-11094.

[204] Z. Zhu, X. Ying, C. Zhao, Y.-Q. Zhang, J. Tang, *Inorg. Chem. Front.* **2022**, *9*, 6061-6066.

[205] S. K. Gupta, T. Rajeshkumar, G. Rajaraman, R. Murugavel, *Chem. Sci.* **2016**, *7*, 5181-5191.

[206] G. M. Sheldrick, *Acta Cryst.* **2015**, *C71*, 3-8.

[207] O. Dolomanov, L. Bourhis, R. Gildea, J. Howard, H. Puschmann, *J. Appl. Crystallogr* **2009**, *42*, 339-341.

7. Appendix

7.1 Crystallographic Data

Compound	**$Dy_2(phsq)_4$ $(tppo)_2(NO_3)_2$**	**$Nd_2(phsq)_4(tppo)_2(NO_3)_2$**
Empirical formula	$Dy_2C_{92}H_{62}N_2O_{16}P_2$	$Nd_2C_{92}H_{62}N_2O_{16}P_2$
Formula weight [g•mol^{-1}]	1838.38 g/mol	1801.85 g/mol
Temperature [K]	200 K	200 K
Crystal system	Triclinic	orthorhombic
Space group	$P\overline{1}$	Iba2
a [Å]	13.1038(3)	17.5348(2)
b [Å]	13.4573(3)	20.2226(3)
c [Å]	13.7832(3)	41.9943(8)
α [°]	68.082(2)	90
β [°]	62.323(2)	90
γ [°]	62.831(2)	90
Volume [Å^3]	1874.45(9)	14891.2(4)
Z	1	8
ρ_{calc} [g•cm^3]	1.629	1.607
μ [mm^{-1}]	10.894	7.954
F(000)	918.0	7248.0
Reflections collected	8914	17229
Radiation	MoKα (λ = 0.71073)	MoKα (λ = 0.71073)
Final R indexes [I>=2σ (I)]	R_1 = 0.0296 , wR_2 = 0.0769	R_1 = 0.0278 , wR_2 = 0.0584

Compound	**$Dy_2(phsq)_4(tcypo)_2(NO_3)_2$**	**$Dy_2(pysq)_4(tppo)_2(NO_3)_2$**
Empirical formula	$Dy_2C_{92}H_{98}N_2O_{16}P_2$	$Dy_2C_{100}H_{62}N_2O_{16}P_2$
Formula weight [g•mol^{-1}]	1874.66	1934.45
Temperature [K]	200 K	200 k
Crystal system	Triclinic	monoclinic
Space group	$P\overline{1}$	$P2_1/n$
a [Å]	12.4071(5)	14.2665(3)
b [Å]	12.4287(5)	13.7553(2)
c [Å]	14.8231(7)	19.4623(4)
α [°]	107.411(3)	90
β [°]	107.189(4)	94.589(2)
γ [°]	102.260(3)	90
Volume [Å^3]	1966.95(11)	3807.04(13)
Z	1	2
ρ_{calc} [g•cm^3]	1.583	1.688
μ[mm^{-1}]	10.430	10.898
F(000)	944.65	1932.0
Reflections collected	9563	9117
Radiation	MoKα (λ = 0.71073)	MoKα (λ = 0.71073)
Final R indexes [I>=2σ (I)]	R_1 = 0.0296 , wR_2 = 0.0769	R_1 = 0.0291 , wR_2 = 0.0707

Compound	**$[Dy_2(pysq)_4(tcypo)_2(NO_3)_2]$**	**$[Dy_2Zn_2(DOTA)_2(ZnCl_4) \cdot 10H_2O]$**
Empirical formula	$Dy_2C_{100}H_{98}N_2O_{16}P_2$	$Dy_2 Zn_2C_{32}H_{84}N_8O_{26}$
Formula weight [g•mol^{-1}]	1970.74	1662.82
Temperature [K]	200 K	200 K
Crystal system	Triclinic	monoclinic
Space group	$P\overline{1}$	$P2_1/c$
a [Å]	12.2652(9)	18.2931(4)
b [Å]	12.4697(8)	14.4466(3)
c [Å]	15.3654(10)	12.0873(2)
α [°]	107.338(5)	90
β [°]	103.009(6)	106.244(2)
γ [°]	102.886(5)	90
Volume [Å^3]	2076.6(3)	3066.83(11)
Z	1	2
ρ_{calc} [g•cm^3]	1.576	1.801
μ [mm^{-1}]	9.902	13.831
F(000)	1002.0	1676.0
Reflections collected	9116	7484
Radiation	MoKα (λ = 0.71073)	MoKα (λ=0.7 073)
Final R indexes [I>=2σ (I)]	R_1=0.0666 , wR_2 = 0.1883	R_1= 0.0671 , wR_2 = 0.2090

Compound	**$Dy_4Zn_4(DOTA)_4$ $(ZnCl_4)_2$ •$16H_2O$**	**[$Dy(H_2tapen)Cl$]**
Empirical formula	Dy_4 $Zn_4C_{64}H_{200}N_{16}O_{48}$	$DyC_{36}H_{38}N_8O_8Cl$
Formula weight [g•mol^{-1}]	2873.9	1034.80
Temperature [K]	200 K	200 K
Crystal system	monoclinic	orthorhombic
Space group	$P2_1/c$	Pbca
a [Å]	18.6163(11)	17.9438(2)
b [Å]	15.5930(19)	19.8360(3)
c [Å]	22.6269(13)	22.8346(4)
α [°]	90	90
β [°]	104.578(5)	90
γ [°]	90	90
Volume [Å^3]	6356.77(90)	8127.6(2)
Z	1	1
ρ_{calc} [g•cm^3]	1.768	1.691
μ [mm^{-1}]	12.986(11)	10.502
F(000)	1576.0	4216.0
Reflections collected	8028	9804
Radiation	MoKα (λ = 0.71073)	MoKα (λ = 0.71073)
Final R indexes [I>=2σ (I)]	R_1 = 0.0273 , wR_2 = 0.0385	R_1 = 0.0368 , wR_2 = 0.1007

7.2 Publications

1. **Yangxin Chen,** Jan Arneth, Eufemio Moreno-Pineda, Appu Sunil, Olaf Fuhr, Christopher E. Anson, Rüdiger Klingeler, Wolfgang Wernsdorfer, Jonas Braun and Annie K. Powell. Enhancing Magnetic Properties in Radical Dy^{III}_2 Dimer Single-Molecule Magnets by Ligand Functionalization [J]. (In preparation)

2. **Yangxin Chen,** Jan Arneth, Eufemio Moreno-Pineda, Appu Sunil, Olaf Fuhr, Christopher E. Anson, Rüdiger Klingeler, Wolfgang Wernsdorfer, Jonas Braun and Annie K. Powell. Two Air-stable Semiquinone Radical Nd^{III}_2 Dimer Single Molecule Magnets with Different Arrangements [J]. (In preparation)

3. **Yangxin Chen**, Zhangxian Chen, Yang Zhou, Yanqiang Li, Youchao Liu, Qingran Ding, Xin Chen, Sangen Zhao and Junhua Luo. An Antimony (III) Fluoride Oxalate Birefringent Material [J]. Chem. Eur. J., 2021, 27, 4557-4560. (hot paper)

4. **Yangxin Chen**, Tingting Zhu, Zheyao Xiong, Yang Zhou, Yanqiang Li, Qingran Ding, Youchao Liu, Xin Chen, Sangen Zhao and Junhua Luo. An Organic-Inorganic Hybrid Birefringent Material with Diverse Functional Groups [J]. Chem. Commun., 2021, 57, 6668 -6671

5. Yang Zhou, Xingyu Zhang, Zheyao Xiong, Xifa Long, Yanqiang Li, **Yangxin Chen**, Xin Chen, Sangen Zhao, Zheshuai Lin, and Junhua Luo. Non-π-Conjugated Deep-Ultraviolet Nonlinear Optical Crystal $K_2Zn_3(SO_4)(HSO_4)_2F_4$ [J]. J. Phys. Chem. Lett. 2021, 12, 8280−8284

6. Xin Chen, Han Wang, Youchao Liu, Yang Zhou, Weiqi Huang, Minjuan Li, Yanqiang Li, **Yangxin Chen**, Sangen Zhao, and Junhua Luo. A New Nonlinear Optical Material with $N(CN)^-$ Anion [J]. Chem. Eur. J.,2021, 27, 17769 – 17772

7.3 Acknowledgements

First and foremost, I sincerely thank my PhD supervisor, Prof. Dr. Annie K. Powell, for giving me the opportunity to pursue my PhD in Germany, providing me with the experimental platform, and supporting my collaborations with other research groups. I also learned from her a spirit of optimism and open-mindedness.

I'm also grateful to Dr. Christopher Anson for helping me refine the crystal structure and providing valuable advice in the experiment, which taught me magnetism knowledge. I also learned a rigorous, pragmatic, and cautious scientific attitude from him.

At the same time, I am very grateful to Dr. Jonas Braun for patiently explaining many experimental problems to me (I always ask him first when I encounter problems in the experiment). I have learned a lot of experience and knowledge of magnetism from him. Dr. Jonas has been very helpful in my PhD research, which has accelerated the progress of my project. I would like to express my sincere gratitude.

I'm also very grateful to Dr. Olaf Fuhr and Prof. Dr. Dieter Fenske for helping me measure and collect single crystals structure. They always promptly provided me with crystals structure and provided me with crystal information. From Prof. Dieter Fenske, I learned a passion for work. He should have been enjoying retirement, but he continues to work diligently because of his passion. This passion deeply inspires me. I wish him good health and a long life, and may he enjoy his work every day!

I would like to thank Dr. Sukhen Bala for his guidance in experimental synthesis and for giving me a lot of practical experimental experience, and thank Prashant Anand at the same time for his help in something during my PhD studies, whether it was experiments or daily trivial matters. I am sincerely grateful.

I would also like to thank our research group secretaries Isabella Vogelbacher and Gertraud Amschlinger for their continued help in handling any my matters related to KIT and in helping me apply for a new contract for my PhD extension.

I would like to thank Dr. Alexander Hinz for helping me set up the Schlenk line in the Modulbau lab 006, which greatly advanced my experimental progress.

I would like to express my sincere gratitude to Daniel Seufert, who shared my lab at Modulbau and provided me with ample experimental space. I am grateful for his continued help during my period of Ph.D.

In addition, I would like to thank PD. Dr. Masooma Ibrahim to help me measure the Powder-XRD data, and I am grateful to Dr. Rouven Pfleger for guiding me at the beginning of my PhD and for helping me adapt quickly to my new research direction. Moreover, I would like to thank Dr. Yannik Schneider for teaching me how to plot magnetic data. Finally, I would like to thank the whole Powell Group for the friendly atmosphere and excellent working environment. I would also like to thank Dr. Xianfeng Li, Christian Pachl, Dr. Aravind Raveendranathan, Vanikrishna Ajithkumar Njayappallil, Dr. Aiswarya Chalikunnath, Kliment Bozov, Emilia Seeger, Sören Lischewski , Dr. Thomas Ruppert, Dr. Hagen Kämmerer, Dr. Muthu Thangavel, Dr. Umaira Shuaib, and Imon Jyoti Dutta for the wonderful time we spent together.

In addition, I would like to express my deepest gratitude to Dr. Jan Arneth from Prof. Dr. Rüdiger Klingeler's group at Heidelberg University, who helped me measure most of the magnetic data and dedicated his time and effort to this endeavor, teaching me a great deal about magnetism. I would also like to thank Appu Sunil and Dr. Eufemio Moreno-Pineda from Prof. Dr. Wolfgang Wernsdorfer's group. I thank Appu for helping me obtain the magnetic data for the Micro-SQUID, and Dr. Eufemio for the theoretical calculations. I would also

like to thank Dr.Tingting Ruan, Dr. Zhaoyang Jing, and Yaorong Chen from Prof. Dr. Mario Ruben's group for helping me with magnetic measurement and explaining some magnetic knowledge.

Last but not least, I would like to thank my family and my closest friends for their support and understanding along the way, which gave me more motivation and encourage to complete my Ph.D studies.